

---


Electronic Theses and Dissertations, 2004-2019

---

2015

## Planar Laser Induced Fluorescence Experiments and Modeling Study of Jets in Crossflow at Various Injection Angles

Luke Thompson  
*University of Central Florida*

 Part of the [Aerodynamics and Fluid Mechanics Commons](#)  
Find similar works at: <https://stars.library.ucf.edu/etd>  
University of Central Florida Libraries <http://library.ucf.edu>

This Masters Thesis (Open Access) is brought to you for free and open access by STARS. It has been accepted for inclusion in Electronic Theses and Dissertations, 2004-2019 by an authorized administrator of STARS. For more information, please contact [STARS@ucf.edu](mailto:STARS@ucf.edu).

---

### STARS Citation

Thompson, Luke, "Planar Laser Induced Fluorescence Experiments and Modeling Study of Jets in Crossflow at Various Injection Angles" (2015). *Electronic Theses and Dissertations, 2004-2019*. 1434. <https://stars.library.ucf.edu/etd/1434>

PLANAR LASER INDUCED FLUORESCENCE EXPERIMENTS AND MODELING STUDY  
OF JETS IN CROSSFLOW AT VARIOUS INJECTION ANGLES

by

LUKE ZIMMERMAN THOMPSON  
B.S. Physics, Bethel University, 2012

A thesis submitted in partial fulfillment of the requirements  
for the degree of Master of Science in Aerospace Engineering  
in the Department of Mechanical and Aerospace Engineering  
in the College of Engineering and Computer Science  
at the University of Central Florida  
Orlando, Florida

Spring Term  
2015

Major Professor: Dr. Subith Vasu

©2015 Luke Zimmerman Thompson

## **ABSTRACT**

Planar Laser Induced Fluorescence (PLIF) with acetone seeding was applied to measure the scalar fields of an axisymmetric freejet and an inclined jet-in-crossflow as applicable to film cooling. From the scalar fields, jet-mixing and trajectory characteristics were obtained. In order to validate the technique, the canonical example of a nonreacting freejet of Reynolds Numbers 900-9000 was investigated. Desired structural characteristics were observed and showed strong agreement with computational modeling. After validating the technique with the axisymmetric jet, the jet-in-crossflow was tested with various velocity ratios and jet injection angles. Results indicated the degree of wall separation for different injection angles and demonstrate both the time-averaged trajectories as well as select near-wall concentration results for varying jet momentum fluxes. Consistent with literature findings, the orthogonal jet trajectory for varying blowing ratios collapsed when scaled by the jet-to-freestream velocity ratio and hole diameter,  $rd$ . Similar collapsing was demonstrated in the case of a non-orthogonal jet. Computational Fluid Dynamic (CFD) simulations using the OpenFOAM software was used to compare predictions with select experimental cases, and yielded reasonable agreement. Insight into the importance and structure of the counter rotating vortex pair and general flow field turbulence was highlighted by cross validation between CFD and experimental results.

Soli Deo Gloria

## **ACKNOWLEDGMENTS**

I would like to thank the numerous individuals who have contributed in both technical and personal support through my entire Masters work. A special appreciation is extended to my fiancée *Miss Katherine Raetz* for her loving understanding and encouragement throughout the entire process. Additionally I would like to thank my parents *Les and Kris Thompson* who have always been there to cheer me on, and instill the drive necessary to surmount adversity.

Special thanks are given to *Dr. Subith Vasu* for his guidance role throughout my research and academic endeavors. Committee members *Dr. Jayanta Kapat* and *Dr. Alain Kassab* are also greatly appreciated for their educational positions, as well as their professional guidance. All other professors and mentors who have fostered a deeper understanding and appreciation for this field have earned my heartfelt gratitude.

I am extremely grateful for the collaboration and encouragement gained from working with my colleagues in Dr. Vasu's lab, especially *Bader Almansour* and *Batikan Koroglu* whose technical expertise and friendship were of great importance.

Finally, I would like to thank the numerous individuals whose invaluable contributions to my research work allowed for otherwise unattainable levels of progress including: *Steven O'Briant, Greg Natsui, Craig Fernandes, Tyler Voet, Zack Little, and Carlos Velez.*

Financial support was provided through the University of Central Florida as well as NASA through the Florida Space Grant Consortium.

# TABLE OF CONTENTS

LIST OF FIGURES .....	viii
LIST OF TABLES .....	xi
LIST OF VARIABLES AND CONSTANTS .....	xii
CHAPTER 1. INTRODUCTION .....	1
1.1 Why Jets in Crossflow .....	1
1.2 Jet in Crossflow Structure.....	2
1.3 Film Cooling.....	4
1.4 Optical Diagnostics.....	7
1.4.1 Planar Laser Induced Fluorescence.....	8
1.4.2 Particle Imaged Velocimetry.....	9
1.4.3 Pressure and Temperature Sensitive Paints.....	10
CHAPTER 2. LITERATURE REVIEW .....	12
2.1 Laser Induced Fluorescence.....	12
2.1.1 LIF Theory .....	13
2.1.2 Acetone Photophysics .....	14
2.1.3 LIF Measurements of Pressure and Temperature.....	18
2.2 Diagnostics of Jets in Crossflow.....	20
2.2.1 Structural Investigations.....	20
2.2.2 Velocity Profiling.....	22
2.2.3 Trajectory Scaling .....	24
2.2.4 Geometry Considerations.....	27
2.3 Mass Heat Transfer Analogy .....	29
CHAPTER 3. EXPERIMENTAL SETUP .....	32
3.1 Wind Tunnel .....	32
3.1.1 Tunnel Construction.....	32
3.1.2 Coupon Development.....	34
3.1.3 Seeding System .....	35
3.2 Optical Setup.....	36
3.2.1 Laser Characterization.....	37
3.2.2 Camera Information .....	38
3.2.3 Optical Material Considerations.....	40
CHAPTER 4. PLIF PROCESSING.....	43
4.1 Correction Procedure .....	43
4.1.1 Sheet Characterization.....	43

4.1.2 Background and Referencing .....	47
4.1.3 Time Averaging of Images .....	48
4.2 Validation With Freejet .....	51
CHAPTER 5. RESULTS AND DISCUSSION .....	57
5.1 Jet in Crossflow .....	57
5.1.1 Fixed Angle Scaling .....	61
5.1.2 Fixed Velocity Ratio Scaling .....	66
5.1.3 Density Ratio Variations .....	67
5.2 CFD Comparisons.....	68
CHAPTER 6: CONCLUSIONS .....	77
APPENDIX A: LIF PROCESSING CODE .....	80
APPENDIX B: SAMPLE COUPON DRAWING .....	85
REFERENCES .....	87



## LIST OF FIGURES

Figure 1. a) Large length scale and b) small timescale examples of jets in crossflow [1, 2] .....	1
Figure 2. Jet in crossflow with dominating features displayed.....	3
Figure 3. Typical normalized temperature distribution in a film cooled wall [3].....	5
Figure 4. Conventional film cooled turbine blade with multiple rows of coolant holes [7].....	6
Figure 5. Boeing 737 turbine with blade failure due to thermal degradation of the blades [8].....	7
Figure 6. Results of a simultaneous PLIF/PIV measurement of a turbulent jet [10].....	10
Figure 7. PSP measurements for a single row of holes indicating film cooling effectiveness as a function .....	11
Figure 8. Vapor pressure as a function of temperature for acetone .....	15
Figure 9. Excitation and emission diagram of electronically excitable species[24].....	15
Figure 10. a) Absorption feature of Acetone, b) Fluorescent yield spectrum of Acetone [22] ....	17
Figure 11. Linear fluorescence as a function of fluence [22] .....	18
Figure 12. Fluorescent signal ratio as a function of temperature for select wavelength pairs for acetone vapor [20].....	19
Figure 13. Top) smoke trails impinging on leading edge of jet. Bottom) top-down view showing wake region and horseshoe vortices [29].....	21
Figure 14. Trajectory results for 90° jet as reported by Smith and Mungal [54].....	25
Figure 15. Hole geometries proposed for use in film cooling [58].....	28
Figure 16. Schematic of the wind tunnel configuration.....	32
Figure 17. Wind tunnel used in JIC testing.....	33
Figure 18. Velocity distribution in the test section as a function of distance from the wall.....	34
Figure 19. Simplified schematic of the full experimental setup .....	37
Figure 20. Sample Laser Pulse Power fluctuation for 1064nm wavelength.....	38
Figure 21. Quantum efficiency vs. wavelength for PCO 1600 camera [71].....	39

Figure 22. Wall scatter effects as seen by the camera for various surfaces. Luminosity demonstrated in arbitrary units .....	41
Figure 23. a) Calibration Chamber for characterizing laser sheet with 3in UVFS window for laser access b) Sample of fluorescence in a.u. as a two dimensional function.....	44
Figure 24. a) Fluorescence plotted vs. y for varying x values. b) Fluorescence plotted vs. x for varying y values .....	45
Figure 25. Convergence of fluorescent mean for arbitrary locations in uniform acetone field....	49
Figure 26. Convergence of mean for arbitrary distances above freejet exit .....	50
Figure 27. Demonstration of the correction effects for a turbulent freejet a) Raw fluorescence, b) background subtraction and normalization, c) energy flux corrections, d) absorption corrected. 52	
Figure 28. Instantaneous images of normalized concentration maps in a freejet for three Reynolds numbers. Left image shows a turbulent jet of Re=9006, middle image Re=3152, right image is a laminar jet of Re=900 .....	53
Figure 29. Plot of 10% concentration lines for two Reynolds numbers shown across symmetry planes .....	55
Figure 30. Compared concentration maps of an experimental and modeled freejet .....	56
Figure 31. Normalized time-averaged concentration fields for 30° inclined jets in crossflow for three varying velocity ratios.....	58
Figure 32. Normalized instantaneous concentration fields for 30° inclined jets in crossflow for three varying velocity ratios.....	59
Figure 33. a) Normalized concentration as a function of y /d at a) x=2d and b) x=10d downstream of the jet exit.....	60
Figure 34. Trajectories for different velocity ratio conditions of an orthogonal jet .....	61
Figure 35. Trajectories for different velocity ratio conditions of an orthogonal jet scaled by a) $rd$ , b) $r^2d$ .....	62
Figure 36. Varying velocity ratio conditions of an orthogonal jet scaled by $r^{1.2}d$ .....	64
Figure 37. Trajectories for different velocity ratio conditions of a 30° jet. a) unscaled, b) scaled by $rd$ .....	65
Figure 38. a) Unscaled and b) Scaled trajectories for varying jet angles for a fixed velocity ratio of $r=1.36$ .....	66

Figure 39. a) Unscaled and b) Scaled trajectories for varying jet angles for a fixed velocity ratio of $r=0.51$ .....	67
Figure 40. Concentration maps of a $30^\circ$ jet with $r=1.7$ . a) Experimental, b) low turbulence CFD, and c) higher turbulence CFD normalized concentration maps for time-averaged JIC .....	70
Figure 41. CFD generated contour map of a $30^\circ$ jet with $r=1.7$ , for $C=0.5$ .....	71
Figure 42. CVP development downstream of $30^\circ$ $r=1.7$ jet at downstream planes of a) $x=1.58d$ , b) $x=3.91d$ , c) $x=6.38d$ , and d) $x=8.97d$ .....	73
Figure 43. Comparison of experimental and CFD reported trajectories.....	74
Figure 44. Velocity profile for instantaneous CFD result of $30^\circ$ $r=1.7$ jet, with colorbar showing velocity magnitude in m/s.....	74
Figure 45. OpenFOAM trajectories for different velocity ratio conditions of a $30^\circ$ jet scaled by $rd$ .....	75

## **LIST OF TABLES**

Table 1. Flame temperatures and melting points for common gasses and metals respectively[3].	4
Table 2. Relevant Camera Specifications .....	40
Table 3. Uncertainty values for processing correction factors in a time-averaged study .....	50

## LIST OF VARIABLES AND CONSTANTS

$\alpha$	=	<i>absorption coefficient [unitless]</i>
$c$	=	<i>speed of light [m/s]</i>
$c_{cj}$	=	<i>entrainment coefficient [unitless]</i>
$c_{ej}$	=	<i>entrainment coefficient of jet [unitless]</i>
$c_{ew}$	=	<i>entrainment coefficient of wake [unitless]</i>
$C$	=	<i>mass fraction [unitless]</i>
$d$	=	<i>jet diameter [mm]</i>
$dV_c$	=	<i>excitation volume [m<sup>3</sup>]</i>
$D$	=	<i>diffusion coefficient [cm<sup>2</sup>/s]</i>
$E$	=	<i>energy density of laser sheet [J/m<sup>2</sup>]</i>
$f$	=	<i>focal length [m]</i>
$h$	=	<i>Planck's constant [J*s]</i>
$J$	=	<i>momentum flux ratio [unitless]</i>
$K$	=	<i>Boltzmann's constant [J/K]</i>
$k$	=	<i>turbulent kinetic energy [J/kg]</i>
$Le$	=	<i>Lewis number [unitless]</i>
$\lambda$	=	<i>light wavelength [m]</i>
$M$	=	<i>blowing ratio [unitless]</i>
$\eta$	=	<i>collection efficiency of optical system [unitless]</i>
$\eta_{film}$	=	<i>film cooling effectiveness (surface) [unitless]</i>
$\sigma$	=	<i>absorption cross section [cm<sup>2</sup>]</i>
$\rho_{jet}$	=	<i>air/acetone vapor mixture density [kg/m<sup>3</sup>]</i>
$\rho_\infty$	=	<i>freestream air density [kg/m<sup>3</sup>]</i>
$P$	=	<i>pressure [Pa]</i>
$\varphi$	=	<i>fluorescence yield [unitless]</i>

$r$	=	<i>jet-to-freestream velocity ratio [unitless]</i>
$Re$	=	<i>Reynolds number [unitless]</i>
$S_f$	=	<i>collected signal per volume [photons]</i>
$T$	=	<i>temperature [K]</i>
$T_\infty$	=	<i>freestream temperature [K]</i>
$T_{aw}$	=	<i>adiabatic wall temperature [K]</i>
$\theta$	=	<i>film cooling effectiveness (fluid) [unitless]</i>
$u_{jet}$	=	<i>jet velocity [m/s]</i>
$U$	=	<i>mean flow velocity [m/s]</i>
$u'$	=	<i>turbulent velocity fluctuations [m/s]</i>
$V_\infty$	=	<i>freestream velocity [m/s]</i>
$w$	=	<i>focal waist [m]</i>
$w_o$	=	<i>beam diameter [m]</i>
$X_i$	=	<i>acetone mole fraction [unitless]</i>
$X_w$	=	<i>jet to freestream mole fraction at the wall [unitless]</i>
$x_{jet}$	=	<i>concentration of acetone in seeded mixture [PPM]</i>

# CHAPTER 1. INTRODUCTION

## 1.1 Why Jets in Crossflow

Perhaps one of the most ubiquitous structures in the physical world is a fluid jet. By spanning a tremendous range of scales, gaseous state jets are critical to the continuing technological development of the world. One particular subset of the overarching gas-jet category is the regime of a gas-phase jet introduced into a crossflowing freestream. A jet in crossflow can broadly be defined as a jet interacting with a flow that has a velocity component orthogonal to the jet's velocity. Although the canonical jet in crossflow exists as a jet completely orthogonal to the freestream, this is merely a restricted case in which the compound and inclination angles are zero, as will be defined in the next section.

Jets in crossflows exist in a diverse array of velocity and length scales, and exist in natural phenomenon as well as established and emerging technologies. As an example of large scale phenomenon, figure 1a illustrates a volcanic eruption where the jet (plume) is interacting with the wind. It is easy to envision that similar scaled events such as smoke from factories hold the potential to have geological and climate impacting repercussions.

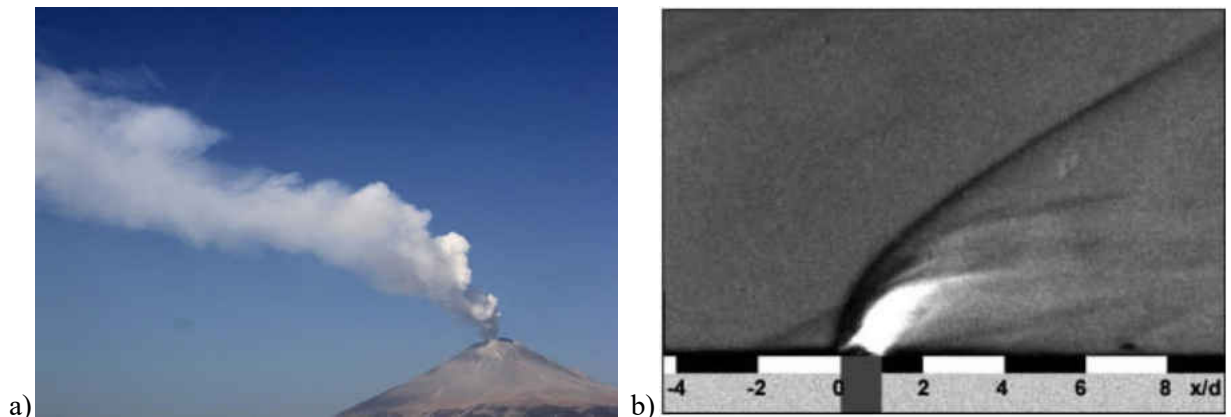


Figure 1. a) Large length scale and b) small timescale examples of jets in crossflow [1, 2]

Figure 1b demonstrates the other extreme of the spectrum where a jet is introduced into a supersonic crossflow. This system is of particular interest in the continuing development of supersonic combustion ramjet (SCRAMJET) engines in which the freestream flow through the engine is on the order of 2000m/s. In these tests a fuel, typically hydrogen or ethylene, is injected orthogonally to the freestream at a high enough velocity to achieve effective penetration into the flow and achieves thorough mixing with downstream propagation. A second example where significant penetration and mixing is required could include dilution cooling applications where the bulk freestream fluid temperature is sought to be reduced. Finally, thrust vectoring incorporates principles leading to a high-velocity jet in crossflow, and is seen in both military aircraft as well as rockets.

A converse goal of minimal penetration and jet mixing are more practical in localized cooling applications. One of the most common uses of a jet in crossflow is seen in film cooling applications which are very common to gas turbines and rocket engines. A complete understanding of the jet in terms of structure and propagation characteristics are an integral component in film cooling applications, where not only the efficiency of the engine is at stake, but the structural integrity may also be compromised with incomplete characterizations.

## **1.2 Jet in Crossflow Structure**

In order to completely understand the phenomenon of a jet in crossflow, it is imperative to first consider the basic structure of the jet and the features which develop. Figure 2 illustrates the dominant characteristics of the jet in crossflow as established by authors over the course of decades.



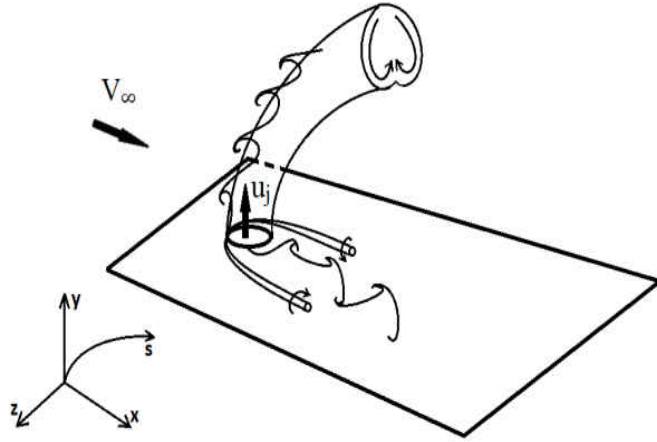


Figure 2. Jet in crossflow with dominating features displayed

In figure 2, one can see that as the freestream ( $V_\infty$ ) wraps around the jet, a counter rotating vortex pair is expected to develop due to shearing effects. Along the upstream edge of the jet, shear layer interactions will cause rolled-up vortices to form. The structure of these vortices will largely depend on the initial turbulence conditions of the jet itself. On the wall surface, a horseshoe vortex is expected to form, and a region of instability is expected to exist in the wake region behind the jet.

For the sake of clarity, the inclination angle of the jet is defined as the angle between  $V_\infty$  and  $u_j$  in the  $x$ - $y$  plane, and will be indicated as  $\gamma$ . The compound angle of the jet can be defined as the angle between  $V_\infty$  and  $u_j$  in the  $x$ - $z$  plane. While there is interest in non-zero compound angle jets in applications of film cooling, the jets investigated in this study all maintained a compound angle of zero. As jets used for thermal management purposes dominantly exist in aeropropulsion or power generation engines, it is reasonable to expect that the flow velocities in the jet will result in high enough Reynolds numbers to ensure a highly turbulent jet.

### 1.3 Film Cooling

The primary motivation for studying non-orthogonal near-wall jets stems from their application in film cooling configurations. Therefore it is advantageous to briefly establish an overview of the theory and applications of film cooling itself.

There are numerous situations, most involving a combustion process, in which an internal flow with a very high temperature ( $>2000\text{K}$ ) exists. Table 1 illustrates the post-combustion temperature for common fuel mixtures as well as the melting point temperatures for commonly used metals.

Table 1. Flame temperatures and melting points for common gasses and metals respectively[3]

<b>Fuel Gas</b>	<b>Combustion Temp (°C)</b>	<b>Metal</b>	<b>Melting Temp (°C)</b>
<b>Acetylene</b>	2500	Aluminum	659
<b>Butane</b>	1970	Brass	927
<b>Ethane</b>	1955	Cast Iron	1204
<b>Hydrogen</b>	2210	Gold	1063
<b>Methane</b>	1950	Nickel	1452
<b>Natural Gas</b>	1960	Steel	1371
<b>Propane</b>	1967	Tungsten	3399

It is clear from table 1 that extremely high temperatures can prove fatal for the bounding structures if thermal management is not employed. Even the use of high-temperature super alloys does not alleviate the issues faced in such a harsh environment. The most common applications of film cooling are gas turbines for power generation purposes and rocket engines. Both of these

have internal flows of extremely hot burned gasses, and are therefore ideal candidates for film cooling.

The concept of film cooling itself is fairly elementary. By injecting a relatively cool gas through the wall surfaces in contact with the hot gasses, the cool jet can remain attached to the wall and form a gaseous film which propagates downstream. Since the primary mode of heat transfer in these systems is convection, this film provides a thermal barrier so that the hot combustion products will not heat the walls to dangerous temperatures. Conventionally, the film cooling effectiveness can be defined as:

$$\eta_{film} = \frac{T_{\infty} - T_{aw}}{T_{\infty} - T_{coolant}} \quad (1)$$

where the freestream temperature is denoted as  $T_{\infty}$  and  $T_{aw}$  represents the adiabatic wall temperature. In film cooling experiments, the normalized temperature assumes a profile seen in figure 3, where the colorbar represents  $\theta$ , defined as:

$$\theta = \frac{T_{\infty} - T(x,y)}{T_{\infty} - T_{coolant}} \quad (2)$$

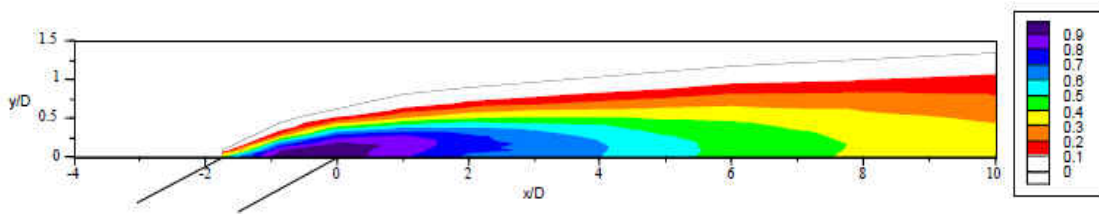


Figure 3. Typical normalized temperature distribution in a film cooled wall [4]

In accordance with figure 3, the highest cooling effectiveness can be expected to exist near the coolant injection site, and dissipate downstream. Due to transport analogies, the temperature distribution can be linked to the coolant concentration distribution. Interested readers are

forwarded to the following references which provide extensive databases for many configurations and the resulting effectiveness distributions on the surface[5, 6]. Additionally, Han provides an excellent overview of heat transfer in gas turbines, with an excellent discussion on film cooling[7].

The exact profile and temperature distribution in a cooling film, is a complex function of several parameters. These include the coolant injection angle, boundary layer profile, mass flux rate of coolant, hole/slot shape, and turbulence and velocity of the combustion gasses in the chamber and nozzle. In regards to the hole geometry, the two common schemes are a hole (inclined or orthogonal) or a slot which runs around the circumference of the wall. Typically, in applications on gas turbine blades, grids of discrete holes are used due to the geometry of the blades. However, in the nozzle of a rocket engine, an annular slot is often employed as it yields a more continuous distribution around the nozzle. Figure 4 displays a turbine blade with film cooling holes along its surface.

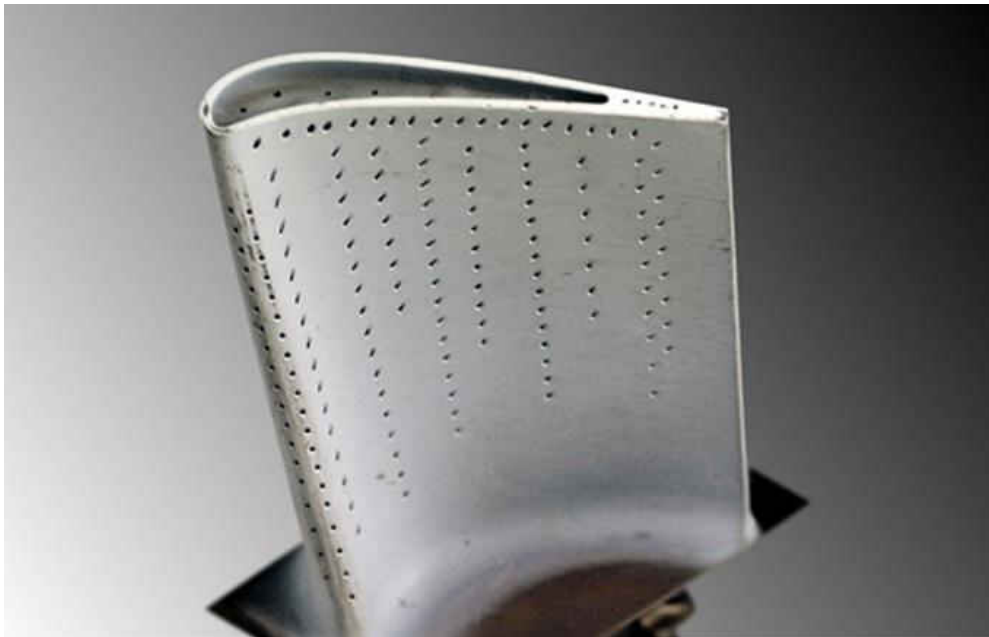


Figure 4. Conventional film cooled turbine blade with multiple rows of coolant holes [8]



Figure 5. Boeing 737 turbine with blade failure due to thermal degradation of the blades [9]

Figure 5 displays a row of turbine blades from a Boeing 737 engine, after a 2009 incident in which the blade material failed. The failure mode was cited as follows: “*Fracture of the stage-1 LPT blades was probably precipitated by thermal degradation of the blade alloy.*”[9]. Therefore, film cooling allows for the safe operation of materials in a harsh thermal environment to alleviate issues of catastrophic failure from excessive temperature. Additionally, by protecting surfaces from high temperatures, the freestream temperature can safely be increased. In gas turbines, an increase in the post-combustion temperatures ultimately leads to a performance and efficiency increase of the turbine.

#### **1.4 Optical Diagnostics**

Recent developments in the field of optical technologies have unlocked a myriad of new measurement techniques which previously had only been attainable through physical in-situ instruments. With the advent of high-speed high-resolution cameras and high-power ultrafast lasers, nonintrusive optical diagnostics now provide temporally and spatially resolved measurements of velocity, pressure, temperature, and species characterization with a level of

both ease and precision unattainable in decades past. Optical diagnostics themselves are simultaneously ingenious and effective, and have the unique characteristics of being fully non-intrusive. Due to their non-intrusive nature, practical considerations of fatigue and environment considerations are oftentimes nullified. Additionally, spatial resolution is often increased dramatically above previous limits of digital instrumentation. Although sections 1.4.2 and 1.4.3 discuss techniques not explored in this work, they are included for the sake of a more complete understanding evolution of thermo-fluid measurement techniques.

#### *1.4.1 Planar Laser Induced Fluorescence*

The diagnostic tool of choice in this work was a system incorporating the principles of laser induced fluorescence (LIF) to accurately and quantitatively extrapolate structural information from a jet in crossflow. While the details of this technique will be expounded upon in chapter 2, its use in extrapolating temperature, pressure, and concentrations are responsible for the relatively recent incorporation of this method in numerous scientific works. Basic LIF theory dictates that excitation of target compounds via a specifically chosen wavelength yields a resulting fluorescence from those compounds which is a complex function of many parameters. In expanding the beam into a sheet, truly 2-dimensional slices of a volume can be obtained through Planar Laser Induced Fluorescence (PLIF).

Before the development of LIF as a common technique, mixing measurements were unreliable and quantitatively inaccurate, and relied on fundamental particles such as smoke particles, for qualitative low-resolution measurements. Aside from absorption based measurements, non-intrusive species measurements were previously out of question, but now both seeded and select naturally occurring molecules can be isolated for investigation through

LIF. This has generated special interest in the application of reacting flows as species such as OH\* and CH\* can be identified using LIF.

#### *1.4.2 Particle Imaged Velocimetry*

A second non-intrusive optical diagnostic method used in research of fluid behaviors is Particle Imaged Velocimetry (PIV). Relying on a similar setup to PLIF, PIV generates spatial distributions of velocity. This is achieved by seeding the flow with microparticles which are subjected to two pulses of laser sheets separated by very small amount of time. By determining the distance travelled by the particles in a know time span, both the direction and the magnitude of the velocity can be determined for the full field of study in a given 2d plane. Recent advances in laser technology have allowed for burst lasers in which the pulse pairs are separated by very small inter-pair time gaps, allowing for temporally evolving maps of velocity fields[10].

In contrast to previous intrusive methods, PIV allows for both instantaneous and time-averaged velocity characterizations in which the full-field magnitudes and velocities are obtained in one measurement. Therefore PIV is a demonstration of a technique which strongly complements PLIF to provide quantitative flow information unparalleled by previous technologies. For the sake of illustration, figure 6 demonstrates the use of PIV in an axially symmetric turbulent jet. Simultaneous LIF measurements were obtained and demonstrate the concentration profile superimposed with the velocity vectors obtained via PIV[11].

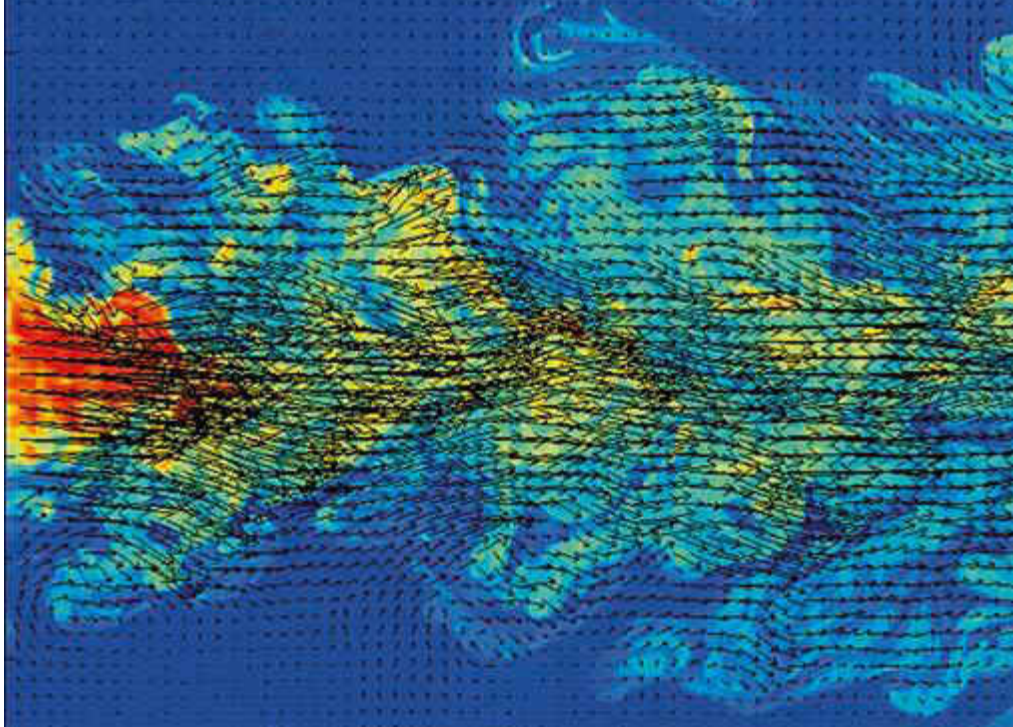


Figure 6. Results of a simultaneous PLIF/PIV measurement of a turbulent jet [11]

#### *1.4.3 Pressure and Temperature Sensitive Paints*

While PIV and PLIF are able to fully characterize a two dimensional flow in a nonintrusive and instantaneous manner, surface measurements yield information which may be difficult to obtain using PLIF or PIV. Traditionally, surface measurements of pressure and temperature have been achieved using thermocouples and pressure taps at discrete locations. However, optically excited pressure and temperature sensitive paints (PSP and TSP) operating on very similar principles to LIF now allow for continuous full-surface characterizations of partial pressure and temperature. Additionally, as in the case of PLIF, proper image processing must be employed to convert from a luminous signal to a relative concentration distribution on the surface.



In studies exploring film cooling, these techniques are often employed due to their ability to simply and accurately yield surface information without attempting to quantify the fluid's characteristics. Figure 7 demonstrates a sample result of spatially resolved partial pressure distributions, depicted in terms of film cooling effectiveness in a single row film cooling configuration.

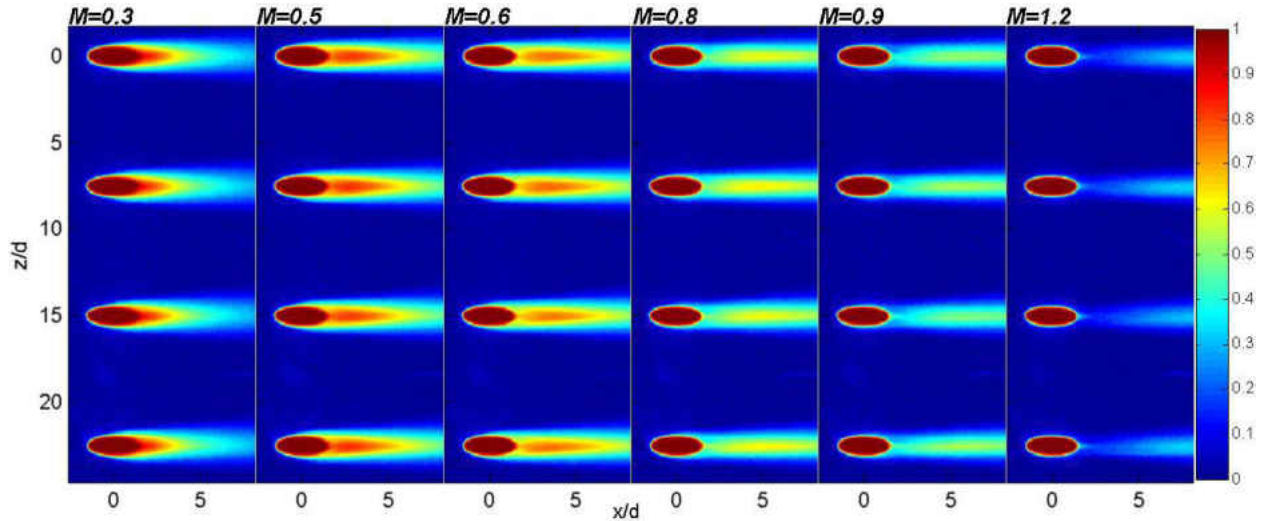


Figure 7. PSP measurements for a single row of holes indicating film cooling effectiveness as a function of mass flux ratio ( $M$ ) [12]

Another common use of these paints is on wind tunnel models as they can yield the full field pressure distribution on a novel wing structure for instance. Historic drawbacks of these paints include a limitation in response time to transient conditions, which are often not an issue for analog instruments. The two determining factors of the time response are the thickness of the paint, and diffusivity of the gas with the binder, which can be increased through porous substrates to increase the surface area[13]. However, recent developments in paint technology have allowed for response times nearing  $1\mu\text{s}$ , making them an attractive candidate for highly transient phenomena including shock tube studies and transient airfoil flow fields[14, 15].

## **CHAPTER 2. LITERATURE REVIEW**

To better approach the subjects of jets in crossflow and the diagnostic method of PLIF, it is imperative to understand a brief summary of the work conducted by other researchers and the validity of claims made. Section 2.1 focuses on comprehending the relevant timeline of LIF and outlines some of the more important results found by others. Section 2.2 is centered on the work which has gone into understanding jets in crossflows and how previous authors have elected to investigate these phenomena.

### **2.1 Laser Induced Fluorescence**

The first report of the use of gaseous fluorescent tracers can be traced back to work by Epstein in 1974 in which the valuable potential of such a quantitative non-intrusive technique was recognized[16]. Much of the preliminary work went into investigations of the characteristics of potentially excitable compounds. Work by Dimotakis and Kychakoff in the early 1980s exposed the usefulness PLIF in liquid and reactive flows respectively. Dimotakis was able to show the basic structure of a jet in crossflow, with the intuitive result that the far field region of the jet is dominated by large scale vortical structures[17].

In the case of reactive flows, intermediate species such as  $\text{OH}^*$  can be targeted to gain temporal and spatial information about a reaction. Kychakoff and Hanson demonstrated this with applications in locating flame fronts and reaction zone distributions[18-20]. This has become a widespread trend in combustion studies as a planar understanding of flame development and structure provides a plethora of results to arrive at more efficient burning strategies. Currently there are numerous well identified compounds which can be targeted in LIF, both naturally

occurring reactive intermediary species and non-reactive tracer species which must be artificially seeded into the flow.

### 2.1.1 LIF Theory

The fluorescent signal collected from a molecule with broadband spectroscopic properties can be expressed by equation (3)[21].

$$S_f = \frac{E}{hc/\lambda} \eta_{opt} dV_c \left[ \frac{X_i P}{kT} \right] \sigma(\lambda, T) \phi(\lambda, T, P, \sum_i X_i) \quad (3)$$

Where  $S_f$  indicates the fluorescent signal,  $E$  the laser energy flux [ $\text{J}/\text{cm}^2$ ],  $hc/\lambda$  the photon energy at excitation wavelength [ $\text{J}$ ],  $\eta_{opt}$  the composite efficiency of collection optics,  $dV_c$  the excitation volume [ $\text{cm}^3$ ],  $\frac{X_i P}{kT}$  the target molecular number density. The absorption cross section  $\sigma$  is a function of the excitation wavelength and molecule's temperature, and the fluorescence quantum yield  $\phi$  is recognized to be a function of excitation wavelength, molecular temperature, pressure, and all the excited species' mole fractions[21].

While equation (3) demonstrates a highly complex multi-parameter function, experimental configuration choices dramatically reduce the complexity. In the experiments in this report the jet and freestream have matching temperatures and due to the low subsonic flow speeds, negligible pressure gradients exist. The isobaric, isothermal assumptions coupled with a spatially monochromatic excitation source imply that  $\sigma$  is spatially fixed. Additionally, Thurbur showed that for relatively high acetone partial pressures, mixture composition played a minimal role in fostering nonlinearity of the fluorescence yield, implying that  $\phi$  is spatially fixed as well[21]. Making a further assumption of linear optics results in no functional dependence on  $\eta_{opt}$ . It is finally recognized that the product of the excitation volume and energy density

variations due to volumetric distortion remains fixed, therefore yielding the simple relationship in equation (4), where E is solely a function of the sheet non-uniformities and absorption effects.

$$S_f \propto E * X_i \quad (4)$$

For select compounds,  $\sigma$  and  $\phi$  have been characterized by their functional dependence on their respective parameters. This has allowed for full field characterizations of mole fraction, temperature, and pressure distributions. Examples of the methodologies required for these systems can be found in section 2.1.3. Velocity measurements using PLIF have been proposed by considering Doppler-shifts in the absorption line shape function; however, PIV has been recognized as a simpler and more accurate technique[22].

### *2.1.2 Acetone Photophysics*

Due to the nonreacting nature of the jet in crossflow, a tracer molecule must be selected and seeded into the flow to allow for jet concentration profiling. Acetone ( $C_3H_6O$ ) has been identified as an ideal compound based on many of its physical and fluorescent characteristics. The physical merits of acetone are its low toxicity, high vapor pressure at room temperature, and inexpensive nature. As the fluorescence scales with number density, high vapor pressures allow for higher saturation limits, and therefore a higher signal level.

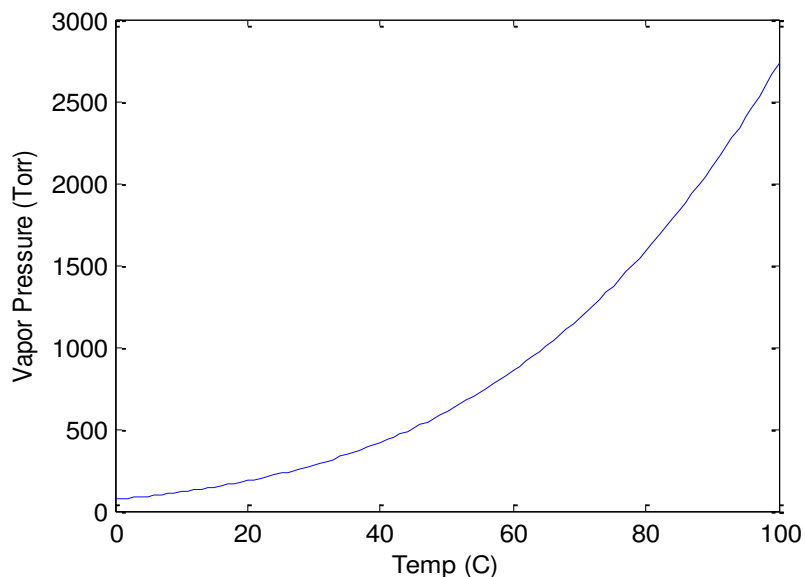


Figure 8. Vapor pressure as a function of temperature for acetone

However, even more appealing are its photophysical characteristics which were largely characterized by Lozano[23]. Fluorescence occurs from the first excited singlet state  $S_1$  as a result of excitation from the ground electronic state  $S_0$ . Since vibrational effects have only been observed in low pressure and temperature cases, considering the lowest vibrational level of each state is sufficient[24]. Rapid crossing from the excited  $S_1$  state to the excited triplet state  $T_1$  limits the fluorescence, which allows phosphorescence to occur from  $T_1$  on a significantly longer time scale[23]. Figure 9 demonstrates the excitation and emission means found in LIF.

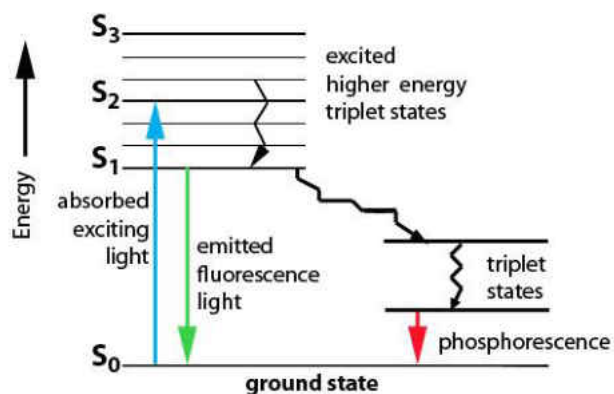


Figure 9. Excitation and emission diagram of electronically excitable species[25]

It is understood that the fluorescence process takes approximately 4ns for acetone while phosphorescence is expected to take roughly 200 $\mu$ s. However, the presence of O<sub>2</sub> rapidly quenches the phosphorescence which therefore can be neglected. The extremely short fluorescence lifetime of acetone vapor allows for the virtually instantaneous imaging of flow provided a short enough laser pulsewidth is used. Based on the velocities of the jets used in this study, the minimum potential spatial resolution due to the laser pulsewidth is approximately 0.2 $\mu$ m.

As demonstrated in figure 10a, the absorption spectrum found by Lozano is very broadband in nature with a peak in the near-UV wavelength region. In the experiments of this study, 266nm laser light was used, which lies near the peak of the absorption feature. Higher absorption efficiencies allow for greater signal strength and therefore greater experimental accuracy. Alternatively, the emission spectrum of the excited state exists in the visible spectrum for ease of capture with a standard unintensified CCD camera. Both of these characteristics make acetone highly attractive for use with the previously owned components (Nd:YAG Laser and visible spectrum CCD camera), and ultimately lead to its selection as the tracer of choice for these studies. Additionally, the wavelength shift between absorption and emission spectra allows for ease of filtering when recording the fluorescent signal.

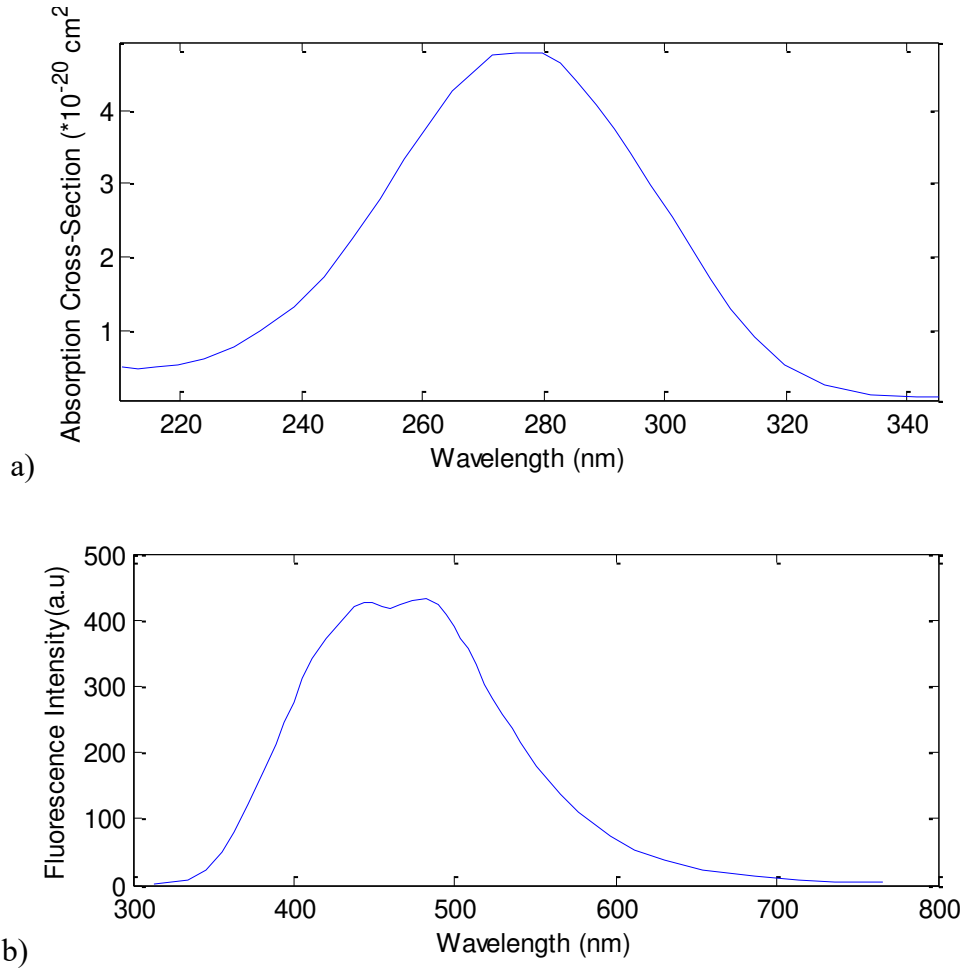


Figure 10. a) Absorption feature of Acetone, b) Fluorescent yield spectrum of Acetone [23]

The final desirable characteristic of acetone vapor is the highly linearity of fluorescence as a function of both excitation energy and acetone number density. With regard to excitation energy, Lozano proved linearity for fluxes of 200-1200mJ/cm<sup>2</sup>, where the flux in this study was approximately 400 mJ/cm<sup>2</sup>. Without these linear properties, reduction of equation (3) and characterization of the laser profile become much more challenging.

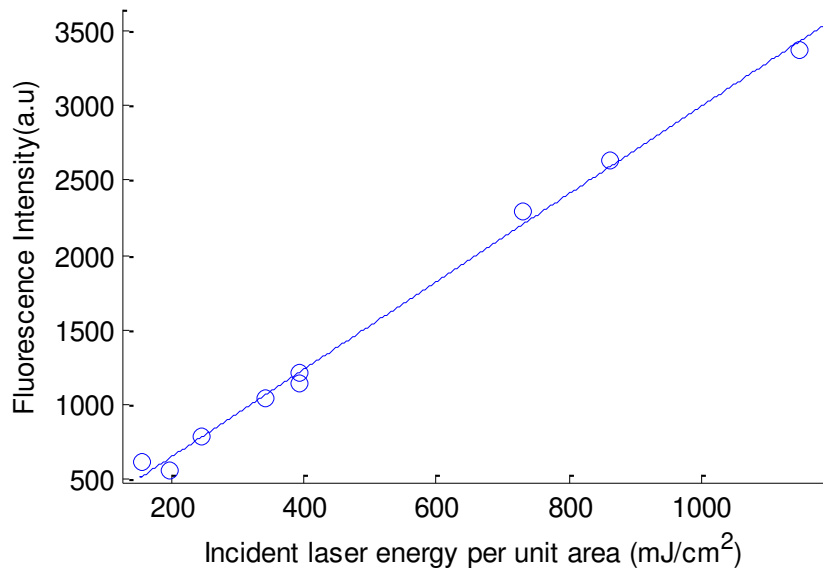


Figure 11. Linear fluorescence as a function of fluence [23]

### 2.1.3 LIF Measurements of Pressure and Temperature

Although unused in the present work, LIF holds the potential to provide temperature information as well as pressure maps of various fluid dynamics systems. The underlying fluorescence equation demonstrates the relationship of the fluorescence to vary with pressure and temperature exclusively through the molecular density, fluorescent yield, and absorption cross section. Through careful probing, the functional dependence of these parameters on pressure, temperature, and excitation wavelength for many tracer compounds such as acetone, iodine, naphthalene, toluene, and biacetyl has been established [23, 26-28]. Depending on the configuration, differing methodologies may be used. In determining the temperature of a system, using either one or two discrete laser wavelengths have been demonstrated as effective. In a system where the tracer is spatially non-varying and the pressure is uniform, a single excitation wavelength can be used according to equation (5).



$$S_f \propto \frac{1}{T} \sigma(T) \phi(T) \quad (5)$$

In the more likely case of tracer density varying with location, a dual-wavelength strategy can be employed. By capturing the fluorescent signals separately from the same tracer species using two different excitation wavelengths, the ratio of the fluorescent signals can yield temperature information of the field. As shown in Equation (6), the number density cancels in the ratio of fluorescence signals resulting from excitation at different wavelengths, assuming the concentration distribution is identical in the two different collections of the fluorescent signal.

$$\frac{S_{f,\lambda_2}}{S_{f,\lambda_1}} \propto \frac{\sigma(\lambda_2,T)\phi(\lambda_2,T)}{\sigma(\lambda_1,T)\phi(\lambda_1,T)} \quad (6)$$

Relationships between the wavelength specific fluorescent signals have been characterized for various tracers, and can directly yield a temperature. Figure 12 gives a sample of the fluorescent signal ratio for common excitation wavelength pairs in an isobaric system.

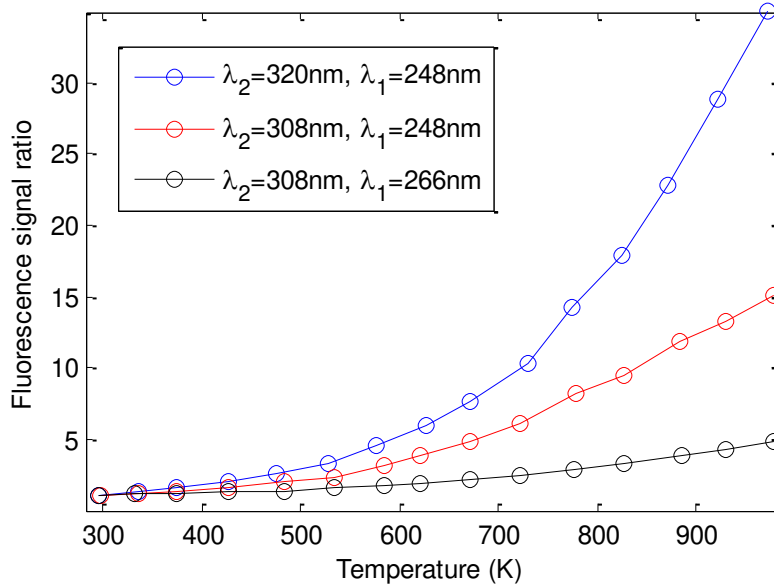


Figure 12. Fluorescent signal ratio as a function of temperature for select wavelength pairs for acetone vapor [21]

Once the temperature distribution has been obtained, it can be used in conjunction with a fluorescent signal from either of the two excitation wavelengths to obtain the number density of the tracer. Similarly, if the temperature is previously known or is constant across the field, a dual-excitation strategy can yield the pressure distribution in the flow field.

An exceptional demonstration of PLIF thermometry can be seen in work by Yoo[29]. In a shock tube uniformly seeded with toluene, Yoo was able to make use of a single line strategy, in conjunction with pressure assumptions to accurately extrapolate temperature profiles. Due to the extremely short fluorescence lifetime and laser pulsewidth, temperature profiles across highly transient phenomena, such as a moving shock wave were obtained.

## **2.2 Diagnostics of Jets in Crossflow**

While the focus of this study is limited to an investigation of the concentration profile of a jet in crossflow, much work has previously been done to address other aspects of jets in crossflow. Most of the previous work has focused on 90° inclination angle jets at high jet-to-freestream velocity ratios.

### *2.2.1 Structural Investigations*

The earliest complete optical characterization of the structure of a jet in crossflow was performed by Fric in 1990[30]. Although previous studies identified components of the jet in crossflow, Fric investigated the primary four resulting vortical structures: shear layer vortices, counter rotating vortex pair, wall attached horseshoe vortices, and wake vortices and their resulting interactions[31]. Identification of these structures was performed by using smoke wire flow visualization and also through the use of hotwire testing. Fric came to the conclusion that the vortical structures observed were largely a result of the boundary layer properties of the jet and along the wall, and not due to the previously accepted analogy describing the jet as a

cylinder in a crossflow. With respect to the leading edge of the jet, the boundary layer is known to separate and accelerate around the jet, skewing the shear layer leading to pressure gradients in the shear layer[32]. This mechanism leads to leading edge vortex rollup as seen in figure 13a. Additionally, Fric later asserted that the wake vortices were caused by the crossflowing boundary layer[31]. Figure 13 depicts results from his smoke wire testing by demonstrating the leading edge vortices, horseshoe vortices, and wake region instability.

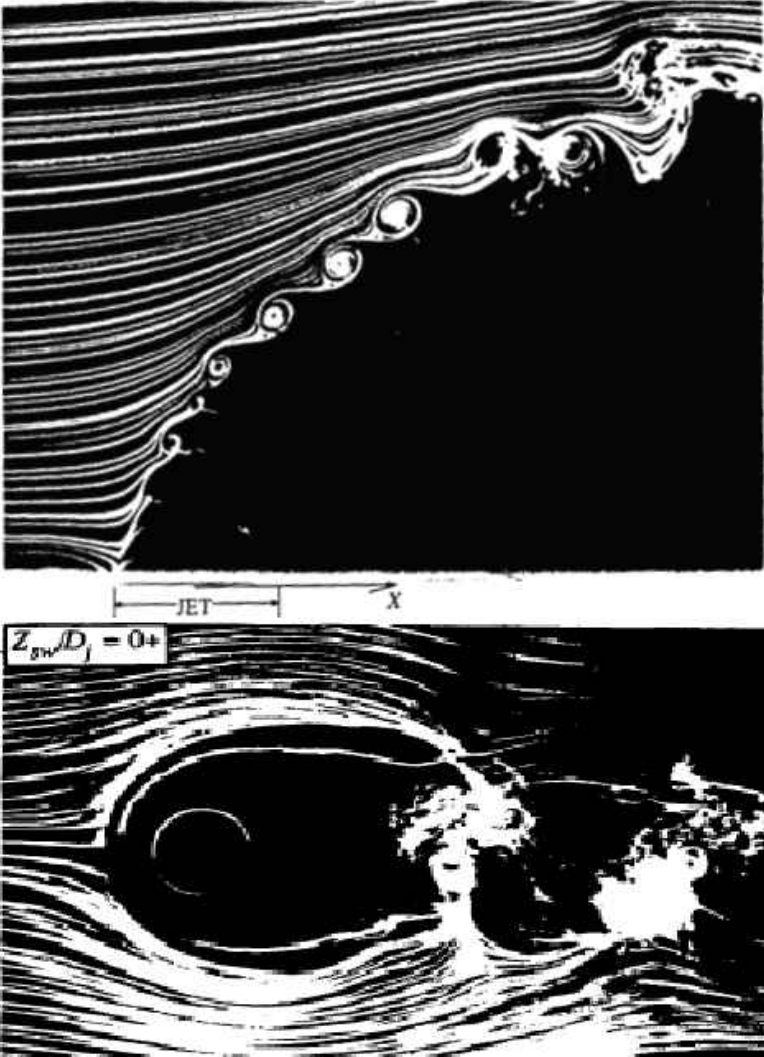


Figure 13. Top) smoke trails impinging on leading edge of jet. Bottom) top-down view showing wake region and horseshoe vortices [30]

Additional work in characterizing the upstream recirculation region and the horseshoe vortex-boundary layer interaction was performed by Krothapalli in 1990[33] and Kelso & Smits[34, 35]. The wake vortex system has been characterized in many studies including Kelso and Lim (1996)[35], Fearn and Weston (1974)[36], and McMahon, Hester, and Palfery (1971)[37], who originally asserted that the wake occurs as in the case of a wake off of a bluff body in a freestream. The initial claim of similarities to a bluff body were drawn by McMahon after noticing the vortex shedding mechanics with similar Strouhal numbers as in the bluff body case. However as mentioned, Fric proposed a different explanation for the phenomena. Finally, the vorticity dynamics of the jet itself can be explored in the studies of Coelho & Hunt (1989)[38] and Needham, Riley & Smith (1988)[39] and more recently Morton and Ibbetson (1996)[40] who specifically investigated the effect of vorticity in impacting the jet deflection angles.

The more recent advent of LES and DNS modeling of jets in crossflow has allowed for further physical insight into the mechanics of observed features. Muppidi and Mahesh (2007) conducted a DNS study in which experimental conditions from Su and Mungal are replicated and results are cross validated in terms of velocity and turbulent intensity profiles[41, 42]. In one of the few studies on low velocity ratio jets, Sau found that hairpin vortices form along the leading edge as opposed to the rolled up vortices expected at higher velocity ratios[43]. This effect occurs when the vorticity of the crossflowing boundary layer overwhelms the opposite vorticity of the leading edge of the jet.

### *2.2.2 Velocity Profiling*

Velocity profiling has perhaps been the simplest characterization to achieve in jets in crossflow experiments. Numerous studies have taken advantage of the technologically simple

hotwire anemometry technique to make measurements of the velocity distribution, with the ability to gain magnitude information[36]. As is pertains to the freejet studies presented in chapter 4, pitot probe measurements were employed in a round freejet at downstream locations by Labus[44]. He was able to clearly show that a uniform velocity profile exists along the axis in the potential core region, and that the centerline velocity monotonically begins to decrease in a logarithmic profile downstream of the potential core. Additionally an increase in jet turbulence, as a consequence of increasing Reynolds number, has been shown to increase the near field spread angle of the jet. Although these conclusions are specific to a freejet, the same phenomena will contribute to the behaviors of a turbulent jet in crossflow.

PIV has allowed for velocity and magnitude characterizations of the jet in a 2d plane [42, 45]. Lanitis used stereoscopic PIV to investigate the CVP in the flow, the structure of which is understood to play a significant role in the interaction of the coolant jet and wall in film cooling configurations [46]. Stereoscopic PIV involves the use of two cameras and allows the possibility of gaining out of plane information to obtain all three velocity components in a flow. This is highly useful in many configurations, especially transient applications. Developments in CFD have allowed for the full field 3d modeling of flow and velocity distributions , and are highlighted by work by Mahesh and Kawai[32, 41, 47, 48]. Cross validation of PIV results from Baresh and Santiago through DNS simulations performed by Chai and Mahesh demonstrate strong velocity profile agreements relating to a jet in supersonic crossflows[49-51]. Compressibility effects are known to introduce factors not seen in low speed freestreams, and require a more complex physical understanding.

### 2.2.3 Trajectory Scaling

Of primary interest in the elementary investigations of this report is the predictable scaling of the jet's trajectory as a function of orientation and velocity conditions. In the world of film cooling, these relationships are intimately coupled to the film's effectiveness. With regard to the jet's dependence on flow conditions, it can and has been argued that the trajectory depends on flow ratios between the freestream and the jet.

However, aside from velocity ratio relationships, it has been shown that the underlying physics responsible for the jet trajectory is intimately related to the entrainment of the jet with the crossflowing fluid[52]. Therefore differing entrainment characteristics are expected to yield differing trajectories, independent of velocity ratios. From a dynamics perspective, it is logical that either the velocity ratio, the mass flux ratio, or the momentum flux ratio will strongly influence the jet's trajectory. These parameters have been defined as follows respectively.

$$r = \frac{u_{jet}}{V_{\infty}} \quad (7)$$

$$M = \frac{\rho_{jet} * u_{jet}}{\rho_{\infty} * V_{\infty}} \quad (8)$$

$$J = \frac{\rho_{jet} * u_{jet}^2}{\rho_{\infty} * V_{\infty}^2} \quad (9)$$

Previous authors have made investigations into how trajectories scale and have arrived at conflicting reports. In particular significance to this study, Smith established both the near field and far field scaling of the jet trajectory with the jet-to-freestream velocity ratio and hole diameter,  $rd$ . When assuming the following simple form:

$$\left(\frac{y}{rd}\right) = A \left(\frac{x}{rd}\right)^n \quad (10)$$

for strong transverse jets the value of  $n$  has been reported to fall between 0.23 and 0.38, and  $A$  ranges from 1.2-2.6[53, 54]. However, this functional relationship depending on  $rd$  has not been able to completely describe data sets. Consider the following results by Smith and Mungal in their 1998 investigation of orthogonal jets with a velocity ratio ranging from 5-25[55].

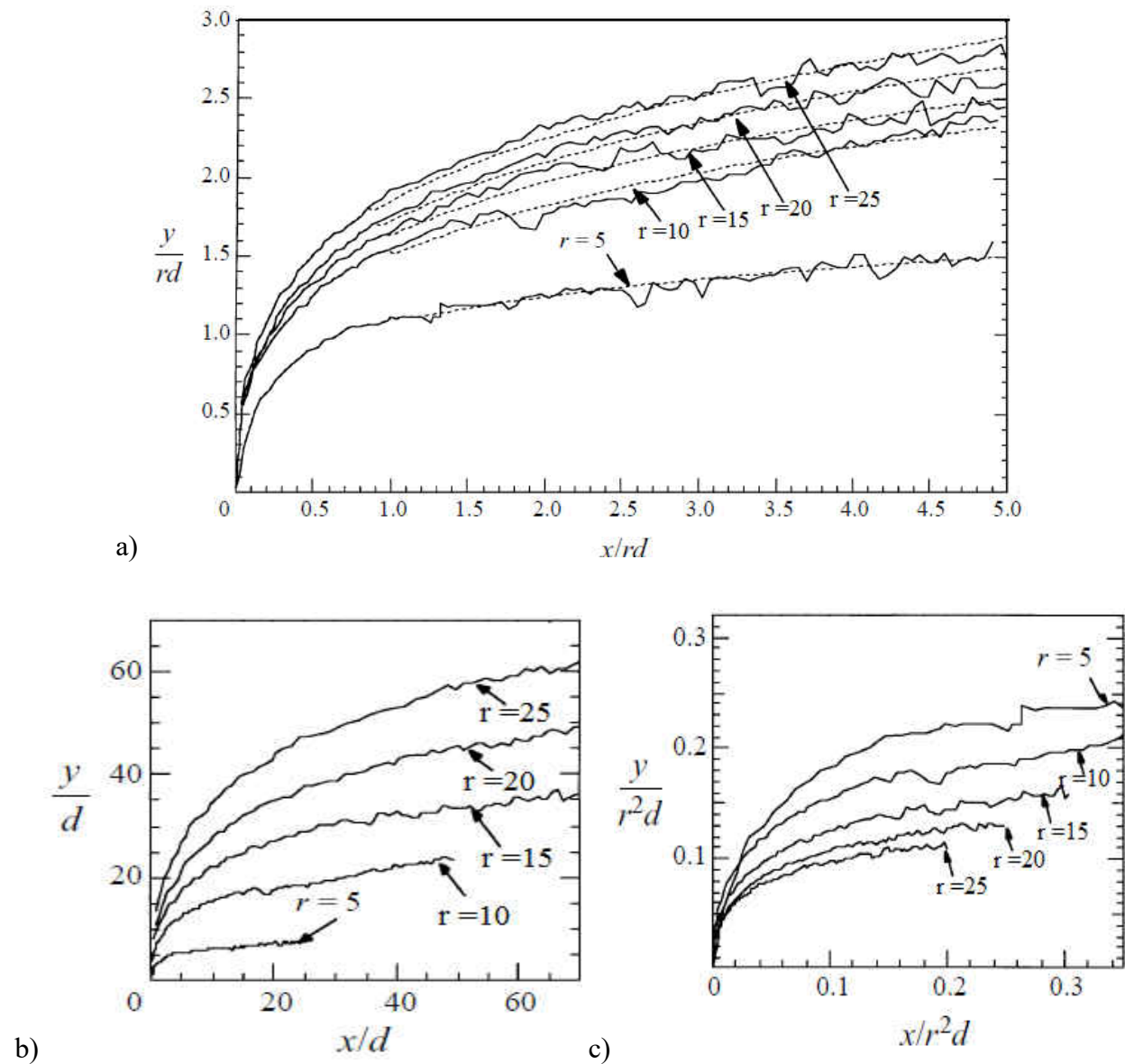


Figure 14. Trajectory results for 90° jet as reported by Smith and Mungal [55]

In their study, is apparent by the lack of trajectory collapsing that the jets do not perfectly scale by  $rd$ , as the data by Pratte and Baines did[56]. Smith and Mungal found that  $rd$  scaling under-collapsed the jets, while  $r^2d$  scaling over-collapsed the jets. It was postulated that discrepancies may be the result of boundary layer influences as Pratte and Baines used a pipe extending into the freestream. However, others have postulated that  $r^2d$  scaling better collapses the data, indicating that the momentum flux is the responsible parameter[57]. Therefore based on the myriad of conflicting results, in the simplest trajectory model it can be summarized that the trajectories scale as some combination of both mass and momentum fluxes, depending on the exact boundary layer, and velocity profile conditions.

Distinction can additionally be made between proposed near field and far field regions of the jet, and consequently different trajectory functions can be argued in each region. Hasselbrink and Mungal employed similarity theory to delineate near field and far field trajectories in equations (11) and (12) respectively[53].

$$\left(\frac{y}{rd}\right) = \left(\frac{2}{c_{ej}} \frac{x}{rd}\right)^{0.5} \quad (11)$$

$$\left(\frac{y}{rd}\right) = \left(\frac{3}{c_{ew}} \frac{x}{rd}\right)^{0.33} \quad (12)$$

Although the definition of what constitutes the far field region is slightly unclear, Smith and Mungal suggest a far-field definition of  $x/r^2d > 0.3$  [55]. In these equations  $c_{ej}$  and  $c_{ew}$  represent entrainment coefficients of the jet and wake regions respectively. Even more complex



functional relationships are suggested by Muppidi and Mahesh as they incorporate momentum in the jet and crossflow boundary layers[58]. They proposed a length scale to parameterize the relative inertia of the jet and crossflow which incorporates both boundary layer thickness and jet velocity profiles, and found that this proposed length scale leads to more complete scaling of the jet trajectory. Another note regarding the predicted trajectory in equations 11-13) is that the density ratio is unaccounted for in this model. As the density ratio impacts both the mass and momentum flux ratios, it is expected that the trajectory will depend on this as well. Finally, it is worth noting that jet penetration hasn't been described to linearly vary with any of the physically elementary relationships. Since individual particle acceleration is occurring in two dimensions in the presence of nonlinear gradients, it is understandable that the trajectory likely will be non-linear as well.

#### *2.2.4 Geometry Considerations*

The immediately preceding sections have described phenomena and studies which are most closely associated with an ideal round jet in crossflow. However, many other factors can have a strong effect on the behavior of the jet. The physical geometry of the jet hole is a topic which has been extensively investigated as it has direct potential to greatly affect film cooling effectiveness levels with no conditions imposed on altering the freestream. Figure 15 demonstrates proposed jet configurations, specifically tailored to address film cooling needs. In particular, fan shaped holes promote lateral expansion of the jet along the wall surface downstream of the hole.

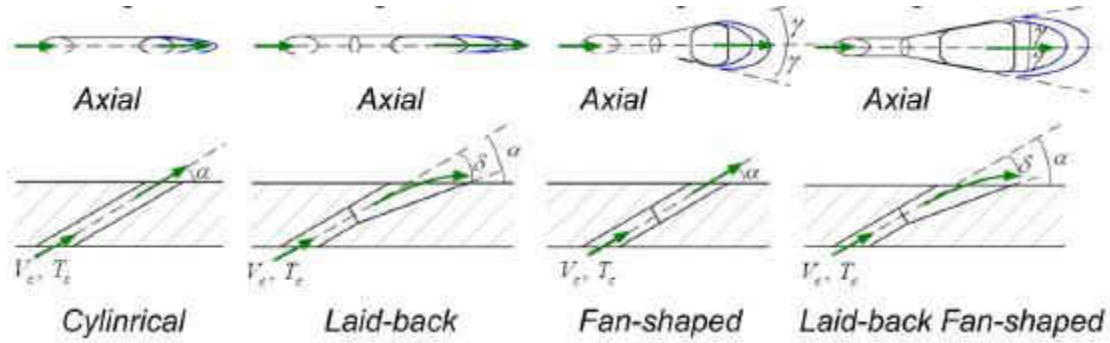


Figure 15. Hole geometries proposed for use in film cooling [59]

Additionally, select experimental studies have investigated other geometries, such as elliptical and rectangular cross sections[60, 61]. Fan shaped holes are expected to deliver better film spreading by introducing a dispersion angle to the coolant fluid. Furthermore, the introduction of a compound angle has been repeatedly shown to similarly increase lateral spreading of the jet[62].

Complex phenomena such as crossflow at entrance effects have also been studied and characterized, which contribute to a complete physical understanding of jet in crossflow interactions[63]. As an illustration for the need of these types of studies Andreopoulos discovered that due to adverse pressure gradients, the crossflow served to block part of the exit jet and therefore increase the peak velocity by a factor of two as compared with the case no freestream[64]. Finally, effects of jet swirl have been considered and are believed to play a role in the penetration characteristics of the jet[65].

The CVP is understood to hold significance in applications of film cooling. Due to the vortical structure, the hot freestream wraps around the sides of the jet and is sucked underneath of the jet between the bulk of the coolant and the wall, while simultaneously lifting the jet, mitigating the purpose of the coolant jet. Due to this phenomenon, work has been conducted in controlling and reducing these vortices. Kusterer investigated an arrangement of two jets at

compound angles chosen to cancel out the vortex generation of each other[66]. Along similar lines, Heidmann proposed and simulated a concept to modulate the CVP. His proposal included adding auxiliary round holes downstream of the primary coolant hole to terminate the CVP[67]. Heidmann and Rigby later added a delta vortex generator downstream of the flow via simulation and showed its effectiveness in eliminating the upwash effect of the CVP[68].

### **2.3 Mass Heat Transfer Analogy**

One critical component for making the concentration results of this study applicable to film cooling is the linkage between the concentration and the film cooling effectiveness. Han provides a concise explanation of the mathematical basis for this linkage, which will be briefly summarized in this section[59]. First let us consider the governing equation of heat transfer in a two-dimensional turbulent boundary layer over a flat plate. [69]

$$\bar{u} \frac{\partial \bar{T}}{\partial x} + \bar{v} \frac{\partial \bar{T}}{\partial y} = \frac{\partial}{\partial y} \left[ (\alpha + \varepsilon_T) \frac{\partial \bar{T}}{\partial y} \right] \quad (13)$$

In equation (13),  $\bar{u}$  and  $\bar{v}$  correspond to the average velocity in the x and y direction respectively,  $\alpha$  indicates the gas thermal diffusivity and  $\varepsilon_T$  is the turbulent thermal diffusivity. Assuming the jet has some contact with the wall, thermal boundary conditions can be imposed as follows:

$$y = 0: \frac{\partial T}{\partial y} = 0, T = T_{aw} \quad (14)$$

$$y > \delta: T = T_{\infty} \quad (15)$$

$$x = 0: T = T_{coolant} \quad (16)$$

for the adiabatic wall, freestream, and initial coolant temperature boundary conditions respectively in equations (14), (15), and (16).

Secondly, we can write the governing equation of mass transfer in a two-dimensional turbulent boundary layer for concentration in terms of the mass fraction,  $C$ . [59]

$$\bar{u} \frac{\partial C}{\partial x} + \bar{v} \frac{\partial C}{\partial y} = \frac{\partial}{\partial y} \left[ (D + \varepsilon_M) \frac{\partial C}{\partial y} \right] \quad (17)$$

Where  $D$  indicates the mass diffusion coefficient and  $\varepsilon_M$  is the turbulent mass diffusivity. Again, boundary conditions can be imposed as follows:

$$y = 0: \frac{\partial C}{\partial y} = 0, C = C_w \quad (18)$$

$$y > \delta: C = C_\infty \quad (19)$$

$$x = 0: C = C_{coolant} \quad (20)$$

for the solid wall, freestream mass fraction, and initial coolant fluid mass fraction boundary conditions respectively in equations (18), (19), and (20). In equations (15) and (19),  $\delta$  corresponds to the film thickness.

Therefore, due to the highly parallel nature of these governing equations (13) and (17), if the turbulent Lewis number is equal to unity, then both the nondimensional solutions of temperature and concentration will be identical. In general, Lewis numbers of one can be assumed in the presence of highly turbulent flow fields. High Reynolds numbers and the presence of many secondary contributions to turbulence promote the validity of this assumption[59]. However, in the viscous sublayer this analogy will break down as turbulent diffusion is inhibited and viscous diffusion dominates. The thermal diffusivity of standard air is given as  $\alpha=22\text{mm}^2/\text{s}$  and the mass diffusivity of acetone vapor in air is  $D=11\text{mm}^2/\text{s}$ . Therefore in these experiments, the Lewis number for the two gas streams mixing will be 1-2, allowing the mass/heat transfer analogy to be applied with minimal error[70]. Additionally, the viscous sublayer generally only comprises approximately 1% of the boundary layer, leading to negligible

error in the case of analogy breakdown. Since the solutions are equivalent, at the surface region we can express the film cooling effectiveness as follows:

$$\eta_{film} = \frac{C_{\infty} - C_w}{C_{\infty} - C_{coolant}} = X_{wall} \quad (21)$$

Where  $X_{wall}$  represents the normalized concentration distribution found through PLIF at the wall. This significant result provides the missing connection between coolant jet concentration maps and corresponding thermal results. More explicitly, if the concentration distribution of the coolant jet can be quantified, the thermal effectiveness of film cooling a wall can also be quantified. This analogy is very commonly used in PSP studies involving film cooling, as a species partial pressure (typically oxygen) can be mapped on the surface and correlated to the cooling effectiveness.

## CHAPTER 3. EXPERIMENTAL SETUP

### 3.1 Wind Tunnel

One key component of an experiment involving a jet in a crossflow is having a high-quality crossflow with specific requirements. The first requirement is that there should be a sufficient test section width to ensure an absence of sidewall effects. The channel height must have a similar requirement so that the only wall effect is the boundary layer on the jet-injection wall. Secondly, the crossflow should be in the low subsonic regime and have a density relatively near the jet density to eliminate significant buoyancy effects.

#### *3.1.1 Tunnel Construction*

With the requirements in place, a previously designed water tunnel with a 127x228.6mm test section cross section was modified to allow for a sufficient crossflow source. Figure 16 depicts the wind tunnel setup and important added features.

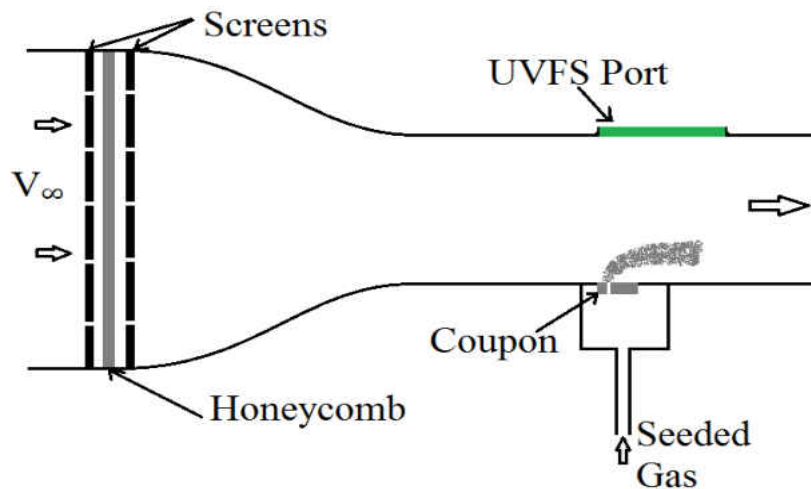


Figure 16. Schematic of the wind tunnel configuration

Flow conditioners were added to improve flow uniformity, a fused silica port allows for the selected laser wavelength to enter the test section, and 4 Dayton 1TDR7 blowers were added

to drive the flow with standard atmospheric air. The wall surface through which the jet is introduced is composed of standard aluminum, which introduced imaging difficulties described later. Figure 16 shows the standard construction and arrangement of the wind tunnel. As flow velocity was not a primary concern, a diffuser was not implemented post test section.

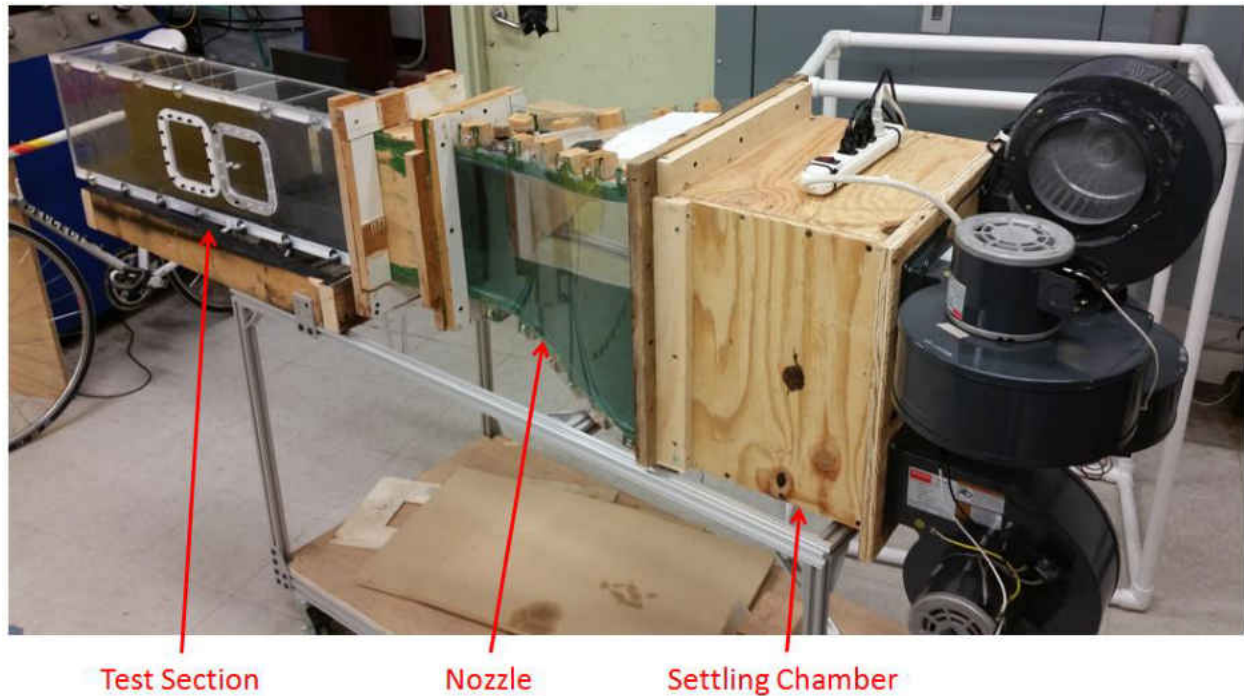


Figure 17. Wind tunnel used in JIC testing

The velocity profile was characterized through the use of a boundary layer pitot probe and the results can be seen in figure 18. Although the flow does not demonstrate a perfect profile in keeping with boundary layer theory, the velocity distribution has a high enough quality to provide reasonable data for the jet in crossflow. The slight velocity growth away from the wall was determined to results from an upstream lip which was part of a boundary layer suction unused in this study. The velocity points are portrayed with the appropriate error bars of  $\pm 0.15\text{m/s}$ , owing to the resolution of the pressure transducer used.

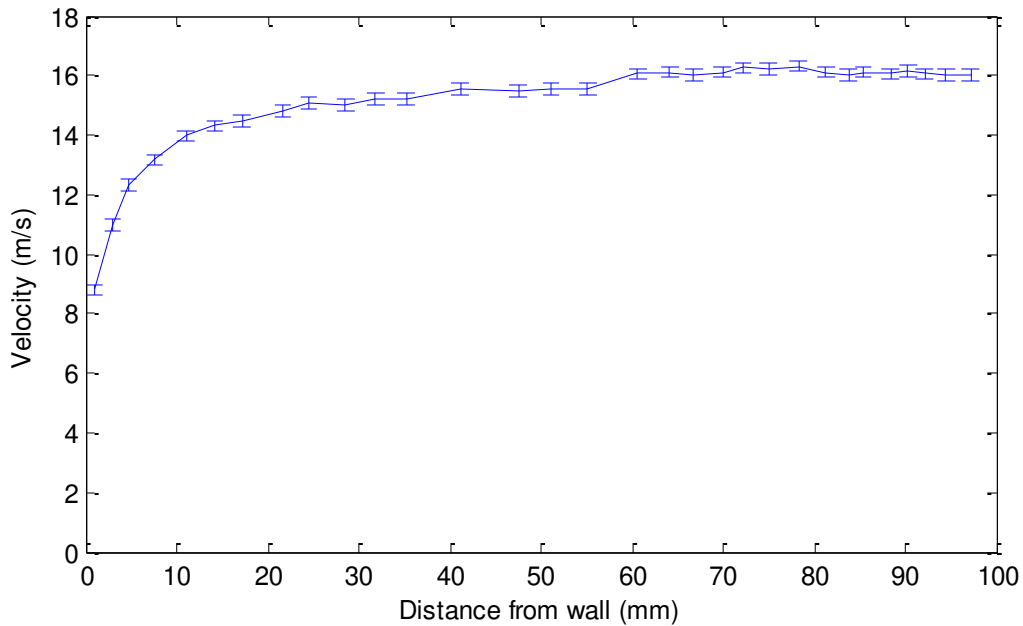


Figure 18. Velocity distribution in the test section as a function of distance from the wall

Although the velocity profile was held constant in these experiments, the jet’s trajectory will certainly be a function of the freestream boundary layer shape and thickness. Future work with this experimental setup should include use of the boundary layer suction to remove the boundary layer, as well as possible modifications to explore the effect of changing the velocity profile near the wall.

### 3.1.2 Coupon Development

The preexisting water tunnel test section was equipped with a mounting system for interchanging removable coupon inserts. This allows for the quick turnaround times between runs when a different hole geometry is desired. For this study, coupons of a fixed thickness and fixed hole diameter of 3mm was used for a variety of hole inclination angles. One limitation of this configuration is that with varying inclination angles, the L/D ratio (ratio of the length of the hole to the diameter of the hole) is changed as well. Across the angles chosen for this study, the



L/D ratio varies from 3.8 up to 7.6. Therefore the velocity distribution in the jet is expected to change slightly as the flow develops further for larger L/D values. As reported, the jet velocity profile is expected to play a role in the jet trajectory slightly[58].

For the experiments presented, a single hole is used. However in most applications multi-hole, multi-row configurations are used. Introducing multiple rows will affect the flow field both thermally as well as in terms of velocity and concentration distributions. Specifically, the boundary layer will be completely altered by upstream rows, potentially leading to different penetration and dispersion characteristics of the downstream rows. Further work should include an investigation of single-row multi-hole configurations and multi-row configurations to better understand the concentration distributions of a jet in crossflow in a more accurate film cooling configuration. A CAD design of a sample coupon is presented in the appendix. Due to the relatively small size, the coupons used for these types of experiments are ideal candidates for 3D printing, and allow for the extremely unique possibility of moving from conceptual idea to final testing in a matter of hours.

### *3.1.3 Seeding System*

In order to introduce acetone into the jet stream, a seeding system similar to the system used by Ritchie [71] was employed. By simply bubbling atmospheric air through a graduated cylinder full of liquid acetone, the vapor was uniformly distributed into the flow. For the tests presented, the airflow rate supplied to provide the jet was approximately 2-10 L/m before being bubbled through 4in of liquid acetone to seed the air with acetone vapor. In order to quantify the acetone-air mixture, PSP measurements were first attempted to measure the partial pressure of the oxygen in the mixture. However, due to an interaction between the acetone vapor and the paint, concentration results were inaccurate demonstrating an increase in the oxygen

concentration with the introduction of acetone into the flow, which was recognized to be physically incorrect. Therefore simple testing relying on the measuring the volume of acetone evaporated in a given time span was the method chosen to determine the final molar concentration of acetone to be  $23.5 \pm 1.28\%$ . Since the airflow supply showed small fluctuations ( $\pm 3\%$ ), and the tests were conducted in short timespans ( $< 10\text{s}$ ), variations in acetone mole fraction of the seeded mixture is understood to be negligible. For comparison, the theoretical saturation limit for acetone at room temperature is reported as  $25.6\%$ , indicating a strong effectiveness of the acetone seeder used.

Accurate jet mixture concentration is imperative as it allows for the calculation of jet density, which is theorized to play a role in the trajectory and mixing of the jet via the blowing and momentum flux ratios. The acetone/air mixture used in the jet was determined to have a density and dynamic viscosity of  $1.51 \text{ kg/m}^3$  and  $1.02 \cdot 10^{-5} \text{ kg/m}\cdot\text{s}$  respectively. Finally, although the phase transition of acetone from a liquid to gas requires an energy transfer, the resultant temperature of the jet was measured to consistently fall within the measurement accuracy ( $< 0.1\text{K}$ ) of the freestream temperature. Therefore no temperature error is introduced when assuming an isothermal system for conversion between fluorescence and concentration.

### **3.2 Optical Setup**

Figure 19 illustrates a basic schematic for the experimental setup used in the jet in crossflow configuration. Note the acetone seeding mechanism is displayed, and also that the laser sheet propagates perpendicular to the jet injection wall.

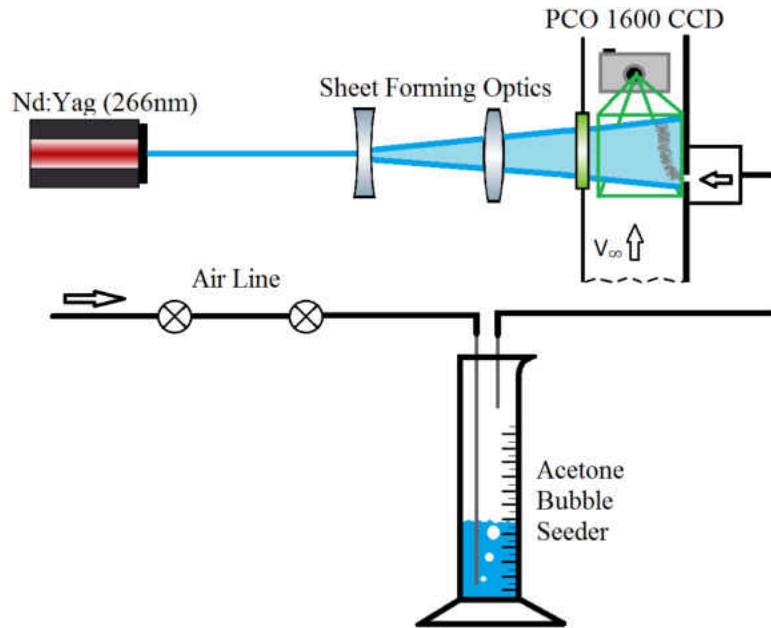


Figure 19. Simplified schematic of the full experimental setup

### 3.2.1 Laser Characterization

The excitation source used was a Quanta-Ray Lab 190 laser with a 10Hz repetition rate. The fundamental mode of the laser generates 1064nm pulses with a FWHM pulsewidth of approximately 8ns. Peak laser power of the fundamental mode was measured at 1J/pulse. The 4th harmonic 266nm wavelength was generated by 2 BBO frequency doubling crystals used in succession, and a pair of dichroic mirrors to promote a single-wavelength source, all internal to the laser system. After frequency conversion and separation, the average pulse intensity was approximated at 87 mJ/pulse using a Coherent J-50MB-YAG-1535 energy meter. However, the laser was subject to variations of approximately 3% in individual pulse power, as is demonstrated in figure 20. Due to an inability to continuously monitor pulse power, the images can be corrected for laser power fluctuations by realizing that the fluorescence correlates directly to the pulse power.

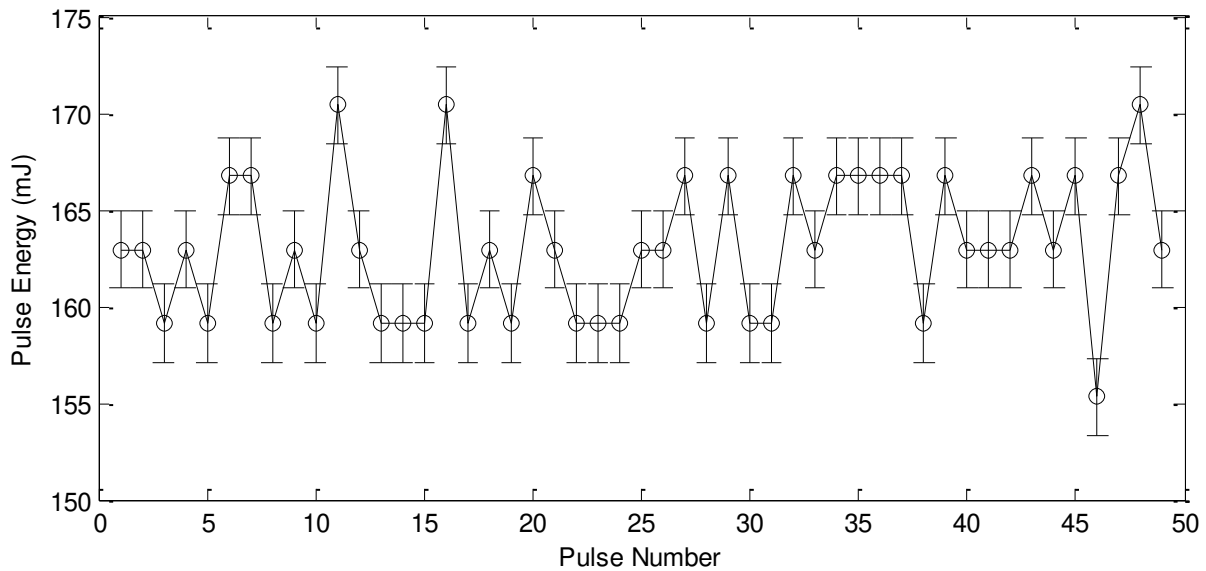


Figure 20. Sample Laser Pulse Power fluctuation for 1064nm wavelength

The laser beam is subjected to an aperture to use only the relatively uniform core of the beam, which is then passed through two cylindrical lenses to form a sheet. At the measurement location, the sheet thickness is  $400\mu\text{m}$  and the fan height is  $63.5\text{mm}$  with a divergence angle of  $2^\circ$  in the sheet transverse direction. Sheet divergence in both the transverse and out of plane direction leads to a non constant  $dV_c$ , but is accounted for in equation (3) by competing effects in the energy density.

### 3.2.2 Camera Information

A PCO 1600 CCD camera was used with a resolution of  $1600 \times 1200$  pixels resulting in a minimum voxel size of  $79 \times 79 \times 400\mu\text{m}$  for the camera configuration used in testing with a  $62\text{mm}$  lens. The voxel size indicates the maximum possible resolution obtainable; however, the actual resolution is expected to be significantly larger. A resolution target should be used to determine the true resolution capabilities of the camera at the given distance. However, the laser sheet thickness is understood to be the limiting volumetric resolution factor. The camera was oriented

orthogonally to the sheet where images were collected at 10 fps with an exposure time of 100ms, synchronously with the laser pulses. Due to the laser pulsewidth and fluorescence lifetime both existing on the order of ns, advanced timing between the camera and laser were not required, as pulses always fell within the relatively large framing window.

Figure 21 depicts the quantum efficiency curve of the camera used. As the quantum efficiency of the camera is highest over the wavelengths emitted by the fluorescing acetone, the risk of IR or UV signals being mistaken as PLIF signal is reduced significantly.

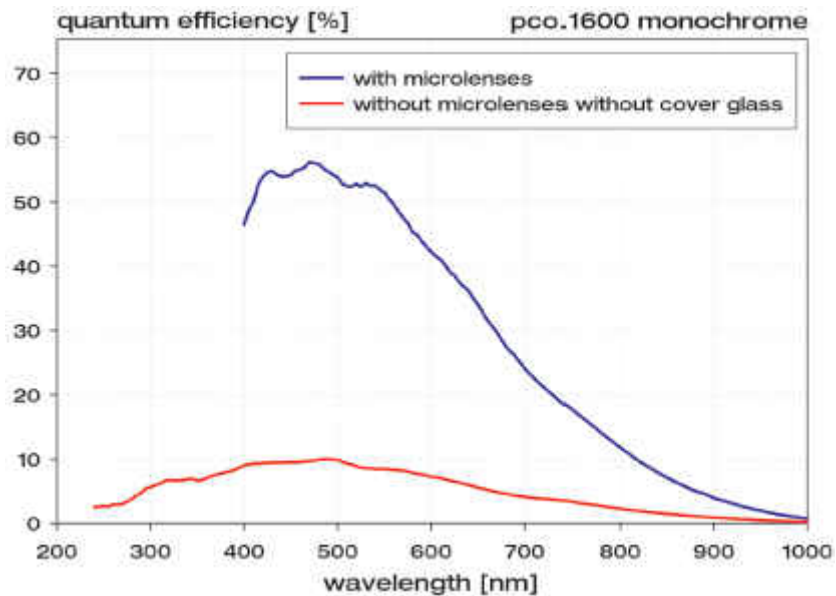


Figure 21. Quantum efficiency vs. wavelength for PCO 1600 camera [72]

In this study, time-averaged peak fluorescence was found to have a SNR in the range of 51-61, depending on laser variations. Instantaneous SNR values were much lower at approximately 4 for peak fluorescence. Due to the low SNR values instantaneously, it is more advantageous to use time-averaged profiles. Additionally, table 2 presents relevant information for the selected camera.

Table 2. Relevant Camera Specifications

	<b>Unit</b>	<b>Setpoint</b>	<b>pco.1600</b>
<b>Resolution</b>	Pixel		1600 x 1200
<b>Bits</b>			14
<b>Pixel size</b>	$\mu\text{m}^2$		7.4 x 7.4
<b>Full well capacity</b>	$e^-$		40,000
<b>Image sensor</b>			KAI-2001
<b>CCD temp</b>	$^{\circ}\text{C}$		$\Delta$ -50 vs. ambient temp
<b>A/D conversion factor</b>	$e^-/\text{count}$		2.1
<b>Readout noise</b>	$e^- \text{ rms}$	@ 10/40 MHz	10/21
<b>Maximum dynamic range</b>	dB		72
<b>Imaging frequency frame rate</b>	fps	@ full frame	30
<b>Non linearity</b>	%	Full temp range @10MHz	<2
<b>Dark current</b>	$e^-/\text{pixel*s}$	@20 $^{\circ}\text{C}$ @-20 $^{\circ}\text{C}$	0.5 0.01
<b>Exposure time</b>	s		5 $\mu\text{s}$ – 49days

### 3.2.3 Optical Material Considerations

While the bulk of the wind tunnel is constructed from standard polycarbonate, UV light is very strongly absorbed and results in virtually no transmission through polycarbonate. In order to allow the laser sheet to access the test section, a UV fused silica (UVFS) window is used which has a transmission of 91% for 266nm light. Additionally, the sheet forming lenses are also made from fused silica. In regards to the collected camera signal, figure 10b illustrates that fluorescent light exists in the visible spectrum, and testing showed that the fluorescence can be accurately imaged through the polycarbonate walls with the camera, without concern of significant attenuation of the fluorescent signal. Additionally, imaging through the polycarbonate walls served as a filter to remove any scattered 266nm light which the camera may record.

The problem of near-wall light scatter is a concern as the jet flow will exist in a region where the incident laser sheet impinges on the wall. Although dichroic mirrors were employed

trace amounts of 532nm light was still present in the laser pulse, and is responsible for significant surface scatter visible to the CCD. The test section wall was fixed in regards to the material used (aluminum), but different surface coatings and surfaces were tested to explore the scattering properties and optimization potential.

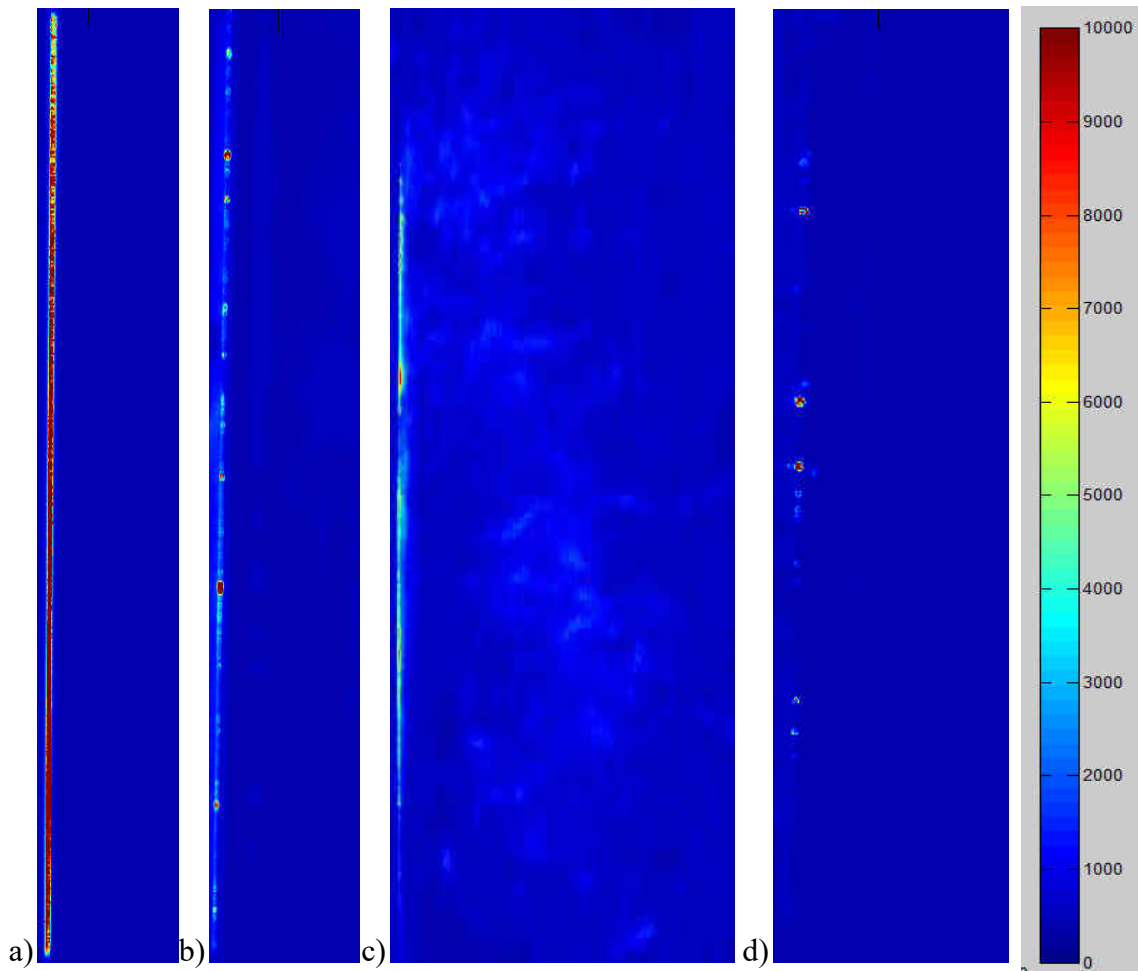


Figure 22. Wall scatter effects as seen by the camera for various surfaces. Luminosity demonstrated in arbitrary units

Figure 22 demonstrates the difference in potential interference seen from 63.5mm laser sheet impingement from the right on a) black paint on aluminum, b) uncoated polycarbonate, c) electrical tape, and d) uncoated UVFS. The same arbitrary fluorescence units are used in all cases to highlight the qualitative difference in material selection. On polycarbonate and UVFS surfaces

the wall scatter is greatly diminished, only demonstrating interference at localized “hot spots” thought to be imperfections in the surface. In PLIF studies targeting boundary layer measurements, UVFS has been shown to provide an optimal solution for minimizing wall scatter and reflection effects[29]. Additionally, laser polarization and angle of incidence are understood to play a role in wall reflections.

The use of electrical tape showed a diminished signal at the wall as compared to black paint over polycarbonate, but resulted in issues of smoke generation due to the high laser fluence. For black paint over aluminum (used in experimental configuration) a very high signal was recorded at the wall. However, the signal showed no interference even at small distances from the wall, indicating minimal interference with the PLIF signal. Ultimately, this configuration was used in subsequent experimental tests. Therefore due to feasibility constraints, a less than optimal optical configuration results in some unavoidable near wall light scatter noise.



## **CHAPTER 4. PLIF PROCESSING**

### **4.1 Correction Procedure**

According to the assumptions presented in section 2.1.1 the fluorescent signal collected becomes a linear function of the energy flux multiplied by the concentration of the acetone vapor. Therefore if the energy flux variations can be accounted for and one calibration data point can be obtained relating the fluorescence and concentration, the full field concentration map can be quantitatively generated. The correction process was conducted through MATLAB[73] scripts contained in appendix A, and adheres to the general outline as follows: 1) background subtraction to obtain  $S_f$ , 2) correction for absorption in laser propagation, 3) correction for laser sheet flux variations, 4) normalization and referencing.

#### *4.1.1 Sheet Characterization*

Due to the high sensitivity of the BBO crystals in the harmonic generation unit of the laser, with any minor temperature fluctuations the resultant beam will change profile dramatically. Although the crystals are housed in a constant temperature housing, the energy deposition in the crystals due to the beam itself will lead to temperature fluctuations in time. Therefore in order to obtain a non-temporally varying beam profile, the laser was allowed to run under full power and warm up to a steady state condition for a minimum of 30 minutes prior to each test. Testing was conducted making use of the calibration chamber, to determine the sheet temporal stability of the laser. After the warm-up period, the maximum change in energy distribution in a 5 minute time span was found to be less than 4%. Laser sheet characterization and testing took place in a 3 minute timespan, therefore the fluence correction is assumed to introduce an error of less than 2%, based on temporal variation. However, despite a stable beam

and optimization through tuning of the crystal orientation for maximum uniformity and power, significant changes in the energy flux across the laser sheet are unavoidable.

To counteract this issue, a methodology for characterizing the steady state energy distribution using equation (4) was developed. By designing an optically accessible volume which could be seeded with a uniform distribution of acetone vapor, a direct correlation between the fluorescent signal and the energy flux distribution exists. Figure 23a depicts the constant volume chamber used for calibrating the laser sheet.

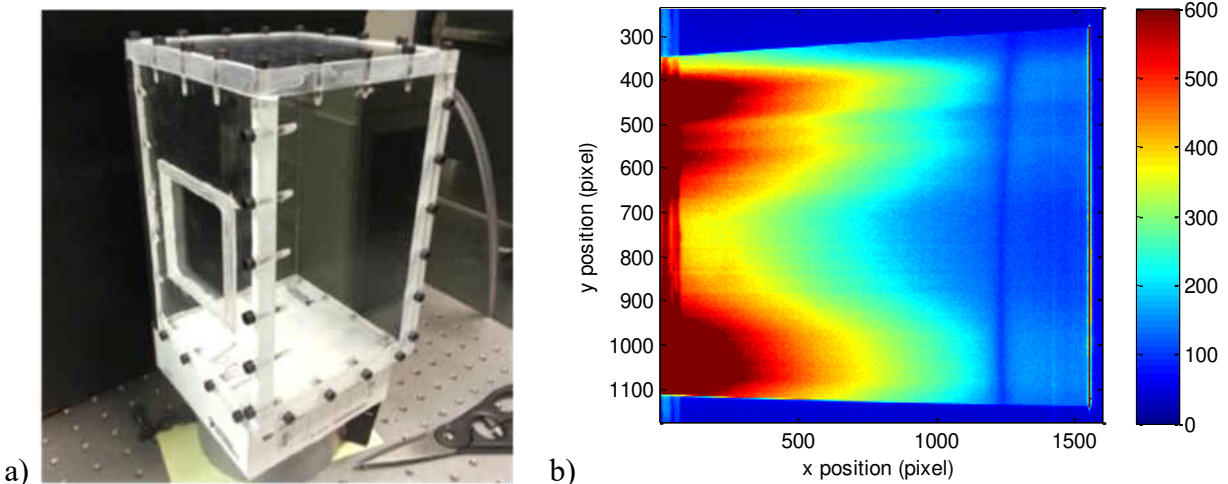


Figure 23. a) Calibration Chamber for characterizing laser sheet with 3in UVFS window for laser access  
b) Sample of fluorescence in a.u. as a two dimensional function.

Figure 23b demonstrates a sample of the fluorescent profile in the uniformly seeded calibration chamber. The image was captured orthogonally to the laser sheet with the sheet entering from the left. The decay profile due to absorption behaves as expected up to the focal plane of the lens ( $\sim x=1250$ ) which is marked by a sharp reduction in fluorescence. One may suspect that the excitation volume approaches zero at this location, which in accordance with equation (3) should lead to no fluorescent signal. However, as the volume asymptotes to a very

small value, the fluence should asymptote proportionally to a very large value. By making Gaussian assumptions, the focal waist size can be approximated by the following equation:

$$w = \frac{\lambda * f}{\pi * w_0} \quad (22)$$

where  $f$  indicates the lens focal length,  $w_0$  the initial beam size, and  $\lambda$  the laser wavelength. With these assumptions in place, the fluence is estimated at 1000 times larger than the linearity cutoff as reported by Lozano of  $1000\text{mJ}/\text{cm}^2$ . Therefore it is reasonable to believe that the energy flux asymptotes to such a high value that linear fluorescence can no longer be reasonably expected, and the volume trend dominates the fluorescence equation.

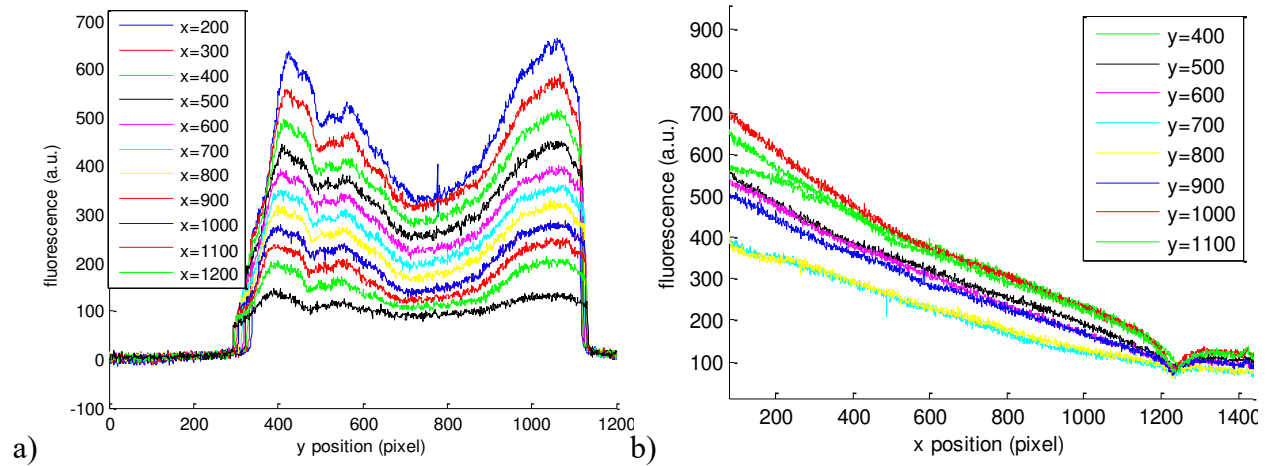


Figure 24. a) Fluorescence plotted vs. y for varying x values. b) Fluorescence plotted vs. x for varying y values

Figure 24a plots a sample of the sheet-transverse fluence for arbitrary propagation distances, indicating the large variations in laser energy. Figure 24b demonstrates the fluence decay with propagation distance for arbitrary y-locations, showing a relatively strong absorption

phenomenon. Aside from the focal plane, the fluorescence and therefore the energy flux decay in accordance with Beer's Law given in equation (23).

$$E(x) = E_o e^{-\alpha x} \quad (23)$$

When absorption effects are removed, the fluorescent signal becomes very uniform in the x direction, indicating the effective quantification of the absorption process. Similarly, the distribution of fluence can also be quantified. Therefore characterization of beam profile variations across the laser sheet and an estimate of the absorption properties allow for an accurate profiling of  $E(x,y)$ . Due to the portable nature of the test section, the calibration chamber was substituted into the same location as the test section to ensure that the exact same portion of the beam was being characterized. Quantification of the error in the calculated fluence distribution is difficult as the fluence is defined from the data itself. Nevertheless, by comparing the calculated energy distribution and the fluorescence distribution in the jet potential core, the sheet transverse fluence is estimated to be accurate to 3.1%.

Correction based on the absorption behavior of the laser potentially has a strong error associated with the correction methodology. Since the concentration distribution in the calibration chamber does not match that in the case of tested jets, the absorption profile demonstrated in figure 24b will not be applicable across the whole domain of a freejet or jet in crossflow. However, figure 24b demonstrates the maximum decay rate possible since the volume had a saturated acetone-air mixture. Second, the absorption correction only spans regions where the normalized jet concentration is above 0.25. Since the absorption and therefore fluence are exponentially dependent on the absorption coefficient, which is dependent on the acetone volumetric density, regions of low acetone concentration will have a negligible attenuation effect on the laser sheet. By taking the strongest absorption rate across the widest high-concentration

area, the maximum possible absorption based error in terms of normalized concentration is 7.5%. However, the actual expected error is significantly lower. Although greatly increasing complexity, an iterative solution correlating absorption and concentration effects would reduce absorption based concentration uncertainty further.

#### *4.1.2 Background and Referencing*

In using a CCD to record light in the visible spectrum, multiple sources of interference can also be recorded by the camera to yield a false fluorescent signal. One source of error is ambient light in the room, which although a darkroom was used, is unavoidable. Another source of errant light comes from the laser itself. Although dichroic mirrors were used, a small amount of 532nm light was still present yielding a slightly “dirty” beam. Since the CCD is not UV sensitive, and polycarbonate stands between the acetone jet and camera, the 266nm laser light does not corrupt the signal. Nevertheless, the 532nm light had the ability to scatter off of the wall and be recorded by the CCD. Finally, high laser flux impingement on the wall caused smoke in the near wall region. To counter these effects, proper background signal elimination must be achieved.

By running full test conditions but with no acetone-seeded jet introduction into the system, the luminosity of all non-acetone fluorescence light sources was combined into a background image. By far the largest light contaminant was scatter of 532nm light from the wall, which was measured by the camera to be approximately 10 times as luminous as the acetone fluorescence signal. Other ambient light sources and dark current merely provided a uniform offset, with very low standard deviation, approximately equal in intensity to the fluorescent signal. Due to the high wall scatter, background subtracting proves imperfect resulting in the possibility of signal contamination. However by applying a black non-reflective surface to the

wall, this scatter contamination was localized to approximately 1mm from the wall as demonstrated previously.

Normalization is also a concern as it is a requirement for obtaining quantitative concentration results. As previously mentioned, shot-to-shot laser power fluctuations exist, which are not monitored via detector. However since the peak jet fluid concentration, known to exist at the jet exit, remains constant in the system fluorescence values at this location can be used to reference individual pulse power fluctuations. Due to noise in the fluorescent signal, this methodology does allow for the introduction of an offset bias in the concentration in each normalized image. For time averaged profiles where the signal noise is smoothed out, this error is estimated to be less than 5%, which is consistent with known laser fluctuations. However in the case of an instantaneous image, the signal to noise ratio is significantly lower, and consequently a 10x10 pixel average must be taken at the jet exit to appropriately normalize instantaneous images.

#### *4.1.3 Time Averaging of Images*

Before exploring the effect of the correction procedure on a freejet, an examination of the time averaging methodology and implications for image accuracy is merited. As previously mentioned, and subsequently displayed in the following section, single pulse images are susceptible to significant amounts of noise in the system. Therefore time averaging across multiple images provides a solution to naturally filter out image noise. However, the discrete turbulence structures are washed out when a time averaged approach is used. Due to the turbulent nature of the jet leading to semi-discontinuous concentration profiles, a finite number of instantaneous images will be required to form a stable and accurate time averaged profile. In the case of a temporally fixed concentration distribution, noise removal can be visualized by

plotting the convergence of concentration values at arbitrary points with an increasing number of instantaneous images. Figure 25 demonstrated this by exploring the convergence of four points to their respective time averaged values.

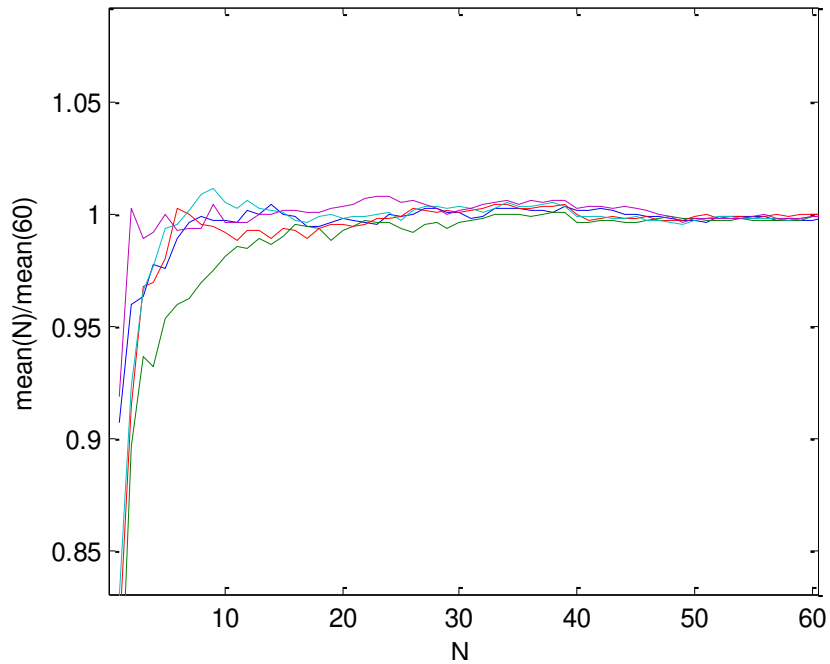


Figure 25. Convergence of fluorescent mean for arbitrary locations in uniform acetone field

By understanding the rate of convergence in a fixed concentration system, insight can be gained into the relative rate of convergence to a mean profile due to the turbulent structure of the jet as demonstrated in figure 26. Physically, the convergence of profiles is expected to be slightly slower in the case of the freejet, as both turbulent structures and inherent system noise must be smoothed out. This behavior can be seen in comparing the two graphs.

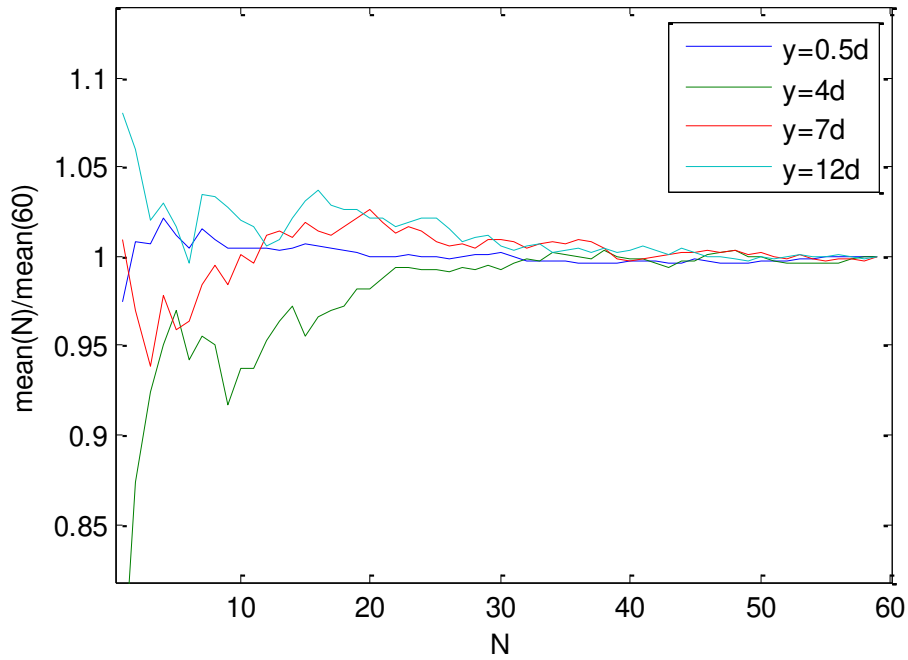


Figure 26. Convergence of mean for arbitrary distances above freejet exit

According to the above plot, the jet profile was found to converge to within 0.5% of the mean profile within 50 images. For the fixed concentration convergence test, a deviation of less than 0.2% existed after 50 images. However, to ensure an even more rigorous definition of the mean, a 75 image average was used in all time averaged profiles reported in this study.

Table 3. Uncertainty values for processing correction factors in a time-averaged study

Source	Uncertainty in Calculated $\eta$
<b>Image noise</b>	<3%
<b>Laser drift</b>	<2%
<b>Sheet transverse correction</b>	<3.1%
<b>Absorption correction</b>	<7.5%
<b>Image normalization</b>	<5%



## **4.2 Validation With Freejet**

In order to have confidence in the methodology to correctly convert from a fluorescent signal to an accurate quantitative concentration map of a seeded jet, a simple case of a freejet was first investigated. Freejets are highly intuitive and have been studied in many previous works. Turbulent jet theory has established that a round freejet will contain a time-averaged potential core region of uniform velocity and concentration extending approximately 4-6 diameters above the jet exit, and monotonically decreasing concentration with distance from the jet exit[74]. The same configuration as depicted in figure 19 was employed in the tests involving the freejet. However as opposed to the illustrated case, the wind tunnel was not used and instead a 3mm jet was used positioned on the tabletop. For the jet pipe, an L/D value of 20 was chosen to promote pipe flow development and reduce jet fluctuations due to air supply nonuniformities.

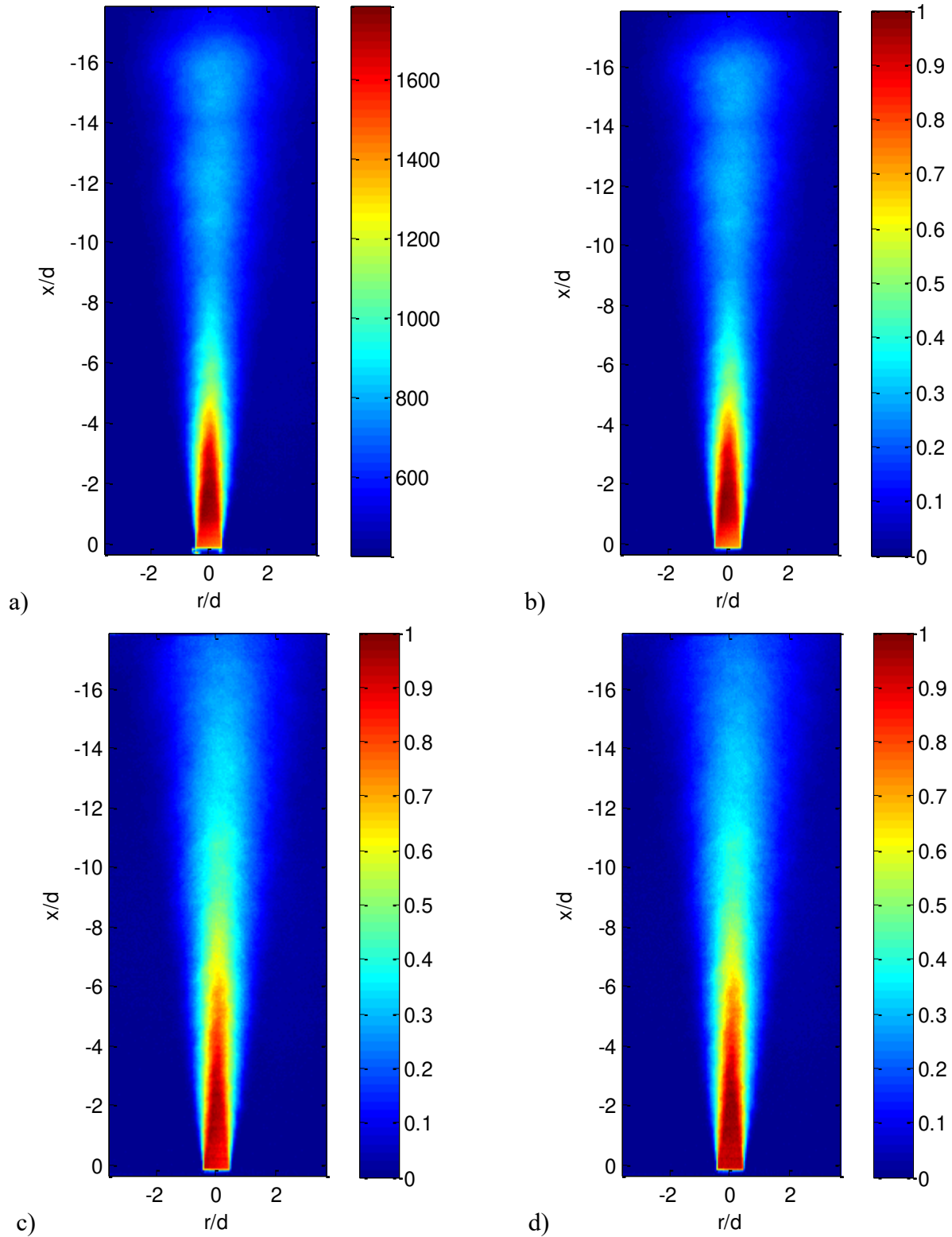


Figure 27. Demonstration of the correction effects for a turbulent freejet a) Raw fluorescence, b) background subtraction and normalization, c) energy flux corrections, d) absorption corrected

As a proof of concept, figure 27a-d demonstrate the correction process beginning in figure 27a and adding one correction feature at a time in 27b-d. It is apparent in figure 27a that there is a physically incorrect distribution of the concentration, especially when considering the region near the jet exit. At the exit, there should be only seeded jet fluid, and consequently the highest normalized concentration anywhere in the field. Incorrect distributions vertically are the result of laser sheet variations, while horizontal asymmetries result from absorption effects. The end result after correcting for these factors is shown in figure 27d demonstrates a normalized concentration map which is much more physically accurate than the fluorescence originally recorded in 27a. In these figures, the concentration is presented as the mole fraction of the jet fluid as it interacts with the surroundings.

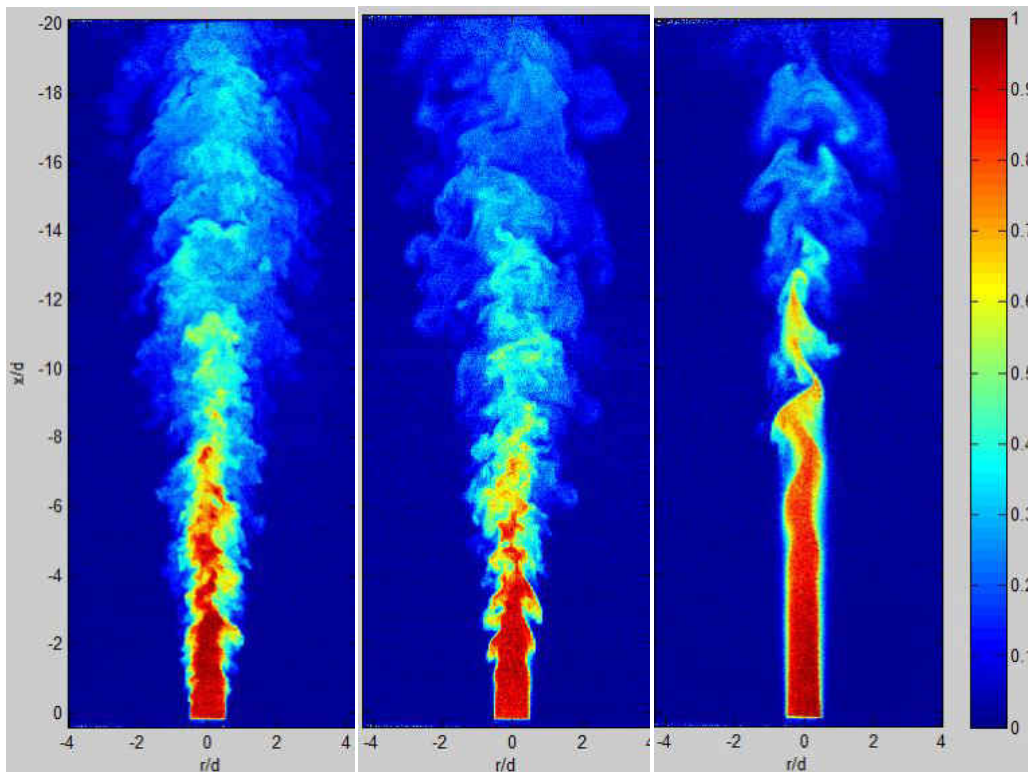


Figure 28. Instantaneous images of normalized concentration maps in a freejet for three Reynolds numbers. Left image shows a turbulent jet of  $Re=9006$ , middle image  $Re=3152$ , right image is a laminar jet of  $Re=900$

While figure 27d illustrates the time averaged profile of a jet with seemingly good accuracy, it is of interest to investigate the resolution ability of the system both spatially and temporally. Figure 28 displays the results of instantaneous PLIF images of a freejet as a function of different jet velocities. The first interesting characteristic of the jets above is the ability to freeze highly turbulent structures in a single image. Clearly the fluorescence lifetime of  $\sim 4$ ns of the acetone vapor, is much shorter than the turbulent timescales involved. The velocity values were chosen to demonstrate the transition from a laminar jet subject to shear layer instabilities to a highly turbulent jet with a nearly linear dispersion angle. For reference, the jets considered in the jet in crossflow portion of the report have jet Reynolds numbers of approximately 2,000-10,000.

Figure 29 portrays a result of the 10% mole fraction line plotted at two different Reynolds numbers for a time-averaged freejet. The higher Reynolds number jet displays a more linear dispersion, while the laminar jet requires more distance from the jet exit to succumb to shear layer instabilities. However, contrary to predictions by Labus, the net spread angle of the freejet extending 20 diameters downstream appears largely unaffected by the Reynolds number[44].

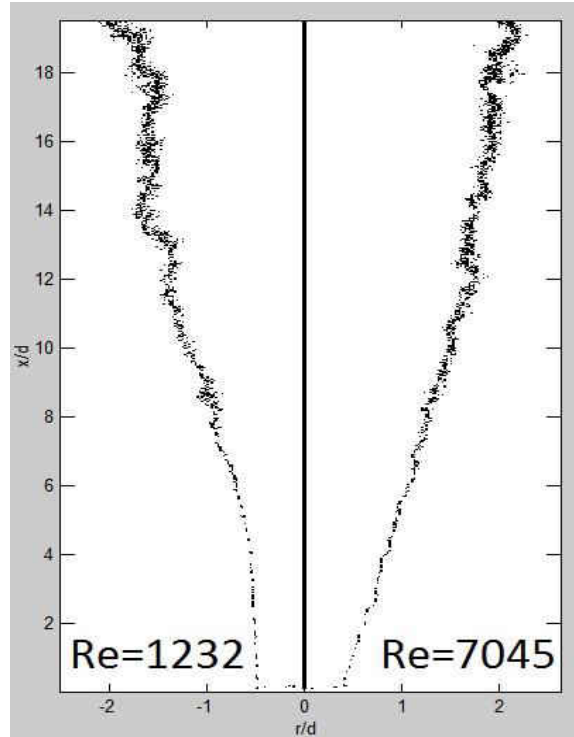


Figure 29. Plot of 10% concentration lines for two Reynolds numbers shown across symmetry planes

Another interesting realization of the instantaneous images is the relative increase in the amount of noise in the system, which is more apparent in the instantaneous cases. However, section 4.1.2 discusses the possibility for a concentration offset error and the measures for reducing this error for both time averaged and instantaneous profiles. The noise demonstrated in an instantaneous image is believed to result from dark current noise, which exists commonly in CCD devices. Since instantaneous structures have high concentration gradients, smoothing functions cannot be used to remove dark noise, without compromising the concentration data.

Finally in Figure 30, concentration maps of identical cases are compared between experimental values and modeled results. The jet presented has a diameter of 3 mm and a Reynolds number of 9000 for both the experimental and modeled cases. In a parallel manner to the case discussed in section 5.2, a 3 million cell mesh is used to perform an OpenFOAM simulation. Both the model and experimental configuration had  $L/D$  values of 20, promoting a

developed velocity profile. Assuming that the model predicted pattern represents the correct solution, it is obvious that the experimental LIF technique with accompanying correction processes yields an accurate methodology for further studies. The potential core is shown to extend to exactly  $x/d=4$  in both cases, and dispersion patterns demonstrate a nearly identical spread angle as well. Therefore through cross validation and physical expectations, the LIF technique has been shown to have satisfactory accuracy.

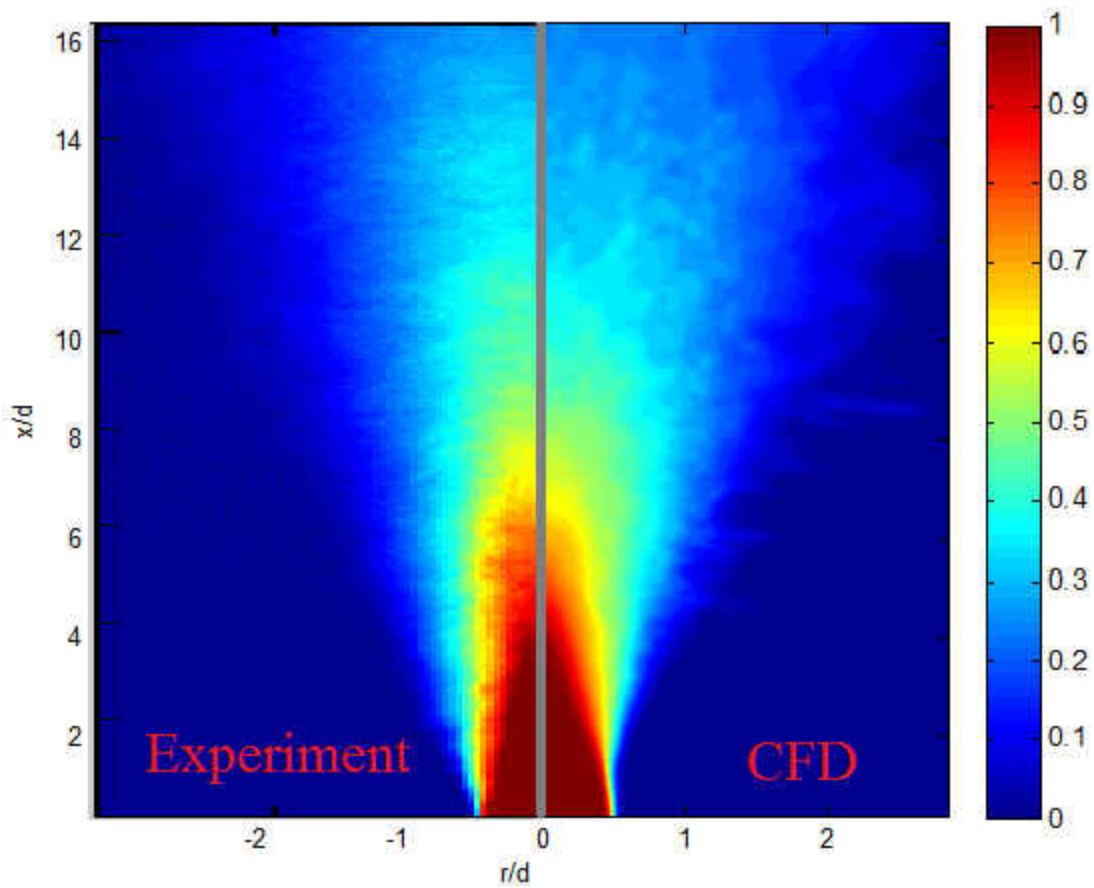


Figure 30. Compared concentration maps of an experimental and modeled freejet

## **CHAPTER 5. RESULTS AND DISCUSSION**

### **5.1 Jet in Crossflow**

As mentioned in the introduction jets in crossflow hold numerous possibilities in heat transfer and fluid dynamics related engineering applications. One area with a lack of experimental investigations is the mapping of concentrations of jets in crossflow, in the case of a near-wall and non-orthogonal jet. Again, it is worth highlighting that this regime closely resembles the configuration of many film-cooling applications. Orienting the laser sheet in the streamwise wall-normal plane provides insight into both the downstream propagation of the coolant, as well as information as to the thickness and structure of the film.

Nevertheless, there are merits to other configurations, including wall-parallel configurations and wall-normal streamwise transverse planar configurations. Cooling effectiveness is best measured through surface profiling, and can be measured via PLIF with a wall parallel sheet. However, this orientation yields a very restricted picture of the jet's structure and additionally suffers from difficulty in allowing for sufficiently near wall measurements. Therefore the streamwise wall-normal plane gives the most insightful data for this study.

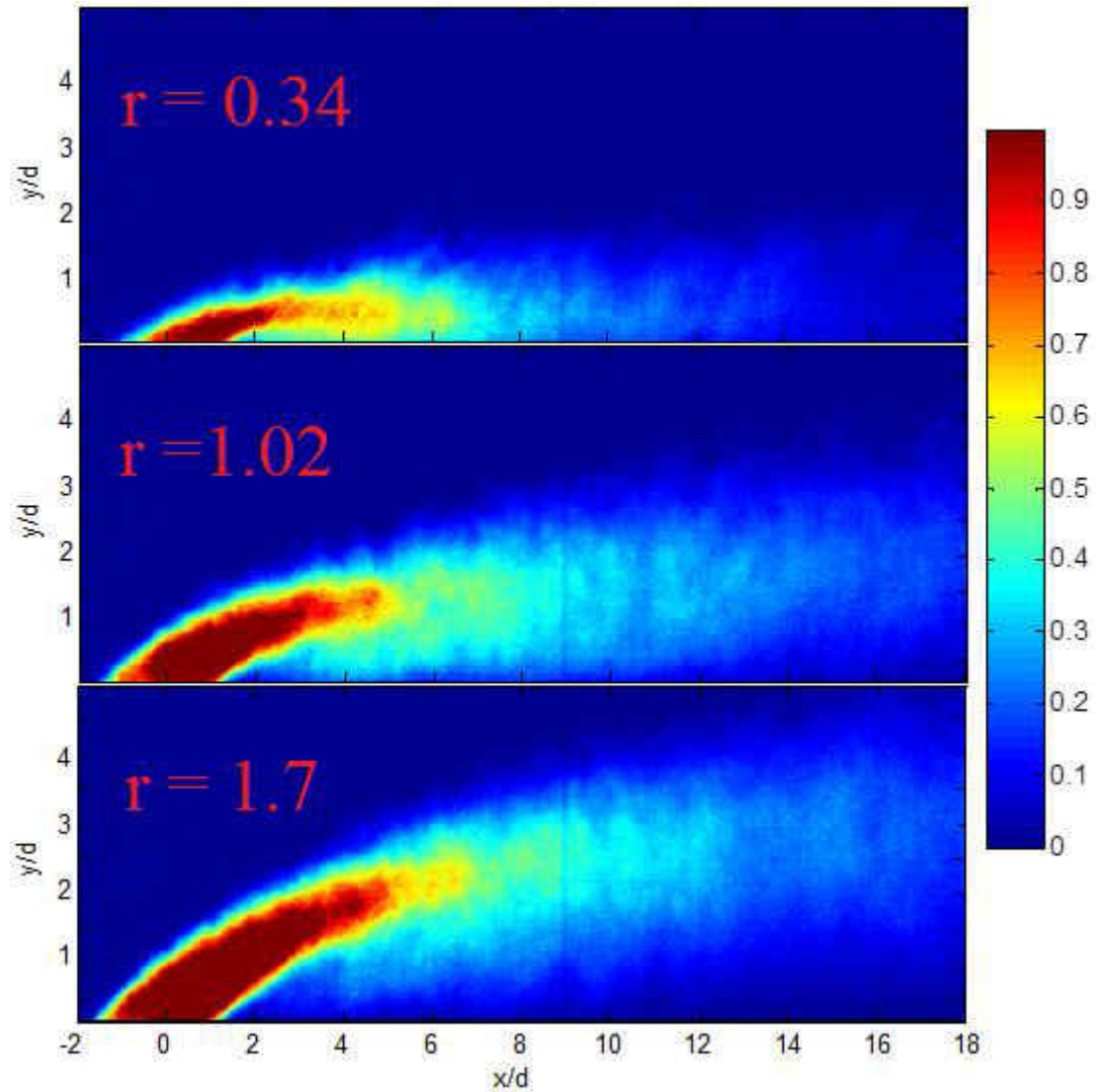


Figure 31. Normalized time-averaged concentration fields for 30° inclined jets in crossflow for three varying velocity ratios

Figures 31 and 32 display sample concentration distributions for both the instantaneous and time-averaged profiles of a select configuration. In these cases, a jet with a 30° inclination angle is considered at different velocity ratios. In the case of the time averaged  $r=0.34$  jet, the covering effect described by previous authors is clearly observable, as the upstream half of the jet exit appears to be issuing little fluid[64].



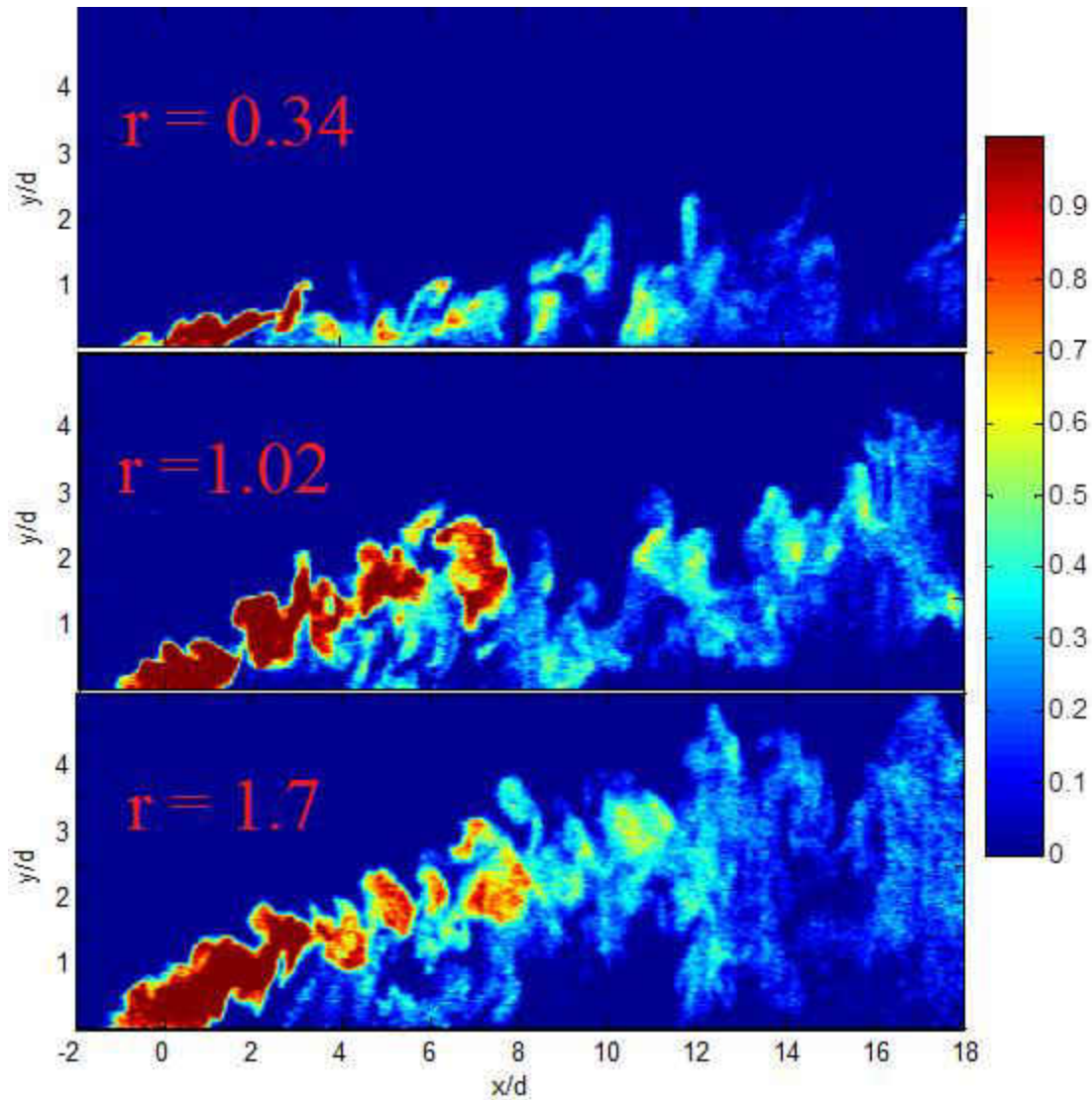


Figure 32. Normalized instantaneous concentration fields for 30° inclined jets in crossflow for three varying velocity ratios

The sample results above provide reasonable insight into the results gained from using PLIF on a seeded jet in crossflow. Intuitively, as the velocity ratio is increased, the increased y-momentum of the jet encourages further separation from the wall. Additionally, due to the highly turbulent structure of the jet, the time averaged profiles are diffuse in nature. As turbulence leads to a more uniformly diffuse structure as opposed to the kidney structure reported by other authors, planar concentration distributions are deemed minimally sensitive to

sheet position perturbations. A counter example to this case is seen in a preliminary modeling attempt in section 5.2.

The instantaneous images are useful in establishing the characteristics of the jet turbulence as it enters the crossflow. It is apparent that the jet has highly turbulent large scale eddies immediately issuing from the jet exit. These large eddies lead to a very discontinuous profile in the jet with many semi-discrete lumps propagating downstream. For the three time averaged profiles above, slices of concentration at discrete x-locations aid in illuminating the physical results of the trajectory and mixing of the jets. Figures 33a and 33b depict the normalized concentration profiles at 2d and 10d downstream respectively.

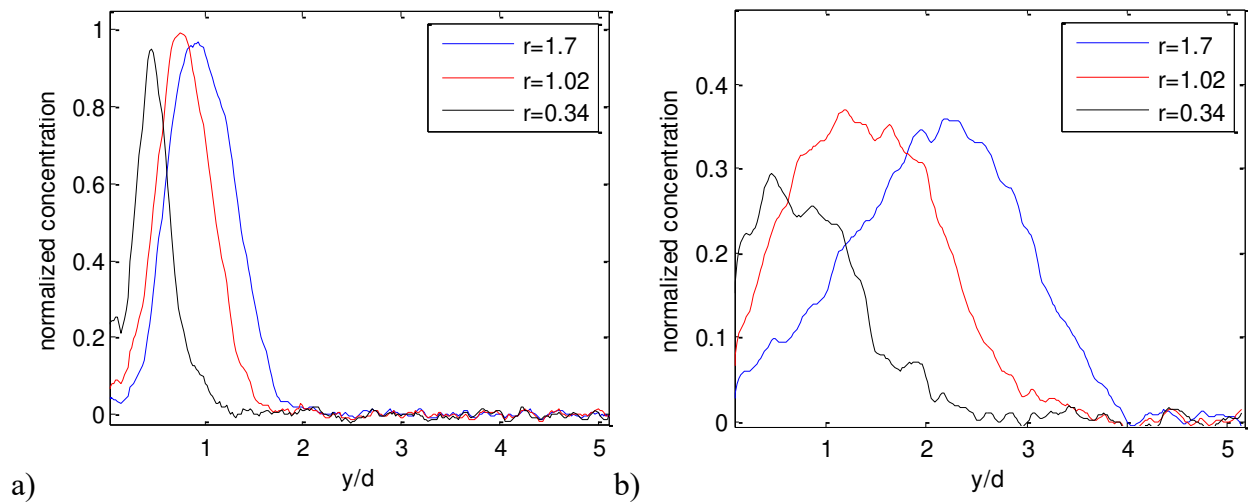


Figure 33. a) Normalized concentration as a function of  $y/d$  at a)  $x=2d$  and b)  $x=10d$  downstream of the jet exit

At near field locations, an increase in velocity ratio plays little role other than simply shifting the concentration profile away from the wall and slightly broadening the profile. At a location 10d downstream however, a noticeable difference in profile width and near wall concentration emerges. Since the cooling efficiency and coolant concentration are intimately coupled, the necessity of having a wall-attached jet in film cooling configurations is apparent. In

regards to dissipation, the peak concentration is reduced by more than 60% at this location for all velocity ratios. Similar trends were noticed for cases of 90°, 50°, and 40° inclination angles.

### 5.1.1 Fixed Angle Scaling

By holding all other conditions constant, parametric variations allow for characterization of the jet's trajectory in terms of a functional dependence on that parameter. One of the most intuitive dependences of the jet trajectory is the relationship between the flow ratio of the jet and the freestream. As reported by many other authors[53], the trajectory of an orthogonal jet seems to have a functional dependence on the velocity ratio of the form  $y = f(x)r^{0.78}$ . Although this dependence has been shown many times for a 90° jet, authors have shown no such dependences for non-orthogonal low-r value jets in crossflow. This does not stem from conflicting reports, but rather a lack of data on this specific regime of jets in crossflow. In order to isolate the velocity ratio dependence of the jet, scaling of the trajectory by different parameters gives a visual interpretation of the degree of dependence on that scaling parameter.

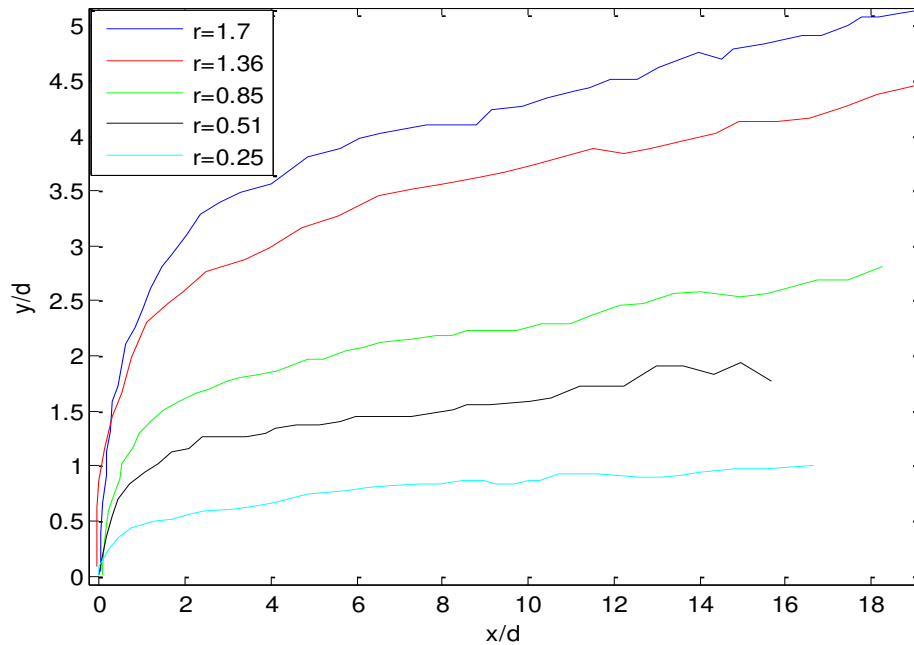


Figure 34. Trajectories for different velocity ratio conditions of an orthogonal jet

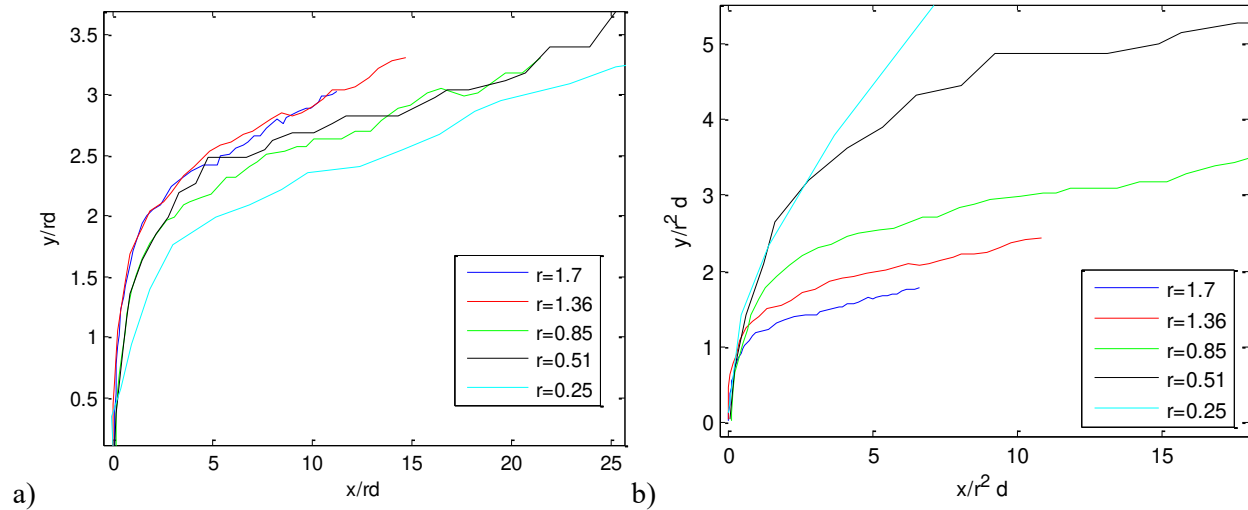


Figure 35. Trajectories for different velocity ratio conditions of an orthogonal jet scaled by a)  $rd$ , b)  $r^2 d$

To first compare results with the dependencies seen by other authors, the case of a  $90^\circ$  jet for varying velocity ratios are considered. Figure 34 first demonstrates the trajectories, scaled by jet exit diameter, for five selected velocity ratios. The trajectories themselves are defined by the maximum concentration location as a function of downstream location planes. The local maximum velocity could also be used to define the jet trajectory, and is reported to indicate 5-10% deeper penetration than using peak concentration definitions[55]. Unscaled results are intuitive in that higher velocity ratios yield greater penetration into the flow.

Not presented is a case of  $r=0.17$  where the jet remains highly attached to the wall and demonstrates no downstream separation from the wall. In this case, a slight oscillatory behavior of the maximum concentration line along the wall appears to be an interaction as the two streams adjust to an equilibrium in terms of velocity direction. In the unrepresented case where the jet remains completely attached to the wall, a slight shift of the peak concentration seems to occur as it shifts towards the wall. Due to the higher velocity with increasing distance from the wall, it is expected that dissipation and mixing happens at a higher rate away from the wall, resulting in a concentration shift towards the wall.

Figure 35a demonstrates the selected trajectories when they are scaled by velocity ratio and jet diameter. Similar to the data of Smith, collapsing is demonstrated but is incomplete. Since there is no modulation of the density ratio, it is impossible to tell if the trajectory is only a function of  $r$  or is a function of the density ratio as well. Additionally, the functional dependence on jet diameter is unquantifiable. However, we can conclude that for this case the trajectory's relationship with the velocity ratio is not completely scalable with the velocity ratio. Another parameter which could be proposed to play a large role on the trajectory of the jet based on physical intuition is the momentum flux ratio. Figure 35b demonstrates the same three trajectories when scaled by the velocity ratio squared. Since the trajectories do not demonstrate the collapsing seen with scaling by  $r$ , it is apparent that for these cases that the trajectory is not simply a function of the momentum flux ratio ( $J$ ). This is somewhat of a trivial conclusion as figure 35a implies only a slight nonlinear relationship, but addresses a seemingly reasonable guess of momentum holding sole responsibility for the trajectory.

In order to best quantify the scaling dependence of the  $90^\circ$  jets studied, different scaling relationships were further explored. As demonstrated in figure 36, the most complete collapsing was found with scaling by  $r^{1.2}d$ . In a parallel manner to equation (10), the trajectory as a function of velocity ratio can be expressed as follows.

$$\left(\frac{y}{r^{1.2}d}\right) = 1.4 * \left(\frac{x}{r^{1.2}d}\right)^{0.3} \quad (24)$$

These values line up extremely well with the previously reported values, even with the slightly different scaling parameter.

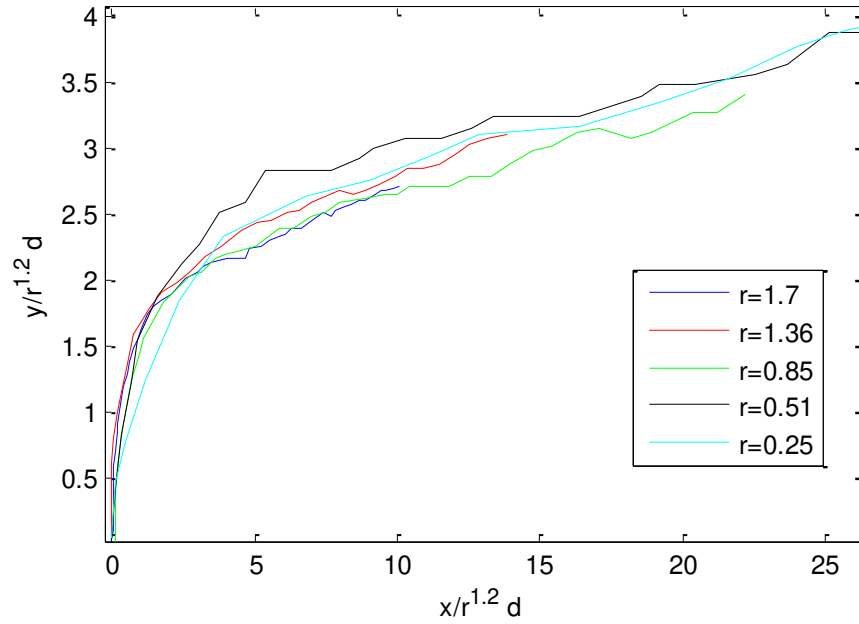


Figure 36. Varying velocity ratio conditions of an orthogonal jet scaled by  $r^{1.2}d$

This scaling relationship leads to the conclusion that the jets trajectory is neither a function of the mass flux ratio or the momentum flux ratio, but appears to be a combination of the two in an identical manner to the results of Smith and Mungal.

Since lower inclination angles are common in film cooling configurations, parallel studies for a  $30^\circ$  and also  $40^\circ$  and  $50^\circ$  jets were also considered. Figures 37a and 37b demonstrate trajectory results for the  $30^\circ$  configuration with unscaled and scaled results presented respectively. As previously seen, the trajectory indicates higher degrees of separation from the wall with an increase in the velocity ratio in figure 37a. Note that for the case of  $r=1.7$ , the penetration height is significantly less than for the  $90^\circ$  jet. Again, the jets can be scaled to gain information about the functional dependence on the velocity ratio. With scaling by the mass flux ratio (and therefore  $r$ ), a reasonable collapsing of the trajectories is demonstrated. The strongest outlying trajectory is the case of  $r=0.34$ , which appears to be more strongly impacted by the wall. The other four velocity ratio conditions which appear to have fully separated from the wall,

demonstrate a very strong collapsing of the trajectories. Although there is significant variation in the x-component of the jet's velocity as the velocity ratio is varied, scaling indicates a linear influence of this effect. In this case, scaling by the momentum flux ratio is not presented as it would simply lead to further decoupling of the trajectories.

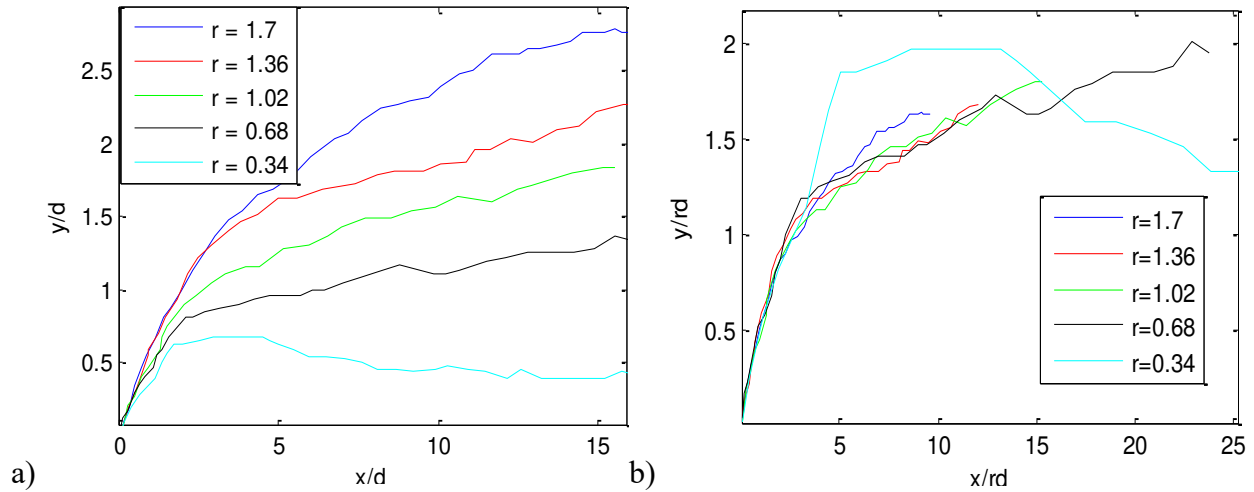


Figure 37. Trajectories for different velocity ratio conditions of a 30° jet. a) unscaled, b) scaled by  $rd$

Tests with a 50° and 40° inclination angle jet demonstrates similar scaling relationships, but are omitted as the 30° jet best approximates a real-world configuration. However in the case of the 30°, 40°, and 50° jets, contrary to the orthogonal jet, the trajectories seem to best scale directly with  $rd$  and not  $r^{1.2}d$ . A possible explanation of this originates from the boundary layer profile. In these near wall jets, the trajectory lies within the boundary layer. Therefore, lower inclination angle jets may be relatively less impacted by the crossflow than they would be in the case jets near the boundary layer edge. The presence of a relatively thick boundary layer is interesting as film cooling relies on keeping the coolant very near the wall, often times inside the boundary layer.

### 5.1.2 Fixed Velocity Ratio Scaling

In a similar manner to the previous section, testing can be carried out for parametric variation of the jet inclination angle. A lack of literature specifically investigating the effect of inclination angle on trajectories of jets in crossflows was noticed by the author. Intuitively, larger inclination angles will result in a relatively larger wall-normal momentum of the jet, promoting separation from the wall. While penetration maximization is often desired for fuel delivery systems, minimization is desired for film cooling. However there are notable drawbacks to low angles of inclination, primarily that the exit hole geometry leads to significantly larger surface distortion as well as difficulties in logistically implementing a sufficient number of jets in a compact manner. While the exact orientation and shape of film cooling holes is considered proprietary information by most companies, an inclination angle of  $20^\circ$ - $30^\circ$  is largely viewed to meet the criteria of minimal wall-normal momentum, while simultaneously being geometrically feasible and practical for desired configurations. Due to experimental limitations, the shallowest inclination angle studied in this work was  $30^\circ$ . Figure 38 shows a selected case of  $r=1.36$  for varying jet inclination angles, while figure 39 demonstrated similar relationships for a lower velocity ratio.

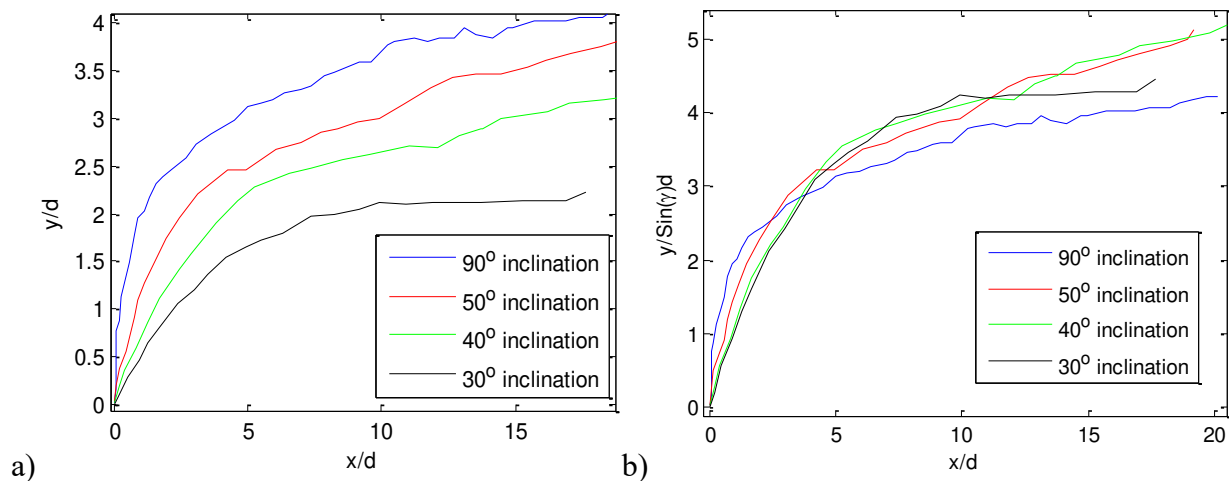


Figure 38. a) Unscaled and b) Scaled trajectories for varying jet angles for a fixed velocity ratio of  $r=1.36$



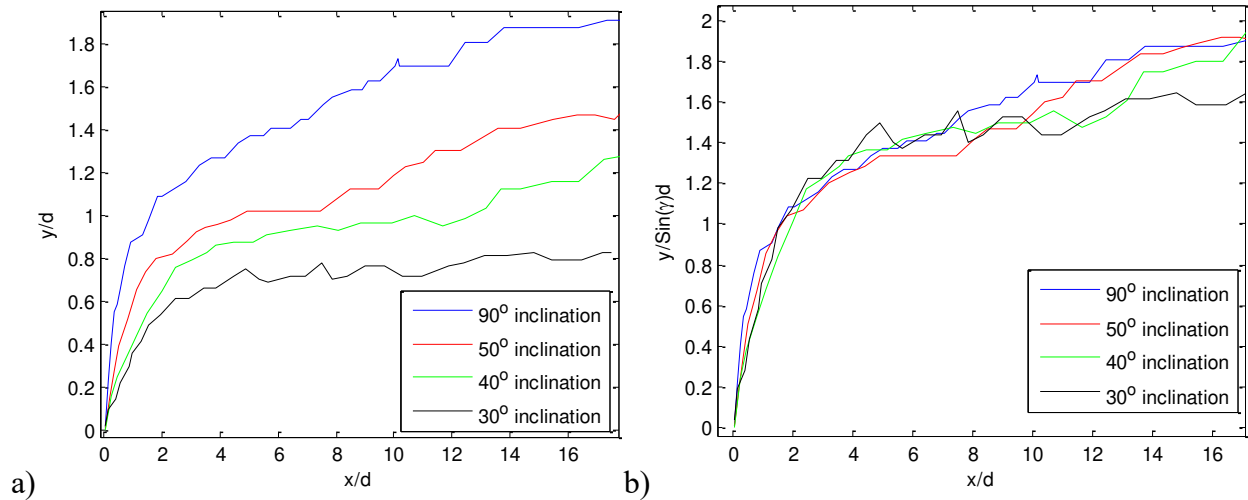


Figure 39. a) Unscaled and b) Scaled trajectories for varying jet angles for a fixed velocity ratio of  $r=0.51$

While there are many different possible functional dependencies of the trajectory in terms of the inclination angle, a linear relationship with the wall-normal velocity component best collapses the trajectories. Although the initial x-velocity of the jet is varying significantly this seems to play very little role in the trajectory the jet takes.

In a study of  $r=0.25$ , jets all demonstrated unpredictable trajectories as they either fully or only partially detached from the wall as shown in the case of the  $30^\circ$  jet. Therefore in these wall-attached cases, trajectory collapsing by scaling with orthogonal velocity is no longer valid.

### 5.1.3 Density Ratio Variations

Density ratio variation was not achievable through this configuration, but must be considered to fully understand the factors responsible for near wall jets in crossflow. In a real-world application of film cooling the coolant jet is often significantly lower in temperature than the freestream, and therefore a non-unity coolant to freestream density ratio exists. For typical gas turbines this value is approximately 2.0 [59]. As a result of the seeded acetone mixture playing the role of a coolant jet, a density ratio of approximately 1.25 exists in the studies presented in chapter 5. For a fixed blowing ratio, there is no alteration in coolant mass flux ratio

implying no change in total jet fluid concentration integrated across a downstream plane. However, an increase in the density ratio for a fixed  $M$  value, leads to a reduction in the momentum flux ratio ( $J$ ), likely reducing the degree of wall separation of the potentially film cooling jet. Therefore, with no extra cost of increasing flow ratios, a potentially higher coolant concentration exists along the injection wall with increasing coolant to freestream density ratios.

In section 5.1.1, the dependence of the trajectory as a nearly linear function of  $r$  was determined. However, a study investigating the effects played by the density ratio would aid in further clarifying this relationship. For the scaling presented, it is not possible to determine if the trajectory is a function of the velocity ratio only, or potentially the mass flux ratio. Intuitively, one would expect that the density plays a significant role in the trajectory.

## **5.2 CFD Comparisons**

Although confidence was instilled in the methodology through the understanding of a freejet structure, cross-comparisons with Computational Fluid Dynamics (CFD), using OpenFOAM[75], was also achieved. The multiphase, incompressible flow solver, interFoam, is used to track the interfaces between the two phases. This method solves partial differential equations for the scalar transport of each concentration based on the velocity and pressure field. Interested readers are forwarded to the article by Kissling[76] for a detailed description of the interFoam solver. Although highly complex models could be adapted in an effort to identically match the experimental results, the author retained a more simplistic and general case to explore if scaling relationships and trajectory data are reasonable in a less restrictive configuration. To compare experimental and simulation results, figure 40 depicts the two full-field concentration results in the case of a  $30^\circ$ , 3mm diameter jet with a velocity ratio of  $r=1.7$ .

The sudden expansion of the jet into the test section creates a highly turbulent jet that is difficult to accurately resolve. The jet's approximate Reynolds number of 9,000 requires accurate

modeling of the turbulent fluctuations present downstream of the opening and locally in the jet recirculation region which stabilizes and directs the jet downstream. To accurately resolve these turbulent features a Large Eddy Simulation (LES) is used to model the turbulent fluctuations  $(\overline{u_i' u_j'})$ . LES fully resolves the large “energy carrying” turbulent fluctuations  $(\overline{u_i' u_j'})$  and solely models the small or sub-grid scale  $(\overline{u_i' u_j'})_{sgs}$  turbulent fluctuations. To provide closure for the SGS velocity fluctuations a single equation eddy viscosity model is used, which assumes that at the interface of the resolved and SGS scales there exists a local equilibrium. A transport equation is used to solve for the SGS turbulent kinetic energy ( $k_{sgs}$ ) which is then dissipated by a modeled SGS viscosity ( $\mu_{sgs}$ ). Turbulent quantities are defined with respect to the mesh size and boundary conditions which are now discussed.

The computational domain is discretized into approximately 2 million cells which are composed of 98% hexahedral (HEX) cells with the remaining cells made up of prisms and polyhedrals. The non-HEX cells are introduced at the interface between HEX refinement regions and are located far into the free stream flow to prevent the effects of any non-orthogonality between refinement regions. With the use of this refinement a  $Y^+$  value of approximately 100 is obtained along the lower wall and consequently wall functions are used to model the SGS turbulent kinetic energy ( $k_{sgs}$ ) and the sub-grid viscosity ( $\mu_{sgs}$ ). The wall function model constants are defined appropriate to the expected turbulent length scales and mesh cell size. The cube root volume of the cell size is used to filter between the resolved and modeled turbulent scales, accordingly mesh refinement is present in regions of high strain (near the jet exit) to ensure the smallest stresses are always modeled and not resolved.

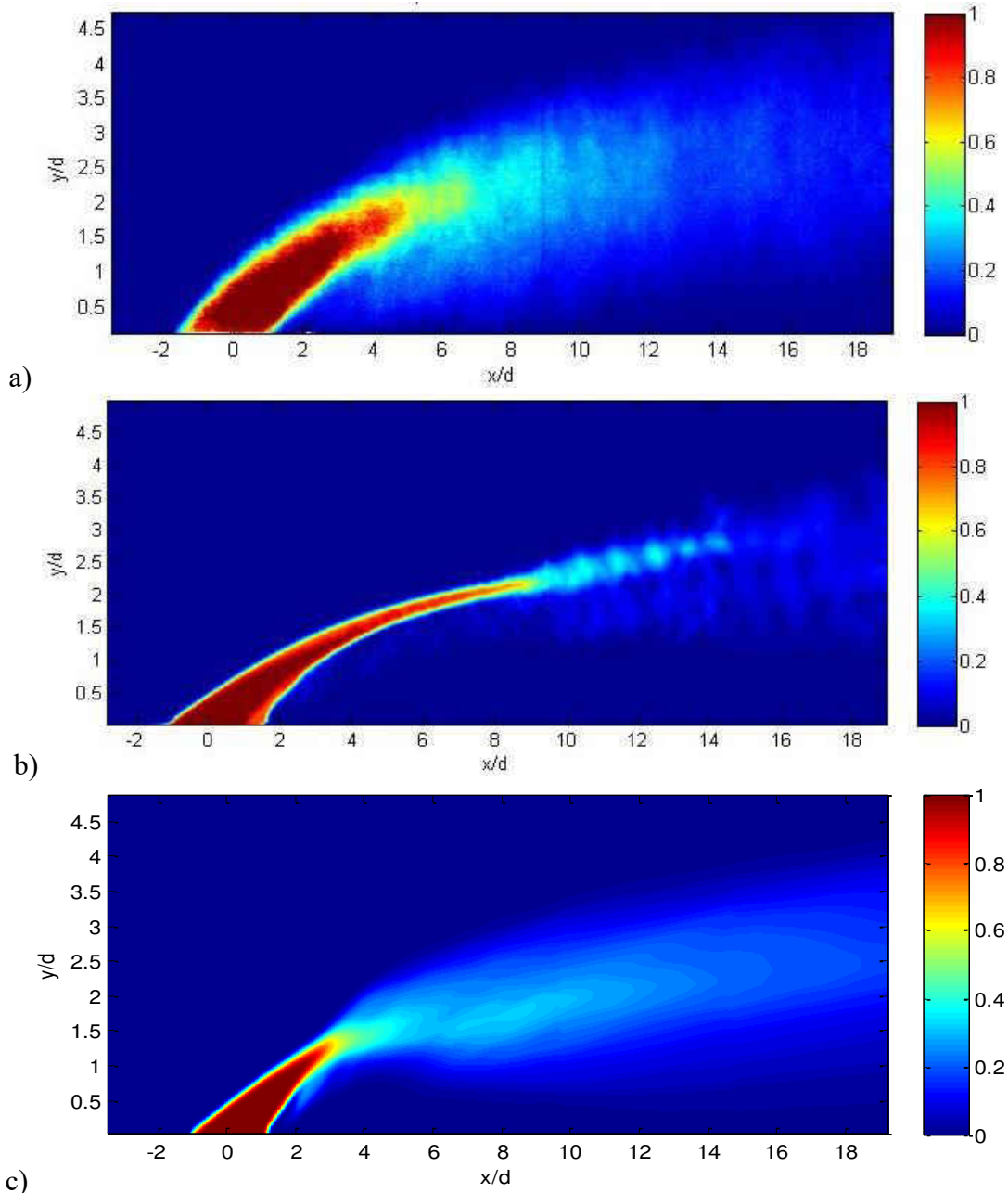


Figure 40. Concentration maps of a 30° jet with  $r=1.7$ . a) Experimental, b) low turbulence CFD, and c) higher turbulence CFD normalized concentration maps for time-averaged JIC

The velocity inlet and outlet conditions are made similar to those of the experiment with no slip conditions present along walls. For the outlet patch all quantities are imposed a zero gradient condition, since the outlet is located far downstream of the jet and is void of any large velocity or pressure gradients.

Preliminary attempts at modeling yielded interesting results. A  $30^\circ$  inclined jet with an  $r=1.7$  value was compared between experiment and simulation and time averaged results are shown in figure 40. With regards to figures 40a and 40b, the trajectories of the experimental and simulated jets are in good agreement when comparing the center of mass of the jet. However the experimental case demonstrates a much more diffused structure; this along with instantaneous profiles indicate that large scale turbulence is strongly underpredicted in this first CFD simulation. A consequence of turbulence underprediction is believed to result in the relative impact that the counter rotating vortex pair (CVP) plays in the jet structure.

As evidence of this self affecting structural behavior, figure 41 shows the CFD jet profile for a contour of  $C=0.5$  corresponding to the 3d jet used for figure 40b. This depiction of the jet structure implies that for a centerline slice, the jet becomes thin in the y-direction when the CVP has a strong existence. Additionally, it is apparent that the CVP strongly persists into the far-field, well beyond 10 jet diameters downstream of the jet exit.

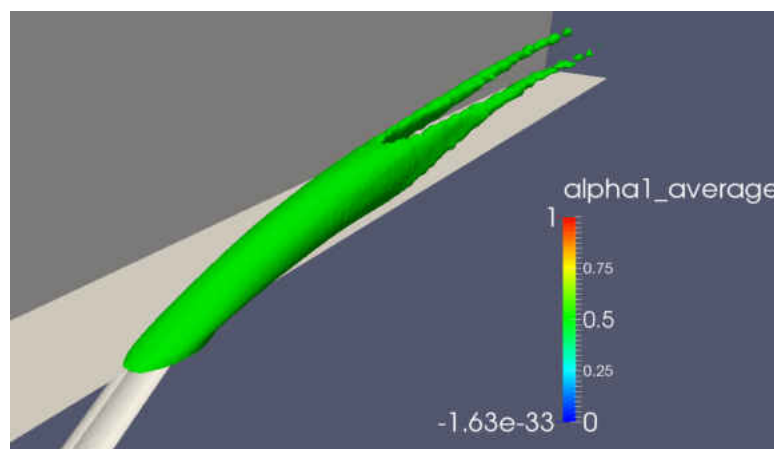


Figure 41. CFD generated contour map of a  $30^\circ$  jet with  $r=1.7$ , for  $C=0.5$

With an improved understanding of the role of turbulence in the jet structure, a turbulent velocity inlet to both the freestream and jet was imposed, along with an increased turbulent kinetic energy, estimated from the following equation:

$$k = \frac{3}{2} (U * 0.16 Re^{-1/8})^2 \quad (25)$$

where  $k$  signifies the turbulent kinetic energy, and  $U$  denotes the mean velocity. These additions result in a more diffuse structure and diminished centerline thinning due to the CVP at downstream locations, as evidenced in the centerline plot in figure 41c. This self affecting behavior aligns with results from Takeishi, who found that for a similar case in which the jet has a significant swirl component, the CVP virtually disappeared and consequently altered the downstream jet structure[65]. Additionally, this lead to an increase in film cooling effectiveness due to a more diffuse structure, as round jets are highly susceptible to separation. Therefore, the turbulence and consequently CVP structure of the jet can play a significant role in proposed applications of film cooling and merited further modeling refinement[77].

The CVP itself is an interesting phenomenon which can be fundamentally characterized by looking at simulated concentration maps at discrete downstream planes. As evidenced in figure 42, the initial jet rapidly develops a strong CVP within a few diameters of the jet exit. Contrary to the lower turbulence case, the CVP is destroyed by turbulent mechanisms within 10 diameters from the jet exit. Far field time averaged concentration profiles assume a Gaussian distribution, assuming substantial separation from the wall as occurred.

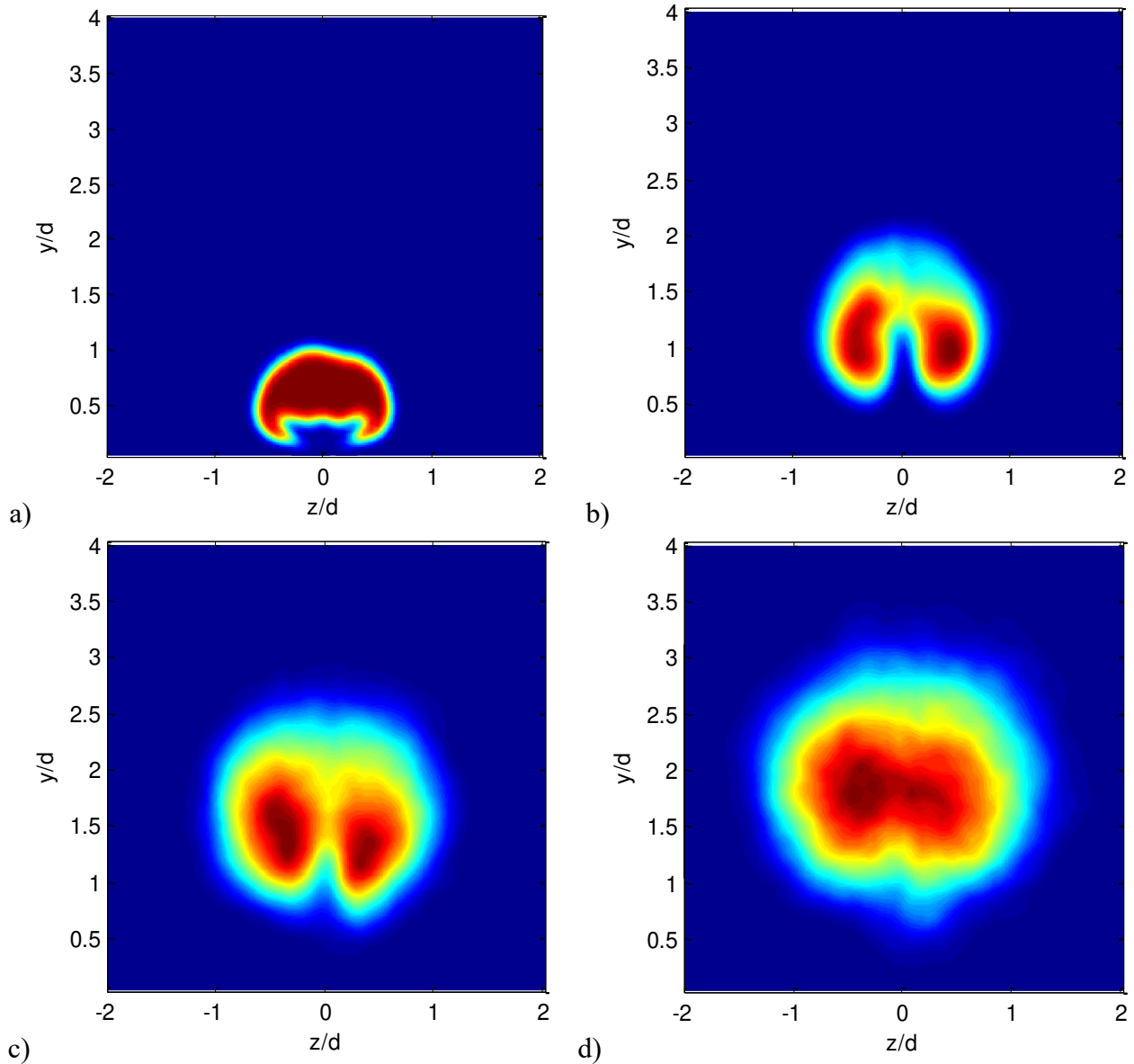


Figure 42. CVP development downstream of  $30^\circ$   $r=1.7$  jet at downstream planes of a)  $x=1.58d$ , b)  $x=3.91d$ , c)  $x=6.38d$ , and d)  $x=8.97d$

In figure 43 trajectories are compared for a  $30^\circ$  jet at various velocity ratios for experimental and OpenFOAM results accordingly. The CDF model under predicts separation by approximately 10% as compared to the experimental observed values. This is expected as the freestream boundary layer is roughly 70% thinner in the CFD case, leading to a higher local velocity ratio. Aside from this slight skew, the data is in good agreement between the two cases.

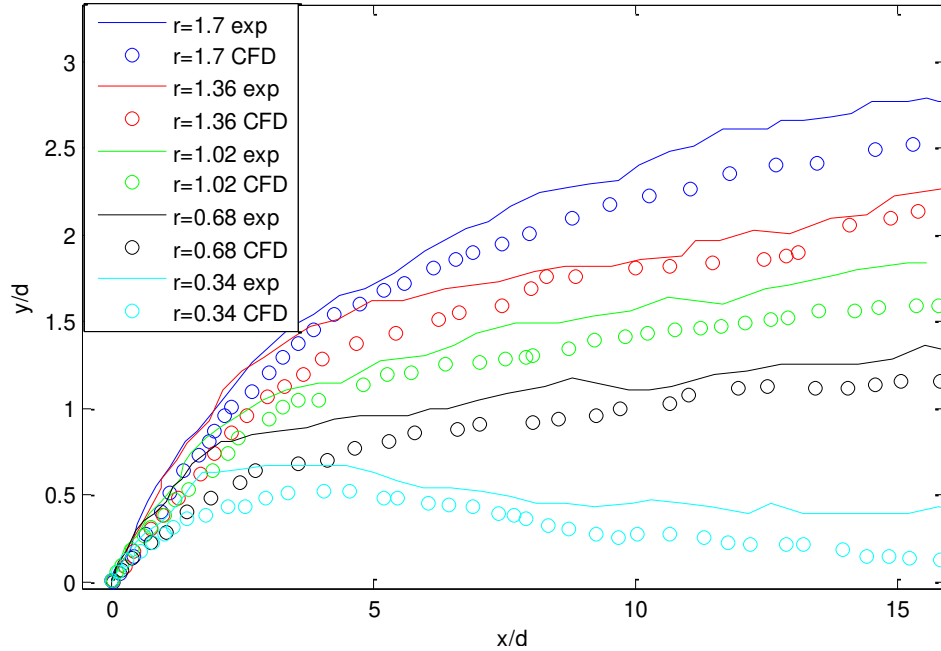


Figure 43. Comparison of experimental and CFD reported trajectories

Figure 44 depicts a plot of the velocity magnitude distribution for the same configuration, unattainable through the current LIF configuration. It is apparent that the modeled boundary layer may not have the same thickness when compared to the experimental case. Elevated jet velocities persist downstream of the jet exit significantly into the far field region, with 25% higher velocities demonstrated in the jet 25 diameters downstream.

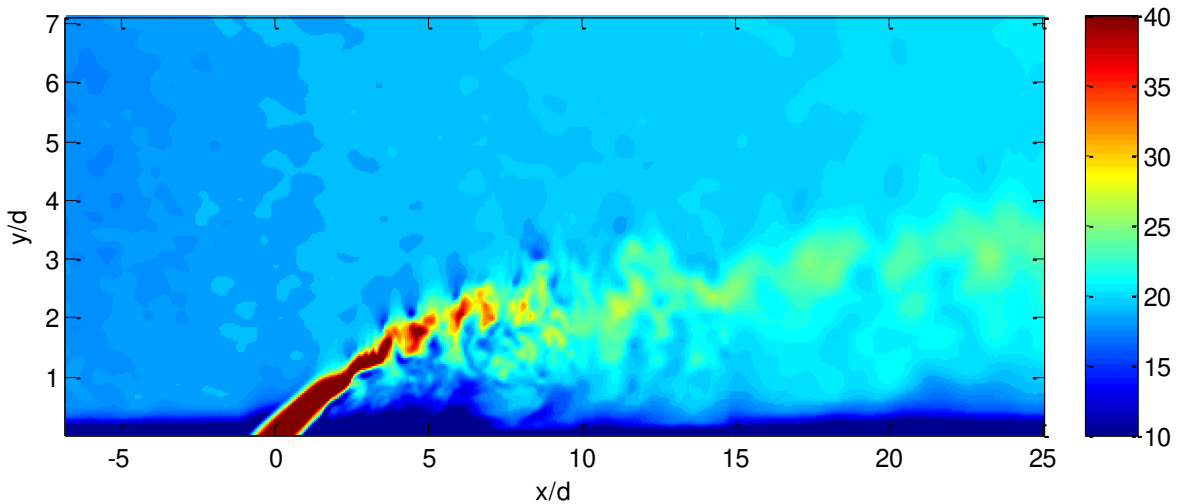


Figure 44. Velocity profile for instantaneous CFD result of 30°  $r=1.7$  jet, with colorbar showing velocity magnitude in m/s



Additionally, OpenFOAM trajectories can be scaled by  $rd$  to investigate the trajectory dependence on the velocity ratio. Results from this comparison are displayed in figure 45. It is shown that in a very similar manner to the experimental cases, despite minor quantitative variations from the experimental trajectories, the modeled  $30^\circ$  jet demonstrates a strong functional dependence on the velocity ratio. Therefore both experiments and modeled results indicate the same trend of  $rd$  scaling of a  $30^\circ$  inclined jet, even though the modeled case contains some known intentional boundary condition deviations from the experiment.

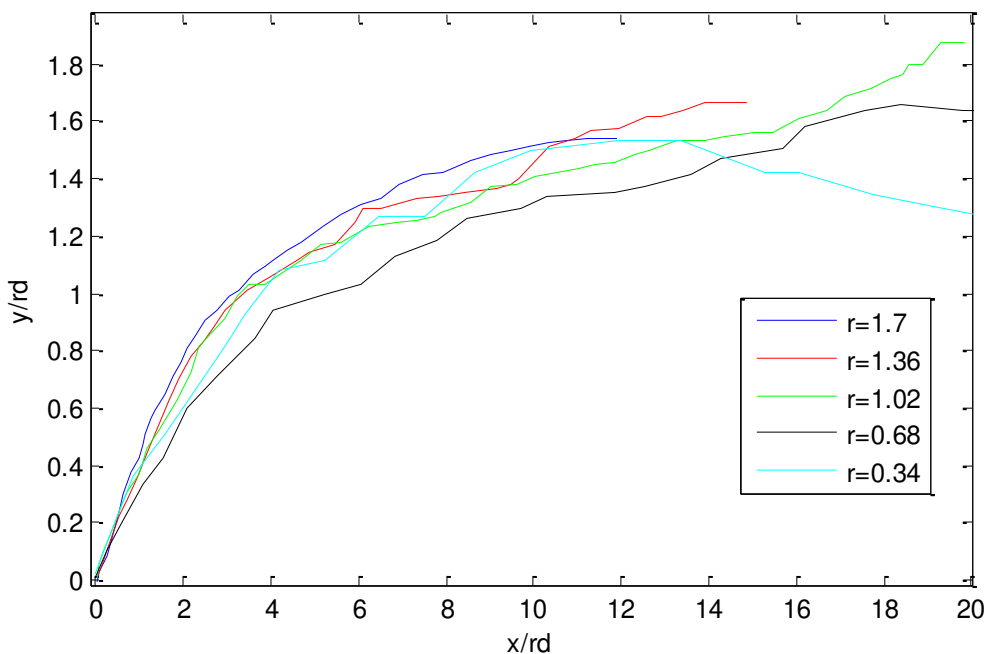


Figure 45. OpenFOAM trajectories for different velocity ratio conditions of a  $30^\circ$  jet scaled by  $rd$

While CFD ideally provides a better understanding of a configuration, identically matching real world cases with CFD proves to be a challenge requiring additional computational cost and analysis. As mentioned the crossflow boundary layer thickness is under-represented in the CFD simulation, potentially contributing to discrepancies between the experiment and

simulation. Additionally, effects such as heat transfer, turbulence, and jet velocity profiles are very difficult to identically match to experiments, potentially leading to differing comparisons.

If identical conditions between experiments and modeled cases are sought, a more restricted configuration involving the addition of a plenum could be included to the mesh, which would potentially account for entrance effects into the jet pipe. Additionally, hotwire data of the test facility could be collected and incorporated via turbulence scale definitions and boundary layer profile tailoring of the CFD model. While a more complete refinement of the CFD scheme could be tailored to identically match the experimental results, these results from CFD highlight some basic advantages of simulating the problem, even at the expense of minor discrepancies between experiments and modeling.

Currently, there is no single measurement technique which has the ability to deduce all the characteristics of the flow simultaneously. Aside from the lack of physical experimental complications, the largest benefit of using CFD in this study is the ability to concurrently obtain pressure, temperature, velocity magnitude and direction, and phase concentration in a full field manner, while current LIF experimentation is limited to single phase concentration mapping in this study. Additionally, CFD has the ability to impose relatively clean boundary conditions, which allow for better parametric isolation of effects.

## **CHAPTER 6: CONCLUSIONS**

In this study a new measurement technique was brought to the university, and validated according to previous literature reports on LIF. A correction process to accurately convert from recorded fluorescence to quantitative concentration profiles allows for the characterization of an acetone seeded jet both in terms of mole fraction distributions, as well as trajectory scaling characteristics. Validation with a freejet elucidates the individual correction components and yields results consistent with knowledge of turbulent freejets. By imaging centerline profiles in the wall normal plane of jets in crossflow, a better understanding of the jet's behavior allows for interpretation in schemes of film cooling.

Additionally, a small scale wind tunnel was designed which allows for future testing of a much more complete nature. Modifications specifically tailored the system to allow for PLIF testing using a 266nm excitation wavelength in conjunction with acetone vapor. Removable coupon inserts allow for rapid prototyping and testing of various configurations of single rows of film cooling holes, with the ability to alter inclination and compound angles, as well as hole geometry.

Scaling investigations provided convincing results in predicting the jet trajectory of near wall non-orthogonal jets in crossflow. With parametric variation of the velocity ratio, the trajectory of an orthogonal jet appears as a nonlinear function of the velocity ratio, specifically as a combination of mass and momentum flux ratios. Literature results offer slightly conflicting reports but have repeatedly predicted a strong dependence on the velocity ratio. Contrary to the orthogonal case, non-orthogonal jets consistently demonstrate a linear dependence of the trajectory on the velocity ratio. Similarly, with parametric variation of the inclination angle, the

jet trajectory appears as a linear function of the wall-normal component of the initial jet velocity. This was shown as a repeatable trend across a range of velocity ratios.

Finally CFD modeling allowed for cross comparisons with the experimental results. While initial attempts in modeling matched the trajectory well, incorrect turbulence conditions demonstrated an over dominance of the CVP. Turbulence modifications improved experimental and modeling agreement, and allowed for confidence in comparing measured trajectories. In parallel with experimental results, jet trajectories for a low angle of inclination jet demonstrate strong scaling dependencies with the parameter  $rd$ . Cross comparisons indicate a coupling between the CVP in the jet and large scale turbulence of the jet. Increased turbulence appears to foster a more diffuse jet structure, and a reduction in the CVP's ability to self affect the jet structure.

The possibilities for future work are immense as a main focus of this study was implementing a PLIF based system for studying jets in crossflow. Since literature and this study focus primarily on the effect of velocity ratio and to a lesser extent inclination angle, a need exists for a parametric variation of the density ratio as well to further understand trajectory predictions. While this is reported in surface tests via the blowing ratio, trajectory studies have tended to neglect this factor.

A primary extension of this work should involve a slight configuration shift in which fluid adjacent to the wall surface should be characterized in a 2d manner. By mapping the jet concentration near the 2d wall surface, comparisons can be drawn about the dispersion and cooling effectiveness along the surface. There is an abundance of PSP and TSP data regarding film cooling configurations of jets in crossflow, and PLIF of the surface coolant distribution can be directly used to cross validate both techniques. Specifically, the optimal cooling efficiency

can be determined by varying velocity ratios, mass flux ratios, and hole geometries. As mentioned, hole geometries provide the opportunity to greatly influence the dispersion and consequently cooling characteristics. Due to their importance in the jet structure, vorticity effects including the CVP can be modulated through altering hole geometries and configurations. Ultimately, the results from this study and future related studies can lead to a more comprehensive understanding of jets in crossflow, and cooling efficiencies in film cooling configurations.

## **APPENDIX A: LIF PROCESSING CODE**

```

%% LIF processing code
% Date: Jan 28, 2014
% Ver: Crossflow (full correction, adapted from v6 code)

tic
clc, clear all, close all;

%% %% %% %% %% %% %% %% %% %% %% %% %% %% %% %% %% %% %% %% %% %% %% %% %% %% %% %% %%

NUMBER = 2; % image set to process

% testing data
filename = './20141017 - lif.xlsx';
data_range = 'c6:e14';

% switches
crop = 1; % 1 if you want to crop the picture if
not 0
save = 0; % 1 if you want to save the pictures
after the correction if not 0
absorption_correction_adapted = 0; % 1 if you want to adapt the correction
for the absorption (take more time) if not 0

%%% Coordinate system inputs
x_i_pixel_origin = 142;
y_j_pixel_origin = 0;

% pixels per meter
ppm = 40/.003;

% crop region
if crop == 1
    y_i_crop = 200:1100; %vertical direction
    x_j_crop = 760:950; %horizontal direction
elseif crop == 0
    y_i_crop = 1:1200; %vertical direction
    x_j_crop = 1:1600; %horizontal direction
end
angle=-.5;

%%% End of inputs

% load data
[numeric , image_names , raw] = xlsread(filename , 'Data' , data_range);
image_count = numeric(:,1); % number of images associated with each set
v_dot_l_min = numeric(:,2); % air volumetric flow rate in liters/minute

% Jet Re # calculation
rho = 1.225; % density of fluid (air acetone
mixture) - kg/m^3
mu = 1.73*10^-5; % dynamic viscosity, SI units

```

```

V_dot    = v_dot_l_min*1.66666667*10^-5; % m^3/s
D        = 0.003;                       % jet exit diameter, meters
U        = V_dot/(pi/4*D^2);            % average jet velocity
Re_jet   = rho*D*U/mu;                  % Jet Re

% load background image
load bg1_avg.mat
bg = imrotate(average,angle);
clear average sdev
figure
imagesc(bg(y_i_crop,x_j_crop))

% filter
filter = bg < 1825;

% % correction
load call_avg.mat %get calibration sheet
average=imrotate(average,angle);
average=average(y_i_crop,x_j_crop);
average=average / max(max(average));%normalize entire sheet by max value
indices=zeros(size(average));
for j=2:length(average(1,:))
    indices(:,j)=indices(:,j-1)+average(:,j);
end
indices=indices/max(max(indices));
for i = 1:size(average,2)
    corrx(:,i)=average(:,i);
    corry(i)=mean(average(20:size(average,1)-20,i))/max(max(average));
end

figure; imagesc(corrx); title('corrx before absorbtion');

%remove absorbtion by dividing by y-average of sheet as a funct of x
for ii = 1:length(y_i_crop);
    corrx1(ii,:) = corrx(ii,:) ./ corry;
end
corrx1=corrx1/max(max(corrx1));
%remove absorbtion by normalizing each column of the sheet
for ii = 1:length(x_j_crop);
    corrx2(:,ii)= corrx(:,ii) ./max(smooth(double(corrx(:,ii))));
end
corrx=(corrx1+corrx2)/2;

for i=1:length(x_j_crop);
    corrx(:,i)=smooth(corrx(:,i));
end
corrx=corrx-min(min(corrx));
corrx=corrx ./ max(max(corrx));
figure; imagesc(corrx); title('corrx after absorption');

counter = 0;
for j = 1:image_count(NUMBER)

```



```

% load test images
load_command = sprintf('%s', char(image_names(NUMBER)), '_',
num2str(j,'%04d'), '.tif');
raw_image = imread(sprintf('%s',load_command));
raw_image=imrotate(raw_image,angle);
raw_image = double(raw_image);

% subtract background from test image
bg_subtract = raw_image(y_i_crop,x_j_crop) - bg(y_i_crop,x_j_crop);
bg_subtract(bg_subtract < 0.05) = 0;

% x/d and y/d
x_pix = 1:size(bg_subtract,1);
y_pix = 1:size(bg_subtract,2);
x_m = (x_pix - x_i_pixel_origin) / ppm;
y_m = (y_pix - y_j_pixel_origin) / ppm;
x_d = x_m / D;
y_d = y_m / D;

% check for low laser power
checker = mean(mean(bg_subtract));
corrected_image = ones(size(bg_subtract));

% ----- apply correction -----
bg_sum=zeros(size(bg_subtract));
bg_sum(1,1)=bg_subtract(1,1);
corrected_image = bg_subtract;

% % correction adapted for absorption
if absorption_correction_adapted == 1
    for ii = 1:length(y_i_crop);
        for jj = 2:length(x_j_crop)
            bg_sum(ii,jj)=bg_sum(ii,jj-1)+bg_subtract(ii,jj);
        end
    end
    bg_sum=bg_sum/max(max(bg_sum));
    bg_sum=bg_sum/2;
    corry_effective=zeros(size(bg_sum));
    for ii = 1:length(y_i_crop);
        for jj = 2:length(x_j_crop)
            [~,jjj] = min(abs(indices(ii,:) - bg_sum(ii,jj)));
            corrected_image(ii,jj)=corrected_image(ii,jj)/corry(jjj);
            corry_effective(ii,jj)=corry(jjj);
        end
    end
end

% correction unadapted for absorption
else
    for ii = 1:length(y_i_crop);
        corrected_image(ii,:) = corrected_image(ii,:) ./ corry;
    end
end
end

```

```

corrected_image = corrected_image ./ corrx; %correct for the laser sheet
profile

if checker > 0 % if laser is on
    counter = counter + 1;

    % build a tensor with each background subtracted test image
    d(:,:,counter) = corrected_image .* filter(y_i_crop,x_j_crop);

    % save each instantaneous image
    if save == 1
        g = sprintf('%s', 'print -dtiff results_',
char(image_names(NUMBER)), '_', num2str(counter), '.tif;');
        eval(g)
    end

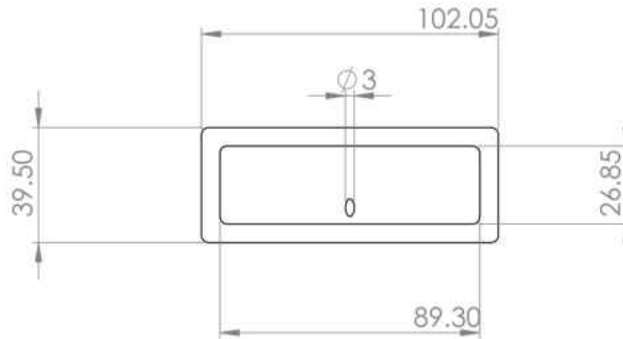
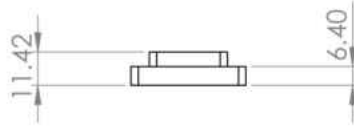
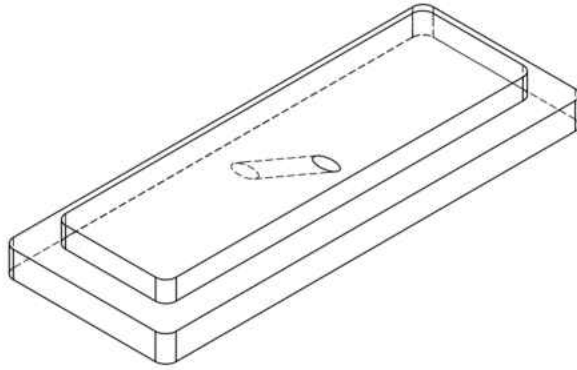
    else % if laser is off
        j
    end
end

% calculate average
davg = mean(d,3);
%davg=davg/max(max(davg));

% plot average
figure, imagesc(x_d,y_d, rot90(davg)/max(davg))
xlabel('x/d')
ylabel('y/d')
colorbar
%axis image
caxis([0 1])
title('Mean profile')

```

## **APPENDIX B: SAMPLE COUPON DRAWING**



UNLESS OTHERWISE SPECIFIED: DIMENSIONS ARE IN MILLIMETERS SURFACE FINISH: TOLERANCES: LINEAR: ANGULAR:				FINISH:		DEBUR AND BREAK SHARP EDGES		DO NOT SCALE DRAWING		REVISION	
DRAWN				SIGNATURE		DATE		TITLE:			
CHKD											
APPVD											
MFG											
Q.A						MATERIAL:		DWG NO: <b>30deg3mmOneHole</b> A4			
						WEIGHT:		SCALE:1:2		SHEET 1 OF 1	

## REFERENCES

- [1] <http://sl.ibtimes.com>
- [2] Ben-Yakar, A. and R. Hanson, "Ultra-fast-framing schlieren system for studies of the time evolution of jets in supersonic crossflows", *Experiments in fluids*, Vol.32, No.6, 2002, pp.652-666
- [3] Turns, S. R., *An introduction to combustion*, McGraw-hill New York, 1996
- [4] Bogard, D. G., "Airfoil film cooling", *The Gas Turbine Handbook*, 2006
- [5] Yuen, C. and R. Martinez-Botas, "Film cooling characteristics of rows of round holes at various streamwise angles in a crossflow: Part I. Effectiveness", *International Journal of Heat and Mass Transfer*, Vol.48, No.23, 2005, pp.4995-5016
- [6] Yuen, C. and R. Martinez-Botas, "Film cooling characteristics of rows of round holes at various streamwise angles in a crossflow: Part II. Heat transfer coefficients", *International Journal of Heat and Mass Transfer*, Vol.48, No.23, 2005, pp.5017-5035
- [7] Han, J. C., S. Dutta and S. Ekkad, *Gas Turbine Heat Transfer and Cooling Technology, Second Edition*, Taylor & Francis, 2012
- [8] <http://www.yxlon.com/Resources/Applications-en/Castings/TurbineBlades>
- [9] [http://avherald.com/img/qantas\\_b734\\_vh-tjy\\_brisbane\\_091110\\_1.jpg](http://avherald.com/img/qantas_b734_vh-tjy_brisbane_091110_1.jpg)
- [10] Brock, B., R. H. Haynes, B. S. Thurow, G. Lyons and N. E. Murray, "An examination of MHz rate PIV in a heated supersonic jet", *AIAA Paper*, Vol.1102, 2014,
- [11] Westerweel, J., T. Hofmann, C. Fukushima and J. Hunt, "The turbulent/non-turbulent interface at the outer boundary of a self-similar turbulent jet", *Experiments in Fluids*, Vol.33, No.6, 2002, pp.873-878
- [12] Natsui, G., Z. Little and J. Kapat, "A detailed uncertainty analysis of adiabatic film cooling effectiveness measurements using pressure sensitive paint," *ASME Turbo Expo Montreal*, Canada, GT2015-42707, 2015
- [13] Gregory, J., K. Asai, M. Kameda, T. Liu and J. Sullivan, "A review of pressure-sensitive paint for high-speed and unsteady aerodynamics", *Proceedings of the Institution of Mechanical Engineers, Part G: Journal of Aerospace Engineering*, Vol.222, No.2, 2008, pp.249-290
- [14] Sakamura, Y., T. Suzuki, M. Matsumoto, G. Masuya and Y. Ikeda, "Optical measurements of high-frequency pressure fluctuations using a pressure-sensitive paint and Cassegrain optics", *Measurement Science and Technology*, Vol.13, No.10, 2002, pp.1591
- [15] Kameda, M., T. Tabei, K. Nakakita, H. Sakaue and K. Asai, "Image measurements of unsteady pressure fluctuation by a pressure-sensitive coating on porous anodized aluminium", *Measurement Science and Technology*, Vol.16, No.12, 2005, pp.2517
- [16] Epstein, A. H., "Fluorescent gaseous tracers for three dimensional flow visualization," Massachusetts Institute of Technology, Department of Aeronautics and Astronautics, 1972
- [17] Dimotakis, P. E., R. C. Miake-Lye and D. A. Papantoniou, "Structure and dynamics of round turbulent jets", *Physics of Fluids*, Vol.26, No.11, 1983, pp.3185-3192
- [18] Kychakoff, G., R. D. Howe, R. K. Hanson, M. C. Drake, R. W. Pitz, M. Lapp and C. M. Penney, "Visualization of turbulent flame fronts with planar laser-induced fluorescence", *Science*, Vol.224, No.4647, 1984, pp.382-384
- [19] Kychakoff, G., R. D. Howe, R. K. Hanson and J. C. McDaniel, "Quantitative visualization of combustion species in a plane", *Applied optics*, Vol.21, No.18, 1982, pp.3225-3227

- [20] Kychakoff, G., K. Knapp, R. Howe and R. Hanson, "Flow visualization in combustion gases using nitric oxide fluorescence", *AIAA journal*, Vol.22, No.1, 1984, pp.153-154
- [21] Thurber, M. C., B. J. Kirby and R. K. Hanson, "Instantaneous imaging of temperature and mixture fraction with dual-wavelength acetone PLIF," *36th AIAA Aerospace Sciences Meeting and Exhibit*, 1998
- [22] Measures, R. M., "Selective Excitation Spectroscopy and Some Possible Applications", *Journal of Applied Physics*, Vol.39, No.11, 1968, pp.5232-5245
- [23] Lozano, A., "Laser-Excited Luminescent Tracers for Planar Concentration Measurements in Gaseous Jets," Ph. D. dissertation, Department of Mechanical Engineering, Stanford University, 1992
- [24] Baba, M. and I. Hanazaki, "The S 1, 1 A 2 (n,  $\pi^*$ ) state of acetone in a supersonic nozzle beam. Methyl internal rotation", *Chemical physics letters*, Vol.103, No.2, 1983, pp.93-97
- [25] <http://web.uvic.ca/ail/techniques/Jablonski.jpg>
- [26] Lochman, B., Z. Murphree, V. Narayanaswamy and N. Clemens, "PLIF imaging of naphthalene-ablation products in a Mach 5 turbulent boundary layer," *27th AIAA Aerodynamic Measurement Technology and Ground Testing Conference*, AIAA,
- [27] Koban, W., J. D. Koch, R. K. Hanson and C. Schulz, "Absorption and fluorescence of toluene vapor at elevated temperatures", *Physical chemistry chemical physics*, Vol.6, No.11, 2004, pp.2940-2945
- [28] Hiller, B. and R. Hanson, "Properties of the iodine molecule relevant to laser-induced fluorescence experiments in gas flows", *Experiments in fluids*, Vol.10, No.1, 1990, pp.1-11
- [29] Yoo, J. H., *Strategies for planar laser-induced fluorescence thermometry in shock tube flows*, Ph.D Dissertation, Stanford University, 2011
- [30] Fric, T. F., "Structure in the near field of the transverse jet," DTIC Document, 1990
- [31] Fric, T. and A. Roshko, "Vortical structure in the wake of a transverse jet", *Journal of Fluid Mechanics*, Vol.279, 1994, pp.1-47
- [32] Mahesh, K., "The interaction of jets with crossflow", *Annual Review of Fluid Mechanics*, Vol.45, 2013, pp.379-407
- [33] Krothapalli, A., L. Lourenco and J. Buchlin, "Separated flow upstream of a jet in a crossflow", *AIAA journal*, Vol.28, No.3, 1990, pp.414-420
- [34] Kelso, R. and A. Smits, "Horseshoe vortex systems resulting from the interaction between a laminar boundary layer and a transverse jet", *Physics of Fluids (1994-present)*, Vol.7, No.1, 1995, pp.153-158
- [35] Kelso, R. M., T. Lim and A. E. Perry, "An experimental study of round jets in cross-flow", *Journal of Fluid Mechanics*, Vol.306, 1996, pp.111-144
- [36] Fearn, R. and R. P. Weston, "Vorticity associated with a jet in a cross flow", *AIAA Journal*, Vol.12, No.12, 1974, pp.1666-1671
- [37] McMahan, H., D. Hester and J. Palfery, "Vortex shedding from a turbulent jet in a cross-wind", *Journal of Fluid Mechanics*, Vol.48, No.01, 1971, pp.73-80
- [38] Coelho, S. L. and J. Hunt, "The dynamics of the near field of strong jets in crossflows", *Journal of Fluid Mechanics*, Vol.200, 1989, pp.95-120
- [39] Needham, D., N. Riley and J. Smith, "A jet in crossflow", *Journal of Fluid Mechanics*, Vol.188, 1988, pp.159-184
- [40] Morton, B. R. and A. Ibbetson, "Jets deflected in a crossflow", *Experimental Thermal and Fluid Science*, Vol.12, No.2, 1996, pp.112-133

- [41] Muppidi, S. and K. Mahesh, "Direct numerical simulation of round turbulent jets in crossflow", *Journal of Fluid Mechanics*, Vol.574, 2007, pp.59-84
- [42] Su, L. and M. Mungal, "Simultaneous measurements of scalar and velocity field evolution in turbulent crossflowing jets", *Journal of fluid mechanics*, Vol.513, 2004, pp.1-45
- [43] Sau, R. and K. Mahesh, "Dynamics and mixing of vortex rings in crossflow", *Journal of fluid Mechanics*, Vol.604, 2008, pp.389-409
- [44] Labus, T. L. and E. P. Symons, "Experimental investigation of an axisymmetric free jet with an initially uniform velocity profile", 1972
- [45] Su, L., D. Han, R. Mirafior and M. Mungal, "Measurements of scalar and velocity fields in turbulent crossflowing jets with low velocity ratio", *AIAA paper*, Vol.815, No.1, 2000, pp.1-11
- [46] Lanitis, N. and J. R. Dawson, "Multi-Scale Stereoscopic PIV measurements of a Jet in a Cross-Flow", *J Fluid Mech*, Vol.566, 2012, pp.47-96
- [47] Kawai, S. and S. K. Lele, "Large-eddy simulation of jet mixing in supersonic crossflows", *AIAA journal*, Vol.48, No.9, 2010, pp.2063-2083
- [48] Kawai, S. and S. K. Lele, "Mechanisms of jet mixing in a supersonic crossflow: a study using large-eddy simulation", *AIAA paper*, Vol.4575, 2008, pp.2008
- [49] Beresh, S. J., J. F. Henfling, R. J. Erven and R. W. Spillers, "Penetration of a transverse supersonic jet into a subsonic compressible crossflow", *AIAA journal*, Vol.43, No.2, 2005, pp.379-389
- [50] Santiago, J. G. and J. C. Dutton, "Velocity measurements of a jet injected into a supersonic crossflow", *Journal of Propulsion and Power*, Vol.13, No.2, 1997, pp.264-273
- [51] Chai, X. and K. Mahesh, "Simulations of high speed turbulent jets in crossflow," *40th Fluid Dynamics Conference and Exhibition, Paper AIAA, 2010*
- [52] Yuan, L. L. and R. L. Street, "Trajectory and entrainment of a round jet in crossflow", *Physics of Fluids (1994-present)*, Vol.10, No.9, 1998, pp.2323-2335
- [53] Hasselbrink, E. F. and M. Mungal, "Transverse jets and jet flames. Part 1. Scaling laws for strong transverse jets", *Journal of Fluid Mechanics*, Vol.443, 2001, pp.1-25
- [54] Margason, R. J., "Fifty years of jet in cross flow research," *In AGARD, Computational and Experimental Assessment of Jets in Cross Flow 41 p (SEE N94-28003 07-34)*,
- [55] Smith, S. and M. Mungal, "Mixing, structure and scaling of the jet in crossflow", *Journal of Fluid Mechanics*, Vol.357, 1998, pp.83-122
- [56] Pratte, B. D. and W. D. Baines, "Profiles of the round turbulent jet in a cross flow", *Journal of the Hydraulics Division*, Vol.93, No.6, 1967, pp.53-64
- [57] Keffer, J. and W. Baines, "The round turbulent jet in a cross-wind", *Journal of Fluid Mechanics*, Vol.15, No.04, 1963, pp.481-496
- [58] Muppidi, S. and K. Mahesh, "Study of trajectories of jets in crossflow using direct numerical simulations", *Journal of Fluid Mechanics*, Vol.530, 2005, pp.81-100
- [59] Han, J.-C. and A. Rallabandi, "Turbine blade film cooling using PSP technique", *Frontiers in Heat and Mass Transfer (FHMT)*, Vol.1, No.1, 2010
- [60] New, T., T. Lim and S. Luo, "Elliptic jets in cross-flow", *Journal of fluid mechanics*, Vol.494, 2003, pp.119-140
- [61] Liscinsky, D. S., B. True and J. Holdeman, "Crossflow mixing of noncircular jets", *Journal of propulsion and power*, Vol.12, No.2, 1996, pp.225-230
- [62] Schmidt, D. L., B. Sen and D. G. Bogard, "Film cooling with compound angle holes: adiabatic effectiveness", *Journal of Turbomachinery*, Vol.118, No.4, 1996, pp.807-813

- [63] Thole, K., M. Gritsch, A. Schulz and S. Wittig, "Effect of a Crossflow at the Entrance to a Film-Cooling Hole", *Journal of fluids engineering*, Vol.119, No.3, 1997, pp.533-540
- [64] Andreopoulos, J. and W. Rodi, "Experimental investigation of jets in a crossflow", *Journal of Fluid Mechanics*, Vol.138, 1984, pp.93-127
- [65] Takeishi, K., M. Komiyama, Y. Oda and Y. Egawa, "Aerothermal Investigations on Mixing Flow Field of Film Cooling With Swirling Coolant Flow", *Journal of Turbomachinery*, Vol.136, No.5, 2014, pp.051001
- [66] Kusterer, K., D. Bohn, T. Sugimoto and R. Tanaka, "Double-jet ejection of cooling air for improved film cooling", *Journal of Turbomachinery*, Vol.129, No.4, 2007, pp.809-815
- [67] Heidmann, J. D. and S. Ekkad, "A novel antivortex turbine film-cooling hole concept", *Journal of turbomachinery*, Vol.130, No.3, 2008, pp.031020
- [68] Rigby, D. L. and J. D. Heidmann, "Improved film cooling effectiveness by placing a vortex generator downstream of each hole," *ASME Turbo Expo 2008: Power for Land, Sea, and Air, 2008*
- [69] Bejan, A., *Heat transfer*, John Wiley & Sons, Inc., 1993
- [70] Eckert, E., H. Sakamoto and T. Simon, "The heat/mass transfer analogy factor,  $Nu/Sh$ , for boundary layers on turbine blade profiles", *International Journal of Heat and Mass Transfer*, Vol.44, No.6, 2001, pp.1223-1233
- [71] Ritchie, "Quantitative Acetone PLIF Measurements of Jet Mixing With Synthetic Jet Actuators," Ph. D. Thesis, Georgia Institute of Technology, 2006
- [72] <http://www.pco.de>
- [73] MATLAB, Release R2014b, Natick, Mass., 2014
- [74] Becker, H., H. Hottel and G. Williams, "The nozzle-fluid concentration field of the round, turbulent, free jet", *Journal of Fluid Mechanics*, Vol.30, No.02, 1967, pp.285-303
- [75] Jasak, H., A. Jemcov and Z. Tukovic, "OpenFOAM: A C++ library for complex physics simulations," *International workshop on coupled methods in numerical dynamics*,
- [76] Kissling, K., J. Springer, H. Jasak, S. Schütz, K. Urban and M. Piesche, "A coupled pressure based solution algorithm based on the volume-of-fluid approach for two or more immiscible fluids," *V European Conference on Computational Fluid Dynamics, Lisbon, Portugal*,
- [77] Haven, B., D. Yamagata, M. Kurosaka, S. Yamawaki and T. Maya, "Anti-kidney pair of vortices in shaped holes and their influence on film cooling effectiveness," *ASME 1997 International Gas Turbine and Aeroengine Congress and Exhibition, 1997*